

Copyright
by
Gergana Ilieva Drandova
2001

The Dissertation Committee for Gergana Ilieva Drandova
Certifies that this is the approved version of the following dissertation:

**NMR INVESTIGATIONS IN COPPER-OXIDE
CHAIN COMPOUNDS AND HIGH-T_C
SUPERCONDUCTORS**

Committee:

John T. Markert, Supervisor

Qian Niu

Alejandro De Lozanne

Peter R. Antoniewicz

John T. McDevitt

**NMR INVESTIGATIONS IN COPPER-OXIDE
CHAIN COMPOUNDS AND HIGH-T_C
SUPERCONDUCTORS**

by

GERGANA ILIEVA DRANDOVA, B.S.

DISSERTATION

Presented to the Faculty of the Graduate School of
The University of Texas at Austin
in Partial Fulfillment
of the Requirements
for the Degree of

DOCTOR OF PHILOSOPHY

The University of Texas at Austin

August 2001

UMI Number: 3031043

UMI[®]

UMI Microform 3031043

Copyright 2001 by Bell & Howell Information and Learning Company.

All rights reserved. This microform edition is protected against
unauthorized copying under Title 17, United States Code.

Bell & Howell Information and Learning Company
300 North Zeeb Road
P.O. Box 1346
Ann Arbor, MI 48106-1346

Acknowledgements

First, I would like to thank Dr. Markert for being the nicest, most knowledgeable advisor one could hope to have, and for introducing me to the wonderful world of experimental physics. I would like to thank him for patiently teaching me how to be time efficient and in the same moment precise to the smallest detail, and how to not get disappointed from the “temporary” equipment misfortunes but to keep fixing things until they stop breaking.

I also thank Tina Barrett, Koki Mochizuki, and Tobias Graf for helping me during my starting period in the lab. Thanks to Peter Russo for showing me how to do different things and for constantly making everyone laugh. Special thanks to Troy Messina for always being willing to take the time to educate me in various subjects—either lab or American culture and crossword-puzzle-solving related. I thank Elin Winkler for the helpful discussions and for sharing with me the happy and the disappointing moments we had, while briefly working on the same project and I thank Casey Miller for saving my thumb. I also wish to thank all the other members of the Markert group for making my time in the lab enjoyable.

I would like to thank Jack Clifford for ensuring that I always came back from the student shop happy with my part and with all five fingers on each hand. I thank everyone in the machine shop who ever had to build a part for

me. I wish to thank Jesse Martinez and Harold Williamson for supplying the uncountable liters of liquid nitrogen and helium I used in my experiment. I also thank John England for answering my electronics questions and for his always helpful suggestions.

Next, I would like to thank my parents Ivanka and Ilia Drandovi for their support and for always letting me make my own choices. I thank my friends Tania, Albena, and Iaki for sharing with me some of the best and the most fun moments of my life. Thanks guys for all the laughs and card games we had and played together. I thank Zechka for being my friend in all these years and I also thank Boro for his humor and for knowing the answer to any question.

I thank my Russian literature teacher Elena Chakarova for the inspiration and for believing in me. I thank my classical guitar teacher Maria Cortes for sharing with me the secrets and all the little details that make the difference, and for encouraging me to simply practice more every time I thought I've reached my limit.

Finally, I wish to thank my husband Sergey Cheshkov for all his love and for being my accessible at any time “all-of-physics textbook”.

NMR INVESTIGATIONS IN COPPER-OXIDE CHAIN COMPOUNDS AND HIGH- T_C SUPERCONDUCTORS

Publication No. _____

Gergana Ilieva Drandova, Ph.D.
The University of Texas at Austin, 2001

Supervisor: John T. Markert

We report ^{89}Y nuclear magnetic resonance measurements of the chain compound $\text{Ca}_{2+x}\text{Y}_{2-x}\text{Cu}_5\text{O}_{10}$. It is believed that this compound undergoes an antiferromagnetic 3D ordering transition at low temperatures for small doping concentrations of $x \approx 0$, while for higher dopings it exhibits a quasi-1D chain behavior, and finally transitions to cluster behavior for doping levels close to $x = 2$. We present measurements of the spin-lattice and the spin-spin relaxation times T_1 and T_2 , respectively, at several different temperatures for $x = 0$ and $x = 0.5$. Information for the spin correlation times in the studied system was extracted from the relaxation rates. In addition, a measurement of the lineshape was made for the $x = 0.5$ sample.

As a preparation for the experiment, modifications in the original design of the NMR probe were made which significantly improved its functionality and eased the data acquisition process. The 160 MHz intermediate frequency

NMR spectrometer was rebuilt and its operation was tested by performing NMR on several reference samples.

Table of Contents

Acknowledgements	iv
Abstract	vi
List of Tables	x
List of Figures	xi
Chapter 1. Introduction	1
Chapter 2. NMR Fundamentals and Measurement Techniques	5
2.1 Basic Theory of NMR	5
2.1.1 The Nuclear Magnetic Resonance Phenomenon	5
2.1.2 Classical Treatment of Noninteracting Nuclear Moments in an Alternating Magnetic Field	9
2.1.3 Bloch Equations	15
2.2 Measurement Techniques	17
2.2.1 Free Induction Decay, Spin-Echoes, and Spin-Spin Relaxation	18
2.2.2 Spin-Lattice Relaxation	22
2.2.3 Spin-Lattice Relaxation in the Rotating Frame	27
Chapter 3. Experimental Set-Up and Considerations	31
3.1 Overview	31
3.2 The Tank Circuit	33
3.2.1 Tank Circuit Requirements	33
3.2.2 Operation of the Tank Circuit and Tuning Considerations .	37
3.3 The Probe	40
3.4 The NMR Spectrometer	47
3.4.1 Spectrometer Operation	47

3.4.2	Signal Level Considerations and Modifications Made to the Original Spectrometer Configuration	50
3.4.3	Deuterium and ^{23}Na NMR as a Test of the Proper Functioning of the Spectrometer	62
3.4.4	Reducing the Spectrometer Ringing	65
Chapter 4.	Prelude to ^{63}Cu NMR in $\text{YBa}_2\text{Cu}_3\text{O}_7$	71
4.1	Overview and Motivation for Conducting the Experiment	71
4.2	Sample Preparation and Attempted NMR Measurements	76
Chapter 5.	^{89}Y NMR in the $\text{Ca}_{2+x}\text{Y}_{2-x}\text{Cu}_5\text{O}_{10}$ Spin-Chain Compound	84
5.1	The $\text{Ca}_{2+x}\text{Y}_{2-x}\text{Cu}_5\text{O}_{10}$ System—Structure and Sample Preparation	84
5.2	Results and Suggestions for Future Work	86
Appendix A.		99
Bibliography		101
Vita		107

List of Tables

- 5.1 ^{89}Y NMR T_1 and T_2 values for the $\text{Ca}_{2+x}\text{Y}_{2-x}\text{Cu}_5\text{O}_{10}$ compound. 93

List of Figures

2.1	Energy levels for a spin 5/2 nucleus. The lowest energy orientation of the magnetic moment is along the field.	7
2.2	The linearly polarized magnetic field $\mathbf{H}_x(t)$ is decomposed to two rotating components \mathbf{H}_R and \mathbf{H}_L	10
2.3	The magnetic field \mathbf{H}_1 is static in the new reference frame rotating about the z axis of the laboratory frame with an angular frequency ω	12
2.4	Precession of $\boldsymbol{\mu}$ about the effective magnetic field \mathbf{H}_{eff} in the rotating frame.	13
2.5	The magnetization is tipped by \mathbf{H}_1 —the only remaining component of the effective field.	14
2.6	After a $\pi/2$ pulse the magnetization dephases in the x' - y' plane with a characteristic time constant T_2^* . After waiting longer times, M_0 relaxes to its thermal equilibrium value along z' but this does not induce a signal in the pickup coil.	20
2.7	$\pi/2 - \tau - \pi$ pulse sequence for inducing an echo.	21
2.8	(a)Inducing a negative echo by applying a π pulse along the x' direction at time τ after the $\pi/2$ pulse. (b)Inducing a positive echo by applying the π pulse along the y' direction.	23
2.9	Saturating comb of 5 $\pi/2$ pulses separated by time t_1 is used for destroying the initial magnetization. T_1 is detected by monitoring the echo strength growth as a function of t	26
2.10	$T_{1\rho}$ measurement sequence.	28
3.1	Experimental set-up.	32
3.2	Tank circuit.	38
3.3	Diagram of the low temperature NMR probe.	41
3.4	Details of the bottom of the probe.	44
3.5	The 160 MHz intermediate frequency NMR spectrometer.	49
3.6	Schematic diagram of the frequency doubler.	52
3.7	Schematic diagram of the single-side-band mixer.	54

3.8	Schematic diagram of the transmitter.	55
3.9	Schematic diagram of the receiver and the demodulator. . . .	58
3.10	Modifications to the switch driver card made to obtain a selectable delay of the receiver turn-on time.	61
3.11	Room temperature T_1 measurement of deuterium as a test of the proper functioning of the spectrometer. Solid line is an exponential fit to the data.	63
3.12	Room temperature T_2 measurement of deuterium as a test of the proper functioning of the spectrometer. Solid line is a gaussian fit to the data.	64
3.13	Signal-averaged quadrature outputs showing an NMR echo (deuterium) with the spectrometer ringing present in the beginning of both channels.	66
3.14	Ringing at the output of the power amplifier (a), and at the preamplifier input (b) observed directly and when attenuated with a crossed-diode box.	67
3.15	(a)Reduction of the ringing at the power amplifier output when using a high-pass RC filter or a $\lambda/4$ cable; (b)Output of the preamplifier when using a $\lambda/4$ cable as a method of ringing attenuation and triggering the Nicolet at the rising edge of a $70 \mu s$ pulse.	69
4.1	Magnetic moment measurement of the $YBa_2Cu_3O_7$ powder cured in epoxy with the field respectively parallel and perpendicular to the crystallites' c axis.	80
4.2	X-ray diffraction pattern of the YBCO sample embedded in epoxy (a) has the same peaks as a powder sample pattern (b). This points to the fact that orientation of the c axis of the crystallites was not achieved.	81
5.1	Shape of the ^{89}Y NMR line of the $Ca_{2.5}Y_{1.5}Cu_5O_{10}$ compound at 289 K.	87
5.2	^{89}Y T_2 measurements at 275 K (a) and room temperature (b) of the $Ca_2Y_2Cu_5O_{10}$ compound.	89
5.3	(a) ^{89}Y T_2 measurement of the $Ca_{2.5}Y_{1.5}Cu_5O_{10}$ compound at 289 K. (b) Straight-line fit of the logarithm of the signal as a function of 2τ	90
5.4	^{89}Y T_1 measurements at 250 K (a), 275 K (b), and room temperature (c) of the $Ca_2Y_2Cu_5O_{10}$ compound.	91

5.5	(a) ^{89}Y T_1 measurement of the $\text{Ca}_{2.5}\text{Y}_{1.5}\text{Cu}_5\text{O}_{10}$ compound at 289 K. (b) Straight-line fit of the logarithm of the difference between the equilibrium value and the current value of the signal as a function of recovery time.	92
5.6	Summarized results of the ^{89}Y T_1 and T_2 measurements of the $\text{Ca}_{2+x}\text{Y}_{2-x}\text{Cu}_5\text{O}_{10}$ system at different temperatures for doping concentrations of $x = 0$ and $x = 0.5$	94
A.1	The author, the NMR probe, and the superconducting magnet.	99
A.2	Collecting data from the $\text{Ca}_{2+x}\text{Y}_{2-x}\text{Cu}_5\text{O}_{10}$ material.	100

Chapter 1

Introduction

Nuclear magnetic resonance (NMR) was discovered in 1945. The original experiment did not seem to have many potential applications and was conducted purely for answering the question: is it possible to observe transitions between the quantum states of a nuclear system placed in magnetic field? Since then, however, NMR has rapidly developed and has become a science of its own finding a broad range of applications not only in physics, but also in chemistry, biology, and medicine. By detecting the resonance spectrum and measuring chemical shifts (observing the location of the resonance lines in a sample compared to their location in a reference sample) one can find the chemical composition of an unknown material and can determine the structure of complicated organic compounds. By measuring relaxation times of various types, it is possible to obtain information about the dynamics of a nonstationary system of molecules, say diffusion in a biological system. The use of field gradients has enabled scientists to obtain spatially resolved images of the studied systems. This has found application in medicine via magnetic resonance imaging (MRI), and in the recent topic of nuclear magnetic resonance force microscopy (NMRFM).

NMR has also become a widely used technique for studying solid state materials. Since the nuclei interact very weakly with their environment, NMR can be used for probing the structure and the interactions in a system without interfering with the studied processes.

Even though most of the interactions of the nuclei with their surroundings are of magnetic nature, NMR can be used to study both the magnetic and the electronic properties of a material. By determining the spin-relaxation times it is possible to extract information about atomic motions, the dynamics of spin systems, and fluctuations, for example, in the flux lines of a type II superconductor. Also it is possible to gather information about the electronic density of states at the Fermi energy, which can be used to study the gap opening in superconductors and the anisotropy of this gap.

In Chapter 2 of this study we present the basic theory of nuclear magnetic resonance, discussing from a classical point of view the interaction of nuclear spins with magnetic field. We introduce the rotating reference frame as a useful tool for simplifying the theoretical expressions and discuss the equations of motion of nuclear moments interacting not only with an external magnetic field but also with their environment. We introduce the spin-spin, spin-lattice, and spin-lattice in the rotating frame relaxation times and discuss the pulse measurement techniques used in the present study for extracting the afore-mentioned relaxation times.

Chapter 3 is dedicated to the experimental set-up. We analyze the requirements for building a successfully operating NMR tank circuit and provide a detailed description of the NMR probe and the improvements made to it

during the measurements. A thorough discussion of the operation of the NMR spectrometer and its components is provided. Signal level considerations are presented and all the changes made to the electronic circuitry are documented. Measurements of the spin-lattice and spin-spin relaxation times of a deuterium sample are reported as a test of the proper operation of the spectrometer after the repairs made to it. An additional test of the spectrometer functioning at frequencies close to the frequency expected for ^{63}Cu (being the planned to study nucleus) was done by performing NMR on sodium nuclei in a NaCl sample. Finally, we discuss the search for the origin of the existing spurious ringing in the electronics and present a solution of this problem allowing us to proceed with our NMR measurements.

The discovery (1986) of high temperature superconductivity [1] in a Ba-La-Cu-O system brought much of excitement to the scientific community. In a very short time many new high temperature superconducting compounds were produced. A lot of effort was made to characterize the new materials structurally, as well as to determine their electronic, magnetic, and superconducting properties at different doping concentrations. Many of these results pointed to the fact that high temperature superconductivity cannot be properly described by the simple Bardeen-Cooper-Schrieffer theory. Hence, the major question still to be answered is: what is the mechanism of the pairing in the new compounds and what kind of theory should be used to model the high temperature superconductivity.

One of the most studied high- T_c materials is the Y-Ba-Cu-O system. In Chapter 4 we propose measurement of the spin-lattice relaxation time in the

rotating frame of the ^{63}Cu nuclei in $\text{YBa}_2\text{Cu}_3\text{O}_7$ and $\text{YBa}_2\text{Cu}_4\text{O}_8$ as a probe of the low frequency vortex fluctuations in these compounds. We report the preparation and characterization of the $\text{YBa}_2\text{Cu}_3\text{O}_7$ sample and conclude that a lack of grain alignment of the powder is the most probable reason for the unsuccessful detection of the NMR resonance.

The copper-oxide spin-chain compounds have received a lot of attention because of their interesting magnetic properties and because of their relation to the cuprate high temperature superconductors. In Chapter 5 we present ^{89}Y NMR measurements in the $\text{Ca}_{2+x}\text{Y}_{2-x}\text{Cu}_5\text{O}_{10}$ quasi-1D system which were performed in an attempt to extract more information about the magnetic ordering in the copper-oxide chains of this relatively new compound. Currently it is believed that this system exhibits 3D antiferromagnetic long-ranged ordering at low temperatures for zero doping but it transitions to 1D chain behavior, and finally to cluster behavior, as holes are introduced into the system via increasing the doping concentration x . We determined the lineshape of the ^{89}Y NMR signal and measured both the spin-lattice and the spin-spin relaxation times for 2 different dopings of $x = 0$ and $x = 0.5$ at several temperatures within the 250 K–295 K range. From the acquired relaxation times we estimated the correlation times for the spin subsystems involved in interactions with the Y nuclei.

Chapter 2

NMR Fundamentals and Measurement Techniques

2.1 Basic Theory of NMR

Magnetic resonance is a phenomenon which can occur in any system possessing magnetic moments. The term “resonance” suggests that we are examining properties of the matter at a particular frequency natural for the system. Nuclear magnetic resonance, in particular, is a type of magnetic resonance occurring in nuclear systems with magnetic moments and is usually performed using radio (rf) frequencies.

In this chapter we will present a review of the NMR fundamental theory described in many sources (see for example [2, 3, 4]), and will also provide an overview of some of the simplest measurement techniques of pulse NMR spectroscopy used in this study.

2.1.1 The Nuclear Magnetic Resonance Phenomenon

The nuclei consist of many coupled particles, all of which in general possess an angular momentum. The superposition of these spins and orbital moments gives rise to a total angular momentum of the nucleus \mathbf{J} (\mathbf{J} being either an integer or a half-integer multiple of \hbar).

Every nucleus with a nonzero total angular momentum possesses a magnetic moment $\boldsymbol{\mu}$ according to the formula

$$\boldsymbol{\mu} = \gamma \mathbf{J} = \gamma \hbar \mathbf{I} \quad (2.1)$$

where \mathbf{I} is the dimensionless angular momentum operator of the nucleus and the coefficient of proportionality γ , called the “gyromagnetic ratio”, varies with the particular nucleus and nuclear state.

The gyromagnetic ratio is related to the nuclear magneton $\mu_n = e\hbar/2m_n$ (m_n being the mass of the nucleus) via the relation

$$\gamma \hbar = g \mu_n \quad (2.2)$$

where g is a scalar coefficient equivalent to the Landé g -factor for atoms.

From Eq. (2.2) which is not constrained to only nuclear moments, but as well as Eq. (2.1) is a rather general expression, it can be seen that the smaller the mass of the particle, the bigger the gyromagnetic ratio which, in turn, leads to a higher resonance frequency as will be seen later. For instance, electrons which possess about 1,000 times smaller masses than the nuclei, have about 1,000 times higher resonance frequencies, falling in the microwave region.

Let us now place our nucleus in a magnetic field \mathbf{H}_0 . The Hamiltonian describing the interaction between the field and the magnetic moment of the considered particle is

$$\mathcal{H} = -\boldsymbol{\mu} \cdot \mathbf{H}_0. \quad (2.3)$$

Without a loss in generality, we can take the magnetic field to be oriented in the z direction. Then it is found that

$$\mathcal{H} = -\gamma \hbar H_0 I_z, \quad (2.4)$$

I_z being the z component of the angular momentum operator of the nucleus.

The eigenvalues of the Hamiltonian then give us the Zeeman energy levels of our simple system

$$E_m = -\gamma\hbar H_0 m, \quad m = -I, -I + 1, \dots, I - 1, I. \quad (2.5)$$

Eq. (2.5) shows that we have a set of energy levels which are equally spaced, separated by a distance $\gamma\hbar H_0$. An example of the levels for a nucleus with spin $I = 5/2$ is presented in Fig. 2.1.

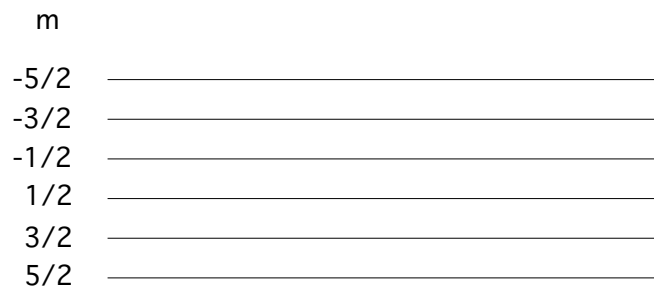


Figure 2.1: Energy levels for a spin 5/2 nucleus. The lowest energy orientation of the magnetic moment is along the field.

If we wanted to detect the splitting of the energy into the discrete levels described above we would have to somehow induce transitions between these levels. The interaction inducing these transitions should be time dependent, with an angular frequency allowing for spectral absorption of the required energy quanta

$$\Delta E = \hbar\omega = \gamma\hbar H_0. \quad (2.6)$$

Therefore, the angular frequency of the interaction should be

$$\omega = \gamma H_0. \quad (2.7)$$

The most common technique used to induce transitions between the energy levels is the application of an alternating magnetic field. From a quantum mechanical point of view, one could argue that this alternating magnetic field should have a perpendicular component to the original magnetic field in order to successfully induce transitions. This comes from the fact (see for instance [5]) that the z component of the angular momentum operator has non-vanishing matrix elements only between the same states, i.e.

$$(m'|I_z|m) \neq 0 \quad \text{only for} \quad m' = m, \quad (2.8)$$

while the perpendicular components of the angular momentum allow transitions between states:

$$(m'|I_{x(y)}|m) \neq 0 \quad \text{for} \quad m' = m \pm 1. \quad (2.9)$$

The last relation also points to the fact that the only allowed transitions for inducing a resonance are between adjacent energy levels. In addition, since the Planck's constant disappeared from (2.7), the results obtained above are closely related to a classical picture.

Let us then consider classically a nucleus with an angular momentum \mathbf{J} placed in an external magnetic field \mathbf{H} . The equation of motion for \mathbf{J} is obtained by equating the rate of change of the angular momentum with the torque created by the magnetic field

$$\frac{d\mathbf{J}}{dt} = \boldsymbol{\mu} \times \mathbf{H}. \quad (2.10)$$

According to Eq. (2.1) the above relation becomes

$$\frac{d\boldsymbol{\mu}}{dt} = \gamma\boldsymbol{\mu} \times \mathbf{H}. \quad (2.11)$$

From this expression we see that the changes in the magnetic moment $\boldsymbol{\mu}$ are always perpendicular to both $\boldsymbol{\mu}$ and the magnetic field \mathbf{H} . Therefore, if the magnetic field is time independent $\boldsymbol{\mu}$ will precess on a cone around the field at a constant angular velocity $\boldsymbol{\Omega} = -\gamma\mathbf{H}$. The corresponding angular frequency $\omega = \gamma H$ is called the “Larmor frequency”. It is the same frequency required for the resonance absorption which we obtained before using the quantum mechanical approach.

In the next subsection we will adopt the classical point of view when considering how the system behaves after the application of a perpendicular alternating magnetic field.

2.1.2 Classical Treatment of Noninteracting Nuclear Moments in an Alternating Magnetic Field

Let us now allow the magnetic field to vary in time. In fact, let us consider a system of two magnetic fields much like the ones used in the majority of the NMR experiments, a large static magnetic field applied in the z direction and, perpendicular to it, a smaller magnitude alternating field, applied for instance in the x direction

$$\begin{aligned}\mathbf{H}_0 &= H_0 \hat{\mathbf{z}} \\ \mathbf{H}_x(t) &= 2H_{x0}\cos\omega t \hat{\mathbf{x}}.\end{aligned}\tag{2.12}$$

The alternating field can be decomposed to two rotating components—one of them rotating clockwise and the other one counterclockwise (Fig. 2.2):

$$\begin{aligned}\mathbf{H}_R(t) &= H_{x0}(\cos\omega t \hat{\mathbf{x}} + \sin\omega t \hat{\mathbf{y}}) \\ \mathbf{H}_L(t) &= H_{x0}(\cos\omega t \hat{\mathbf{x}} - \sin\omega t \hat{\mathbf{y}}).\end{aligned}\tag{2.13}$$

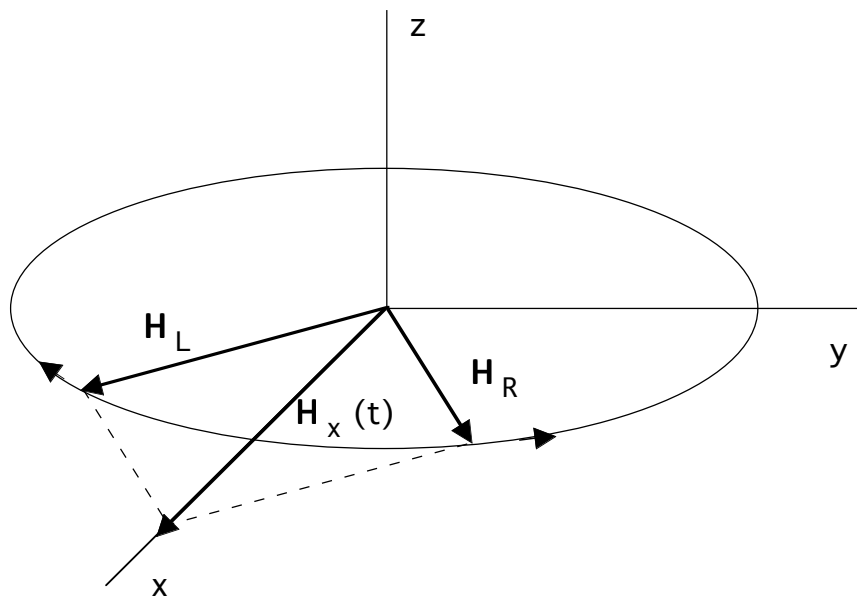


Figure 2.2: The linearly polarized magnetic field $\mathbf{H}_x(t)$ is decomposed to two rotating components \mathbf{H}_R and \mathbf{H}_L .

If we consider now the precessing magnetic moment $\boldsymbol{\mu}$ around the static field \mathbf{H}_0 , one of the components \mathbf{H}_R and \mathbf{H}_L will rotate in the same sense as $\boldsymbol{\mu}$, while the other component will rotate in the opposite sense. Near resonance, that is, when the frequency of the alternating magnetic field is close to the Larmor frequency, the component rotating in the opposite direction may be neglected since it doesn't contribute to the energy level transitions. We shall refer to the contributing component of the magnetic field simply by $\mathbf{H}_1(t)$.

It is very useful at this point to introduce the commonly used rotating reference frame technique for obtaining a simpler and easier to understand picture of the motion of magnetic moments under the influence of a time varying magnetic field.

For this purpose let us consider a frame of reference with unit vectors

$\hat{\mathbf{x}}'$, $\hat{\mathbf{y}}'$, and $\hat{\mathbf{z}}'$, rotating at an angular velocity $\boldsymbol{\Omega}$ with respect to the static laboratory frame with unit vectors $\hat{\mathbf{x}}$, $\hat{\mathbf{y}}$, and $\hat{\mathbf{z}}$. The equation of motion of the unit vectors of the rotating frame in the laboratory frame is described as follows

$$\frac{d\mathbf{i}}{dt} = \boldsymbol{\Omega} \times \mathbf{i} \quad \text{where} \quad \mathbf{i} = \hat{\mathbf{x}}', \hat{\mathbf{y}}', \hat{\mathbf{z}}'. \quad (2.14)$$

Next, let's see how the time derivative of an arbitrary vector \mathbf{A} transforms in the rotating coordinate system:

$$\begin{aligned} \frac{d\mathbf{A}}{dt} &= \frac{dA_{x'}}{dt} \hat{\mathbf{x}}' + \frac{dA_{y'}}{dt} \hat{\mathbf{y}}' + \frac{dA_{z'}}{dt} \hat{\mathbf{z}}' + A_{x'} \frac{d\hat{\mathbf{x}}'}{dt} + A_{y'} \frac{d\hat{\mathbf{y}}'}{dt} + A_{z'} \frac{d\hat{\mathbf{z}}'}{dt} \\ &= \frac{dA_{x'}}{dt} \hat{\mathbf{x}}' + \frac{dA_{y'}}{dt} \hat{\mathbf{y}}' + \frac{dA_{z'}}{dt} \hat{\mathbf{z}}' + \boldsymbol{\Omega} \times (A_{x'} \hat{\mathbf{x}}' + A_{y'} \hat{\mathbf{y}}' + A_{z'} \hat{\mathbf{z}}') \\ &= \frac{\delta\mathbf{A}}{\delta t} + \boldsymbol{\Omega} \times \mathbf{A} \end{aligned} \quad (2.15)$$

where $\delta\mathbf{A}/\delta t$ is the time derivative of vector \mathbf{A} with respect to the rotating coordinate system.

Returning to our single magnetic moment $\boldsymbol{\mu}$ we can write the following equation of motion

$$\frac{d\boldsymbol{\mu}}{dt} = \boldsymbol{\mu} \times \gamma[\mathbf{H}_0 + \mathbf{H}_1(t)]. \quad (2.16)$$

To eliminate the time dependence of the rotating field we can now adopt a coordinate system, with a z' axis coinciding with the z axis of the laboratory frame, which rotates about the z direction at the angular frequency ω of $\mathbf{H}_1(t)$ (Fig. 2.3).

According to our calculations (2.15) the above equation of motion transforms in the new coordinate system as follows

$$\frac{\delta\boldsymbol{\mu}}{\delta t} = \boldsymbol{\mu} \times [\boldsymbol{\Omega} + \gamma(\mathbf{H}_0 + \mathbf{H}_1)]. \quad (2.17)$$

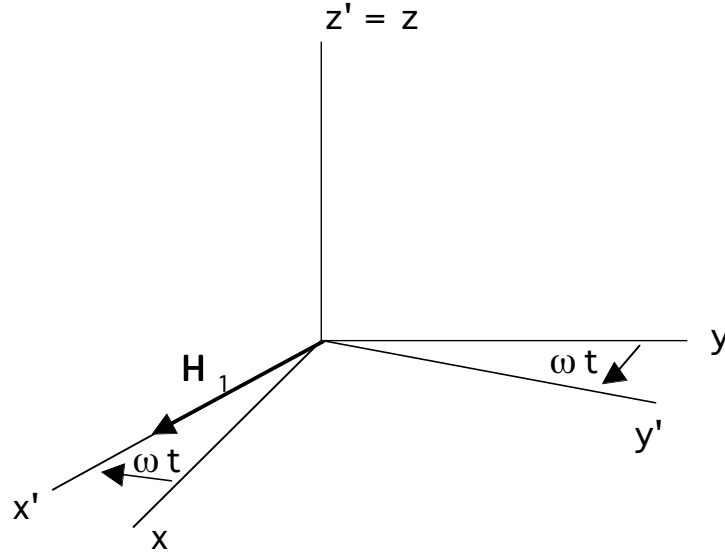


Figure 2.3: The magnetic field \mathbf{H}_1 is static in the new reference frame rotating about the z axis of the laboratory frame with an angular frequency ω .

Thus, with the use of an appropriate reference frame we managed to transform \mathbf{H}_1 into a static magnetic field. Without a loss in generality, let us assume that \mathbf{H}_1 points in the x' direction of the rotating frame. In this case equation (2.17) can be rewritten as

$$\frac{\delta\boldsymbol{\mu}}{\delta t} = \boldsymbol{\mu} \times \gamma \left[H_1 \hat{\mathbf{x}}' + \left(H_0 - \frac{\omega}{\gamma} \right) \hat{\mathbf{z}}' \right]. \quad (2.18)$$

After introducing an effective field

$$\mathbf{H}_{\text{eff}} = \left[H_1 \hat{\mathbf{x}}' + \left(H_0 - \frac{\omega}{\gamma} \right) \hat{\mathbf{z}}' \right] \quad (2.19)$$

(2.18) finally becomes

$$\frac{\delta\boldsymbol{\mu}}{\delta t} = \boldsymbol{\mu} \times \gamma \mathbf{H}_{\text{eff}}. \quad (2.20)$$

From this equation of motion we see that in the rotating reference frame the moment simply precesses in a cone of fixed angle about the static magnetic field \mathbf{H}_{eff} at an angular frequency γH_{eff} . Figure 2.4 shows this precession.

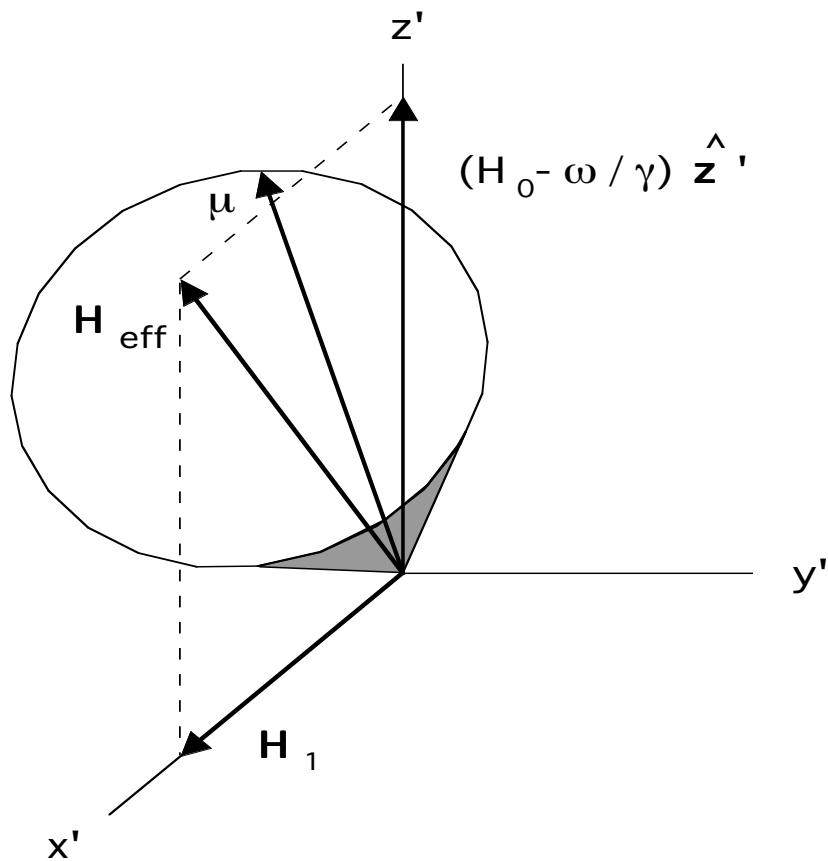


Figure 2.4: Precession of $\boldsymbol{\mu}$ about the effective magnetic field \mathbf{H}_{eff} in the rotating frame.

Since $H_0 \gg H_1$, the potential energy of the magnetic moment $\boldsymbol{\mu}$ can be considered primarily generated by the interaction with H_0 . Therefore, as $\boldsymbol{\mu}$ precesses about \mathbf{H}_{eff} its potential energy in the laboratory frame periodically increases as it is tipped away from the z axis. However, this energy provided by \mathbf{H}_1 is returned back when $\boldsymbol{\mu}$ aligns again with \mathbf{H}_0 . In result, there is no net absorption of energy by the magnetic moment from the alternating magnetic field after any integer number of complete precessional cycles about \mathbf{H}_{eff} .

In the case when the frequency of \mathbf{H}_1 is chosen to satisfy the resonant

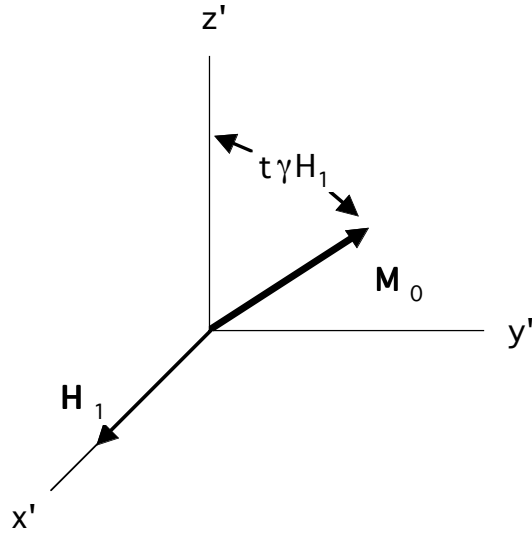


Figure 2.5: The magnetization is tipped by \mathbf{H}_1 —the only remaining component of the effective field.

condition, i.e. to be equal to the Larmor frequency γH_0 , the z' component of the effective field in the rotating frame disappears and

$$\mathbf{H}_{\text{eff}} = H_1 \hat{\mathbf{x}}'. \quad (2.21)$$

In this case, if we start with the magnetic moment parallel to \mathbf{H}_0 , $\boldsymbol{\mu}$ will precess about \mathbf{H}_1 with a frequency $\omega_1 = \gamma H_1$, always staying perpendicular to the field (will be positioned in the y' - z' plane of the rotating reference frame). Therefore, we can use H_1 as means of tilting the magnetic moment to different angles with respect to its original orientation (Fig. 2.5). For instance, the magnetic moment can be tipped to a 90 degree angle by turning on the magnetic field H_1 for an amount of time satisfying the relation $\pi/2 = \omega_1 t$. Such a pulse is referred to as a “ $\pi/2$ pulse”. After turning off H_1 the moment sees no magnetic field in the rotating frame and therefore remains at rest in it. This corresponds to precession with a constant frequency γH_0 in the x - y

plane of the laboratory frame. Similarly, we could apply pulses of different durations, such as, for example, a π pulse to tilt the moment opposite to its original orientation. Furthermore, by changing the phase of the alternating field we can effectively switch its direction in the rotating frame which would allow us to tip the magnetic moment to a certain angle in a different plane.

All these methods of manipulating the nuclear moments are used in the pulse NMR measurement techniques further discussed in the next section.

2.1.3 Bloch Equations

Until this point we considered the motion of a single magnetic moment interacting only with a magnetic field. However, in a real sample we have many such moments which interact not only with the field but also with the lattice. Moreover, they interact among themselves.

Let us consider a macroscopic NMR sample consisting of nuclei of spin $1/2$, for example. If there were no thermal energy and we placed our sample in a magnetic field, all the identical magnetic moments would line up with the field trying to occupy the lower energy state. However, the actual population of the two states depends on the absolute temperature of the sample and the occupation ratio of the spins in the upper energy state to that in the lower energy state at thermal equilibrium is proportional to the Boltzmann factor $\exp(-2\mu H_0/kT)$, where k is the Boltzmann constant and T is the temperature. This population difference gives rise to a macroscopic nonzero magnetization M_0 defined as the sum of all the magnetic moments per unit volume. At room temperature the Boltzmann factor differs from zero only by 10^{-5} – 10^{-6} , so the

precession of the total magnetization usually provides a weak NMR signal.

In general, for nuclei with an angular momentum I the magnetization will be [6]

$$M_0 = \chi_0 H_0 = \frac{n(\gamma\hbar)^2 I(I+1)H_0}{3kT} \quad (2.22)$$

where χ_0 is the static magnetic susceptibility and n is the number of spins per unit volume.

When placing the sample in the static field H_0 the magnetization M_0 does not establish instantaneously, but grows to its equilibrium value over a finite period of time. If we tilt the magnetization with an alternating magnetic field it will try to relax back to its equilibrium value M_0 . Therefore, we can write the following equations of motion for the magnetization

$$\begin{aligned} \frac{dM_z}{dt} &= \gamma(\mathbf{M} \times \mathbf{H})_z + \frac{M_0 - M_z}{T_1} \\ \frac{dM_x}{dt} &= \gamma(\mathbf{M} \times \mathbf{H})_x - \frac{M_x}{T_2} \\ \frac{dM_y}{dt} &= \gamma(\mathbf{M} \times \mathbf{H})_y - \frac{M_y}{T_2}. \end{aligned} \quad (2.23)$$

These equations are called the ‘‘Bloch equations’’ and they describe the magnetization precession about the magnetic field and its tendency to relax towards the equilibrium value.

The first equation introduces the characteristic time T_1 which is called the ‘‘spin-lattice relaxation time’’. This relaxation is due to the energy exchange of the magnetic moments with the thermal reservoir, that is, the lattice. Simultaneously, the transverse components of the magnetization decay to zero with a characteristic time T_2 , which is not necessarily equal to the

longitudinal relaxation time T_1 and is commonly known as the “spin-spin relaxation time”. The difference between the two relaxation times becomes more obvious when we note that the transverse relaxation preserves the energy in the static magnetic field.

One possible mechanism for the relaxation T_2 is a spread in the precession frequencies of the different nuclei induced by differences in the local magnetic fields seen at each site. If the distance between two nearest neighbors in the sample is r the field produced by the magnetic moment of a nucleus in the next site will be $H_{\text{loc}} \propto \mu/r^3$. This field is either adding or opposing the static field depending on the orientation of $\boldsymbol{\mu}$. Hence, we get a spread in frequencies. The dipole interaction described here provides us with a rough estimate of T_2 :

$$T_2 = \frac{1}{\gamma H_{\text{loc}}}. \quad (2.24)$$

There are also other mechanisms giving rise to the relaxation times, and in this sense, the simple exponential decay introduced by the Bloch equations is not always valid. However, these equations are still very useful in providing us with an easy-to-understand picture of the magnetic resonance phenomena. We will not theoretically discuss here the solutions of the Bloch equations for different cases, but instead will refer the reader to [7] and [2] for more information on this subject.

2.2 Measurement Techniques

As we discussed before, we can manipulate the spins in a sample with the use of magnetic fields. We first introduce a big static field to generate a macroscopic

magnetic moment in the sample. After this, we apply an alternating magnetic field to change in various ways the orientation of this magnetic moment. A simple way of introducing the alternating field is to place the sample in a coil positioned perpendicularly to the static field and to apply a sinusoidal voltage to it. To extract the valuable information about the relaxation times associated with our sample we turn off the alternating field after different waiting times and observe the emf induced in the coil by the recovering to its thermal equilibrium value magnetization.

Since the voltage received from the coil is usually very small, signal averaging is required. Many pulse sequences have been developed through the years to accelerate and improve the data acquisition process, and to allow for the extraction of more information from a single measurement. The current section provides a description of different pulse techniques used in the most typical NMR experiments along with the methods used in this work to extract the parameters of interest.

2.2.1 Free Induction Decay, Spin-Echoes, and Spin-Spin Relaxation

In the preceding theoretical discussions, we saw that by applying an alternating magnetic field with a frequency equal to the resonance frequency of our system, we can cancel the z component of the effective field in the rotating frame. Thus, we can use the remaining static field in the x' - y' plane, H_1 , to tilt the magnetization to different angles.

Let us consider the case when we apply a $\pi/2$ pulse of duration

$$t_{\pi/2} = \frac{\pi}{2} \left(\frac{1}{\gamma H_1} \right). \quad (2.25)$$

in the x' direction. This pulse tips \mathbf{M}_0 (Fig. 2.6) along the y' direction. After turning off the rf pulse the magnetization starts to dephase in the rotating frame due to the spread in the resonance frequencies of the nuclei at different sites in the sample. The dephasing magnetization generates an rf signal with decaying envelop in the pick up coil. This decaying signal after the rf pulse is called the “free induction decay” (FID). For a single Lorentzian line the FID decay rate is exponential with a characteristic time T_2^* which is usually much shorter than T_1 in solid samples. Hence, the signal in the pickup coil will totally disappear before any significant part of the magnetization has managed to relax back along z . If we wait more time the magnetization will start growing along the z axis but since the pick up coil is sensitive only to the x and y components of the magnetization no additional signal will be detected.

In general, the time constant T_2^* in liquids can be strongly affected by motion since the molecules in a liquid have more degrees of freedom to reorient and diffuse, which in turn, significantly decreases the average spread in local fields and lengthens T_2 . On the other hand, the transverse dipole effects governing the spin-spin relaxation dominate in solids and the spin-lattice relaxation doesn't play a significant role. In any case, however, a major contribution to the free induction can be due to inhomogeneities of the applied magnetic field. The relation between T_2^* , T_2 , and the spread in the Larmor frequencies induced by the field inhomogeneity ΔH_0 is given by the equation

$$\frac{1}{T_2^*} = \frac{1}{T_2} + \gamma \Delta H_0. \quad (2.26)$$

Since we are interested in determining the properties internal to the sample and not the inhomogeneity of the external magnetic field, a lot of care

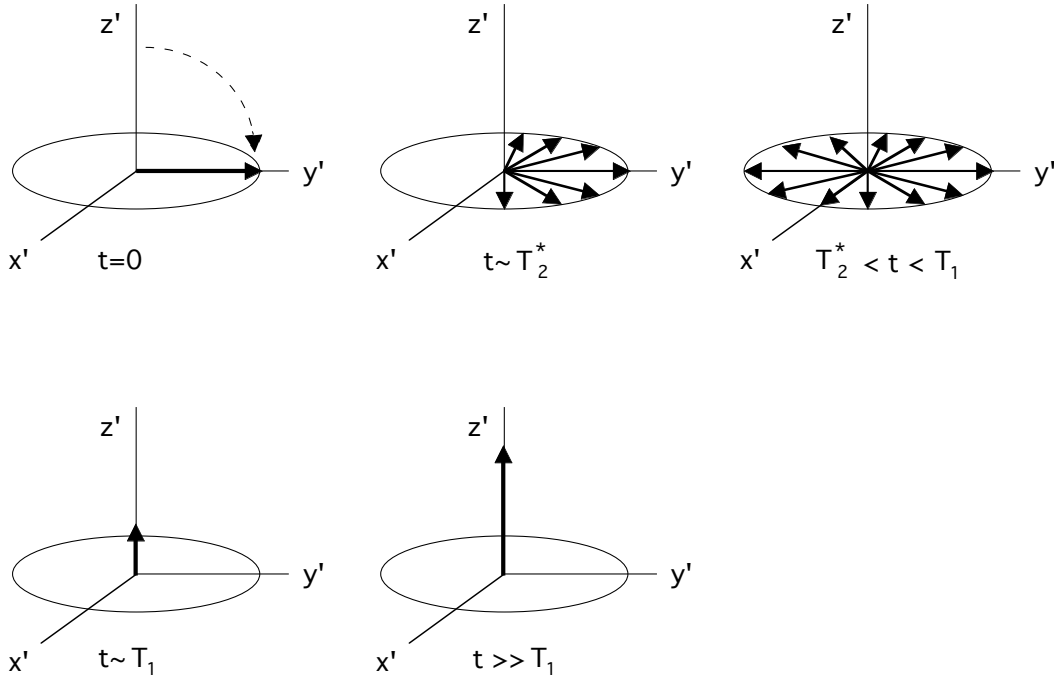


Figure 2.6: After a $\pi/2$ pulse the magnetization dephases in the x' - y' plane with a characteristic time constant T_2^* . After waiting longer times, M_0 relaxes to its thermal equilibrium value along z' but this does not induce a signal in the pickup coil.

is taken to design and build special high-homogeneity NMR magnets. Even with these magnets, though, it is impossible to decrease ΔH_0 so much, that we would have $\gamma\Delta H_0 \ll 1/T_2$.

Therefore, we need a different kind of experiment which can remove the effect of the field inhomogeneity, leaving only the information related to the intrinsic properties of the sample. Such experiments, called the “spin-echo” experiments [8], use the fact that, even though the total magnetization has dephased in the x' - y' plane due to the existence of ΔH_0 , the magnetic moments associated with different small regions in the sample still have not completely dephased due to the internal dipolar interactions. Therefore, if we

could rephase these regions again somehow, we could observe a signal again. This signal will be smaller than the original signal in the FID telling us how fast the internal dephasing in the sample is happening, that is, letting us determine T_2 .

The secondary signal is called a “spin-echo”, or simply an “echo” and is obtained when we apply a π pulse at time τ after the first $\pi/2$ pulse used for inducing the FID (Fig. 2.7). The π pulse, as described in more detail later, causes the spins to refocus in time τ after its application, after which they again slowly dephase with a time constant T_2^* . Thus, the echo obtained basically consists of two FID’s back to back with each other with a maximum signal occurring at time 2τ after the original $\pi/2$ pulse. By monitoring the signal strength of the echo as a function of 2τ we can determine the spin-spin relaxation time T_2 :

$$M(2\tau) = M_0 e^{-2\tau/T_2} . \quad (2.27)$$

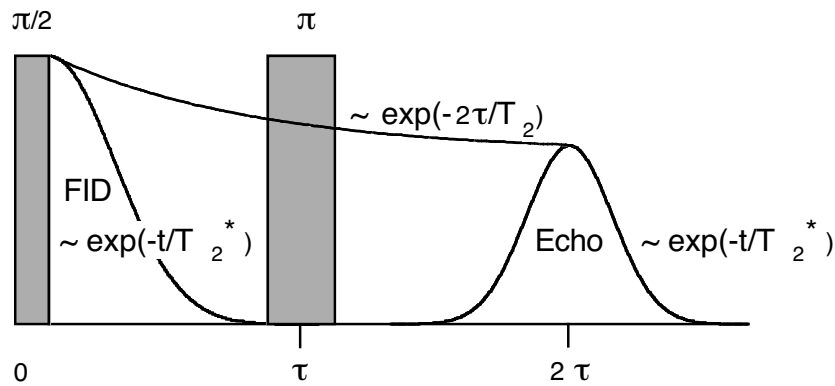


Figure 2.7: $\pi/2 - \tau - \pi$ pulse sequence for inducing an echo.

To understand how the π pulse will refocus the magnetization in the x' - y' plane, let us consider what happens to the individual dephased parts of the

magnetization (see Fig. 2.8). If we apply the π pulse along the x' direction the components of the magnetization will rotate by a 180° angle about x' . Thus, the faster components will now be behind the on-resonance component and the slower components will be ahead. As time elapses, the faster components will start to catch up with the on-resonance component, while the slower ones will lag and thus also get closer to it. Eventually, all components will rephase giving us the maximum echo signal. Since the rephasing will happen in the negative y' direction, we will obtain a negative echo. After the rephasing was completed the different magnetization components again start to spread out in the x' - y' plane producing the second decreasing in magnitude part of the echo.

If we prefer to have a positive echo we have to apply the π pulse in the y' direction instead of the x' direction of the rotating frame. Then the components of the magnetization will be rotated by a 180° angle about y' and will refocus along the positive y' direction as shown in Fig. 2.8(b).

Many elaborate techniques using more than two pulses in a sequence have been developed to shorten the data acquisition process. However, we will constrain our considerations only to generating single echoes and will refer the reader to the literature elsewhere ([9, 10, 11]) for more information on this subject.

2.2.2 Spin-Lattice Relaxation

The most commonly described spin-lattice relaxation has an exponential behavior which the samples under consideration in this study are believed to

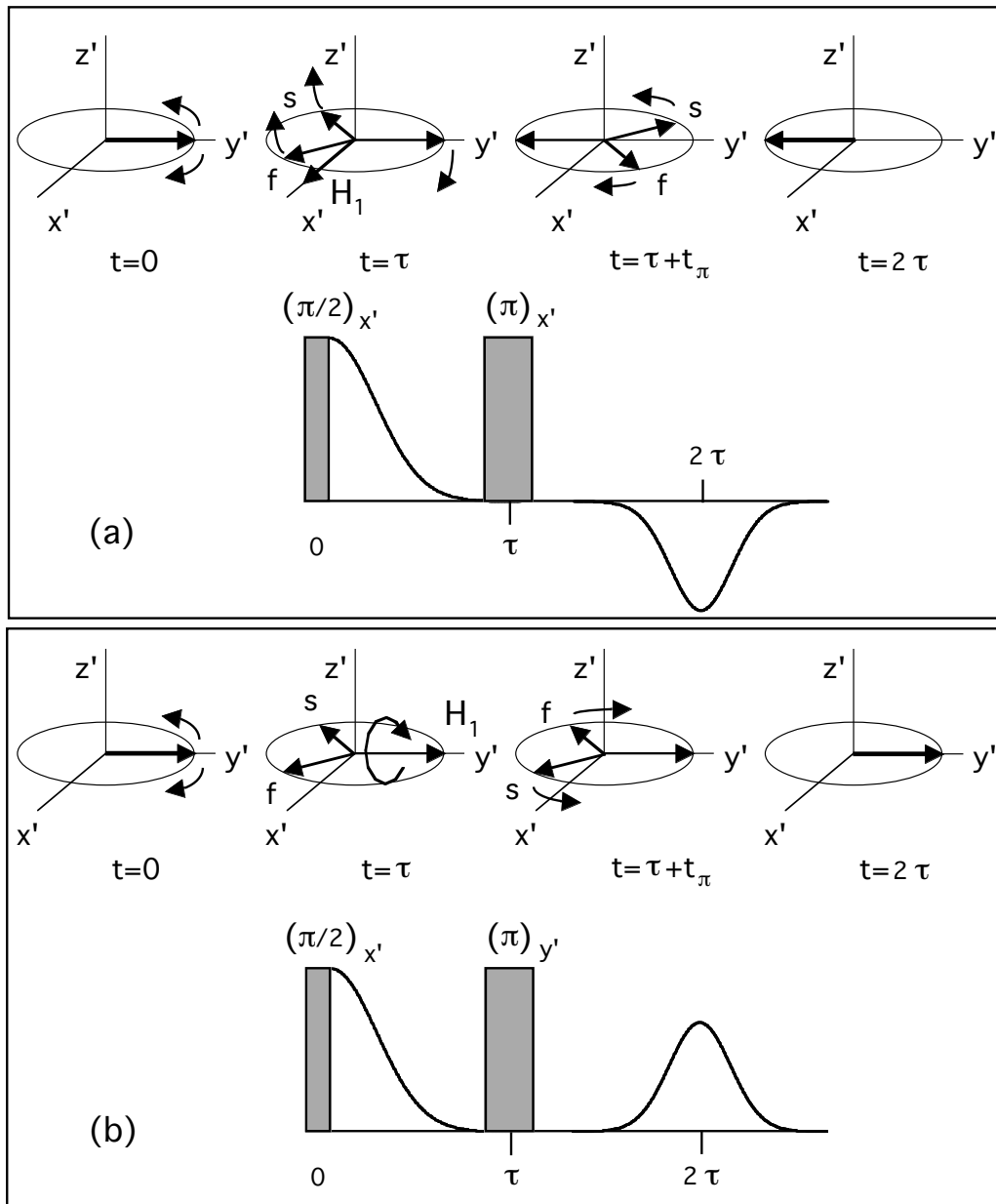


Figure 2.8: (a) Inducing a negative echo by applying a π pulse along the x' direction at time τ after the $\pi/2$ pulse. (b) Inducing a positive echo by applying the π pulse along the y' direction.

possess and to the discussion of which we will constrain ourselves here.

Measuring the spin-lattice relaxation time T_1 is usually a time consuming task, especially when dealing with long T_1 's. There are two popular techniques [3] for performing a T_1 measurement, both of which employ a first pulse (or a sequence of pulses) that prepares the spins in the sample, and a second pulse (or a sequence of pulses) which measures the magnetization in the sample after some recovery time t .

The first technique, called the inversion recovery, involves inverting the magnetization from its thermal equilibrium value M_0 to $-M_0$ by applying a π pulse and then monitoring it relax back to M_0 either by inducing a free-induction decay via a $\pi/2$ pulse or alternatively by observing an echo after a $\pi/2 - \tau - \pi$ sequence. Observing the echo is advantageous for eliminating the contributions to the signal from spurious ringing in the NMR spectrometer after the rf pulses.

Ideally, the time dependence of the magnetization relaxation after an inversion recovery sequence is described by the following equation

$$M(t) = M_0(1 - 2e^{-t/T_1}), \quad (2.28)$$

from which the spin-lattice relaxation time T_1 can be extracted.

The second measurement technique for determination of T_1 is the saturation recovery pulse sequence. It involves applying a $\pi/2$ pulse which puts the magnetization into the x' - y' plane leaving zero magnetization along the z axis and after some waiting time applying another $\pi/2$ pulse to observe the FID from the partially relaxed back magnetization or a $\pi/2 - \tau - \pi$ sequence for obtaining an echo.

The recovery law in this case looks as follows

$$M(t) = M_0(1 - e^{-t/T_1}). \quad (2.29)$$

An advantage of using the inversion recovery sequence is that the data acquired this way has twice the dynamic range of the data acquired by using the saturation recovery sequence. However, there are some drawbacks to it. For instance, the π pulse has only half of the frequency spectrum of the $\pi/2$ pulse since it is twice as wide in the time domain, which yields in a less accurate intensity and line shape determination of signals acquired from samples with broad lines. Also, when using the saturation recovery it is not necessary in principle to wait a long time between the consecutive sequences, since we always set $M_z = 0$ with the first pulse. On the contrary, when using the inversion recovery it is required to have a several T_1 time separation between the sequences so we can set the magnetization to $-M_0$ with the first pulse. This difference between the two techniques can lead to a big time advantage for the saturation recovery when $T_2 < T_1$. In the case of relatively short relaxation times, however, the last mentioned advantage cannot really be employed because of the incapability of the NMR probe to withstand higher dissipated average power and because of triggering time restrictions in the digital oscilloscope.

It is necessary to point out here that both of the sequences described above are often implemented with pulses the duration of which deviates from the ideal one for a $\pi/2$ (π) pulse. The reason for this is that sometimes the weak signal to noise ratio simply doesn't allow for the exact determination of the $\pi/2$

(π) pulse length. In this case, we still keep the relaxation information but the formula describing it will depend on the actual tip angle of the magnetization.

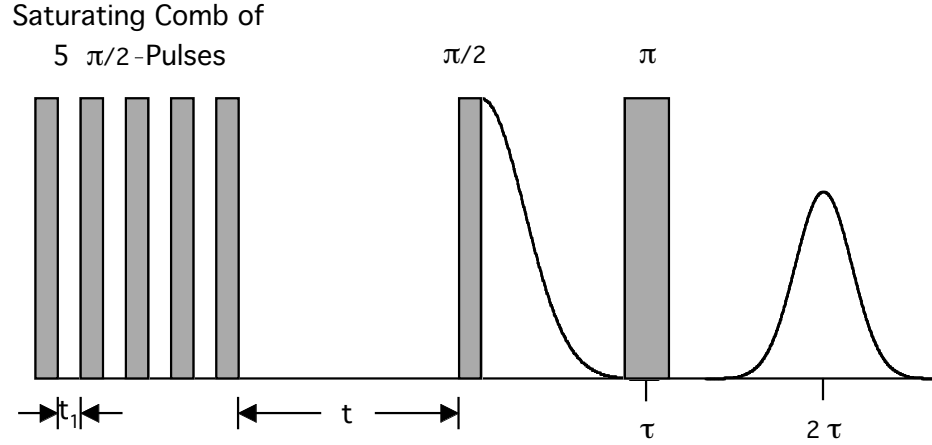


Figure 2.9: Saturating comb of 5 $\pi/2$ pulses separated by time t_1 is used for destroying the initial magnetization. T_1 is detected by monitoring the echo strength growth as a function of t .

A way to fix the problem with not having a perfect length of the $\pi/2$ pulse is to use a number of $\pi/2$ pulses forming a so-called saturating comb instead of just one $\pi/2$ pulse to set the initial condition of zero magnetization in the z direction (see Fig.2.9). By spacing the pulses in the comb by a time t_1 satisfying the condition $T_2^* < t_1 \ll T_1$ we will actually ensure that the whole magnetization is set to zero by the comb and not only its z component. Depending on the deviation of the pulses from the perfect $\pi/2$ length it is required to choose an appropriate number of pulses in the saturating comb.

In the present study the T_1 measurements were performed using the saturation recovery technique. The number of pulses in the saturating comb was usually set to five.

2.2.3 Spin-Lattice Relaxation in the Rotating Frame

The technique for determination of the rotating frame relaxation time $T_{1\rho}$, which were to be utilized in the $\text{YBa}_2\text{Cu}_3\text{O}_7$ measurements we planned to perform, is described here. A review of other experimental methods for determination of $T_{1\rho}$ is presented in [12].

First, a $\pi/2$ pulse is applied, let's say in the x' direction of the rotating frame which tips the magnetization along the y' axis (Fig.2.10). Then instantaneously the phase of the alternating magnetic field is shifted by 90° in the laboratory frame, which in the rotating frame corresponds to suddenly aligning H_1 with y' . The magnetization in the rotating frame experiences only the field H_1 and it is said that it becomes spin-locked to it. The magnetization before applying the alternating field was aligned along the static field H_0 and had a magnitude of

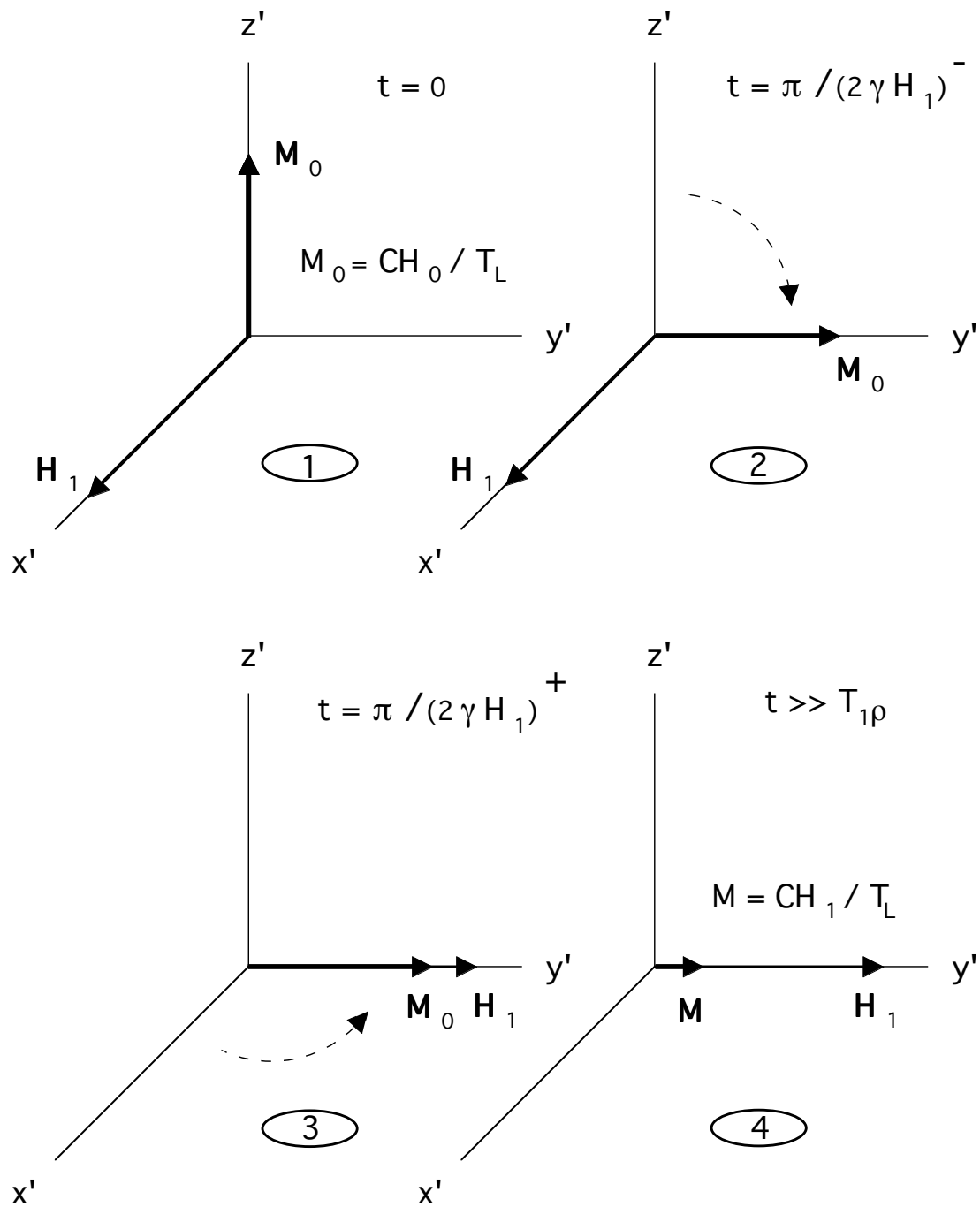
$$M_0 = \frac{CH_0}{T_L} \quad (2.30)$$

where C is the Curie constant (see (2.22)) and T_L is the lattice temperature. However, after the spin-locking rf pulse is applied the magnetization is aligned along a much smaller field H_1 and therefore starts to relax exponentially with a characteristic time constant $T_{1\rho}$ to its new much smaller thermal equilibrium value

$$M = \frac{CH_1}{T_L}. \quad (2.31)$$

Alternatively, we could think that after the initial spin-locking the magnetization has a much lower spin-temperature than its lattice-temperature, according to the following formula

$$\frac{CH_0}{T_L} = \frac{CH_1}{T_S} \quad (2.32)$$

Figure 2.10: $T_{1\rho}$ measurement sequence.

and that the spin-temperature starts to warm up to the lattice temperature with a time constant $T_{1\rho}$.

The relaxation can be observed by turning off the spin-locking pulse after a waiting time t which will result in the magnetization starting to disperse in the x' - y' plane so we can monitor the FID, or alternatively, the echo strength as already discussed above. The magnetization time evolution as a function of the waiting time t follows the law

$$M(t) = M_0 e^{-t/T_{1\rho}} . \quad (2.33)$$

It is worth noting that

$$T_2 \leq T_{1\rho} \leq T_1 \quad (2.34)$$

since if the spin-locking magnetic field H_1 were zero, $T_{1\rho}$ would be simply equal to T_2 and if H_1 were equal to the static field H_0 , then $T_{1\rho}$ would be equal to T_1 . Still, even when $T_2 \ll T_{1\rho}$ the magnetization, being locked to H_1 , will not dephase in the rotating frame until we actually turn off the locking field.

The relaxation time $T_{1\rho}$ will be mostly affected by motions in the sample occurring at the Larmor frequency in the rotating frame $\omega_1 = \gamma H_1$. Since the alternating magnetic field H_1 is much smaller than the static field H_0 and is of the order of gauss, $T_{1\rho}$ is usually sensitive to very slow motions at frequencies of the order of kHz. Of course, it is possible to probe those low frequency motions by lowering the static field H_0 but we would lose a lot of our signal sensitivity since S/N is proportional to H_0^n where $1 < n < 2$ [3]. By varying H_1 and using the $T_{1\rho}$ technique we can gather information about different low

frequency motion regimes in our sample while taking advantage of the good sensitivity of the high-field measurement.

Chapter 3

Experimental Set-Up and Considerations

3.1 Overview

In our set-up (Fig. 3.1), the NMR experiment is conducted using a single coil to produce the alternating magnetic field for manipulation of the spins in the sample, and to detect the signal induced by the relaxing magnetization after the pulses in the coil are turned off. The coil is located in a low temperature NMR probe which, in turn, is part of a tank circuit.

We use a “home-made” NMR spectrometer to generate the rf pulse sequences used in the experiments. We amplify further the pulses using an ENI 5100L-NMR broadband power amplifier, which provides 50 dB of gain in the frequency range 5-400 MHz. After this amplification, the pulses are transferred to the tank circuit and into the coil.

The signal detected by the coil is amplified by a preamplifier and then sent to the receiving part of our spectrometer. Finally, the quadrature outputs from the receiver are averaged and recorded by a Nicolet Pro 30 digital oscilloscope.

The purpose of the preamplifier is to amplify the tiny signal coming from the coil (usually of the order of microvolts) while adding very little noise

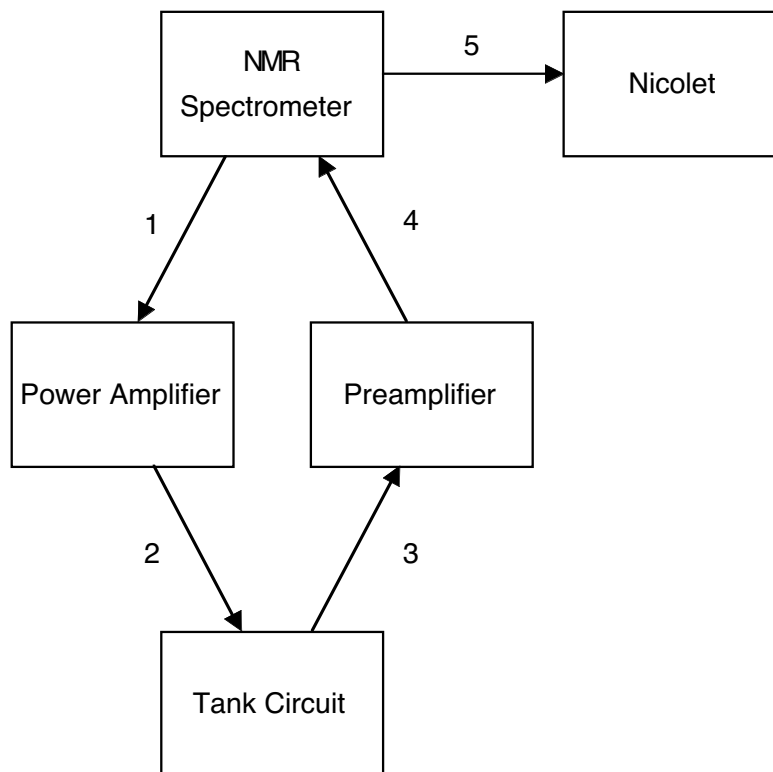


Figure 3.1: Experimental set-up.

to it. Thus, it consists of two low-noise Avnet UTO-511 and GPD-401 amplifiers with gains of 15 and 13 dB, respectively, which are mounted in a box for better noise isolation. Special care is taken for good grounding for the same reason.

To produce the static magnetic field we use a Cryomagnetics, Inc. superconducting NMR magnet. For our low temperature measurements we use a Janis cryostat, model SVT-200T option 5, the tail of which is specifically designed to fit into the 3.50" diameter bore of our magnet and is equipped with a Lakeshore, model CX-1050 calibrated Cernox thermometer located at the bottom of the sample space. A Neocera LTC-21 temperature controller is

used to display the temperature inside the probe and to monitor and control the temperature in the sample space.

Below follows a more detailed description of the different components of the set-up.

3.2 The Tank Circuit

3.2.1 Tank Circuit Requirements

The purpose of the NMR tank circuit is to transfer the full power of the pulses coming from the power amplifier into a resonance circuit containing the NMR coil, and to transmit all of the signal induced in the coil back out of the probe and into the preamplifier.

Many variations of the realization of the tank circuit exist [3, 13] but, no matter what the particular realization, there are several requirements to the design of the tank circuit which have to be satisfied [14]:

1. The alternating field H_1 produced by the coil should be as homogeneous as possible throughout the sample space and it should be strong enough to tip the spins in a major portion of the NMR line.
2. The weak NMR signal should be fully collected and sent to the receiver with a maximum signal-to-noise ratio S/N.
3. The rf power pulsed into the coil should be dissipated as quickly as possible to allow for faster ring-down of the receiver.
4. The transmitter and the receiver should be decoupled from one another

and there should be no rf energy at the resonant frequency irradiated in the vicinity of the NMR experiment.

The signal-to-noise ratio of the detected signal is simply the ratio of the voltage induced in the coil by the relaxing spins to the Johnson noise V_n [15] given by the Nyquist formula

$$V_n = \sqrt{4kTRB} \quad (3.1)$$

where k is the Boltzmann constant, T is the temperature, R is the effective resistance of the circuit, and B is the bandwidth. At room temperature and for a $50\ \Omega$ resistance the Johnson noise is about $0.9\ \text{nV}/\sqrt{\text{Hz}}$ and since we operate with a bandwidth from kilohertz to megahertz the noise can become a big competitor of the small NMR signal.

In general, the signal to noise ratio is proportional to:

$$S/N \propto \zeta \gamma I(I+1)(QVf_0T_2/T_1B)^{1/2} \quad (3.2)$$

where ζ is the filling factor of the coil, γ is the gyromagnetic ratio of the nucleus, I is the spin of the nucleus, V is the volume of the coil, f_0 is the resonant frequency, T_1 and T_2 are the spin-lattice and the spin-spin relaxation times respectively, B as above is the bandwidth, and Q is the quality factor of the resonance circuit, defined as the stored energy in the circuit multiplied by the angular resonance frequency and divided by the power loss [16]:

$$Q = \omega_0 \frac{\text{Stored Energy}}{\text{Power Loss}} = \frac{\omega_0}{\Gamma} \quad (3.3)$$

where Γ is the full width at half-maximum of the power line shape.

After selecting the particular nucleus we would like to experiment on, the parameters left for variation in formula (3.2) are the filling factor of the coil, its volume, and the quality factor of the circuit. To increase the filling factor ζ the coils should be wound in such a way that the samples fit tightly inside them, and special care should be taken to decrease all stray inductances in the resonance circuit which effectively decrease ζ [17]. The volume of the coil should be increased as much as possible, still taking into consideration that the sample should not be larger than a couple of cubic centimeters—the size of the homogeneous region of the static magnetic field. The quality factor can generally be increased by increasing the inductance of the coil and by reducing its resistance. Therefore, the coils should be wound using a wire made of good conducting materials, such as silver or copper, and generally should have many turns. However, for tuning purposes at higher frequencies we make coils with less turns which decreases the inductance. In general, the quality factor increases when lowering the temperature due to the decrease in resistance of the tank circuit with T . But because it is related to the ring-down time of the rf pulses via the formula [14]

$$Q \approx 1.5f_0T_r \quad (3.4)$$

a conflict appears between the requirements for good signal to noise ratio and fast ring-down of the coil. It is even sometimes necessary to artificially decrease the quality factor of the resonant circuit at low temperatures if it becomes so big that it interferes with the proper detection of the signal due to ringing induced by the coil in the receiver.

The homogeneity of the rotating field H_1 is achieved by equally spacing

the windings of the coil and by making it a little longer than the sample in order to prevent the sample from residing inside the fringing fields at the edges of the coil. Unfortunately, the requirement for homogeneity of the alternating field is somewhat in contradiction with the desire to increase the coil filling factor and with the requirement to have as large H_1 as possible.

The strength of the alternating magnetic field is given by the formula [2]

$$H_1 = \sqrt{\frac{10PQ}{f_0V}} \quad (3.5)$$

in which H_1 is measured in gauss, the power P in watts, the resonant frequency f_0 in MHz, and the volume V in cm^3 .

According to this formula we see that again we should try to increase the quality factor of the coil, and we should try to provide as much power as possible to it, but we should actually try to decrease the volume of the coil. The last requirement is at odds with the requirement for increasing the volume in order to improve the signal-to-noise ratio.

In conclusion, when building the tank circuit, one should try to satisfy several requirements for the strength and homogeneity of the rotating field H_1 , the detection and prevention of noise degradation of the signal, and the recovery time of the system from the high power rf pulses. Some of the goals we try to achieve when building the tank circuit impose mutually exclusive requirements on various parameters, and one should only try to do their best in selecting these parameters in a way to optimize the overall results.

3.2.2 Operation of the Tank Circuit and Tuning Considerations

The tank circuit configuration chosen in our experimental set-up is shown in Fig. 3.2. The first crossed-diode box in the tank circuit positioned before the probe prevents the signal coming from the coil from returning to the power amplifier since the diodes turn on at a voltage much higher than the signal detected by the coil. Thus, ideally, we collect all of our signal. The second crossed-diode box is located on a $\lambda/4$ distance after the resonance circuit, where λ is the wavelength of the rf pulses. This box doesn't allow the small signal detected by the coil to be shorted, but effectively looks like 0 impedance for the huge pulses coming from the power amplifier resulting in infinitely high impedance at the point touching the top of the probe. This is so because a zero impedance transforms to infinite impedance when one adds a quarter wavelength of transmission line [18]. This trick gives us the opportunity to transfer all of the power from the power amplifier into the probe, while it doesn't allow it to continue towards the sensitive low signal level amplifiers inside the preamplifier, and further, into the receiver.

Because we are operating at radio frequencies, we need to provide impedance matching throughout the circuit in order to prevent power losses due to various reflections of the signal.

The theory of transmission lines [18, 19] provides us with a general expression for the input impedance at each point of the transmission line as a function of the distance from the load:

$$Z(l) = Z_0 \left(\frac{e^{i\beta l} + \rho_L e^{-i\beta l}}{e^{i\beta l} - \rho_L e^{-i\beta l}} \right) \quad (3.6)$$

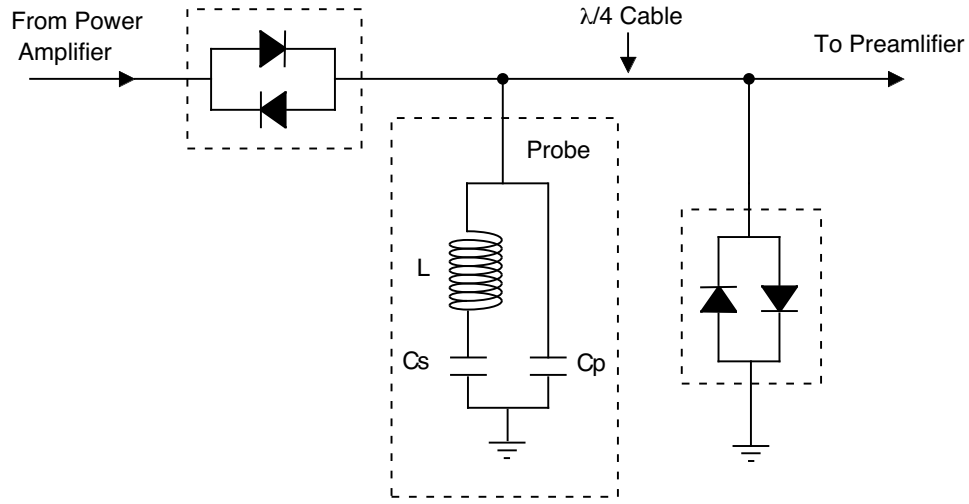


Figure 3.2: Tank circuit.

where l is the distance from the load, β is the wavenumber of the voltage wave propagating in the transmission line

$$\beta = 2\pi/\lambda, \quad (3.7)$$

ρ_L is the reflection coefficient at the load defined as the ratio of the reflected to the forward amplitude of the voltage wave

$$\rho_L = \frac{V_-}{V_+}, \quad (3.8)$$

and finally, Z_0 is the characteristic impedance of the transmission line which for the ideal transmission line is given by the formula

$$Z_0 = \sqrt{\frac{L_0}{C_0}}, \quad (3.9)$$

where L_0 and C_0 are respectively the distributed series inductance and shunt capacitance of the line.

At the load, formula (3.6) transforms into

$$Z_L = Z_0 \left(\frac{1 + \rho_L}{1 - \rho_L} \right) \quad (3.10)$$

from which it is easily seen that the reflection coefficient vanishes when the load impedance is matched to the characteristic impedance of the transmission line.

Since we use standard 50Ω coaxial cables, we need to tune the resonance circuit of the coil to the same impedance. For the purposes of tuning, we form the resonance circuit by adding two variable capacitors to the coil, one parallel to it, and the other in series. Assuming the coil has a small resistance r , one can calculate the real and imaginary parts of the impedance of the circuit and to set them to 50Ω and 0 respectively to find the following relations:

$$Z = \frac{(r + i\omega_0 L - i/(\omega_0 C_s)) (-i/(\omega_0 C_p))}{r + i\omega_0 L - i/(\omega_0 C_s) - i/(\omega_0 C_p)} \quad (3.11)$$

$$\text{Re } Z = 50 \Omega, \quad \text{Im } Z = 0 \quad (3.12)$$

$$50 \Omega = \frac{r/(\omega_0^2 C_p^2)}{r^2 + (\omega_0 L - 1/(\omega_0 C_s) - 1/(\omega_0 C_p))^2} \quad (3.13)$$

$$0 = r^2 + (\omega_0 L - 1/(\omega_0 C_s))(\omega_0 L - 1/(\omega_0 C_s) - 1/(\omega_0 C_p)) \quad , \quad (3.14)$$

where C_p is the parallel capacitance, C_s is the series one, L is the inductance of the coil, and $\omega_0 = 2\pi f_0$ is the angular resonance frequency.

Equations (3.13) and (3.14) show theoretically that the use of two capacitors allows us to tune at different frequencies (to perform NMR on different

nuclei) using the same coil. In reality however, we make a different coil for each experiment because of the limited range of the variable capacitors.

We perform the tuning of the probe on a Smith chart using an HP 8753B network analyzer which generates a test signal at the selected frequency and measures the signal's reflection from the point of interest which in our case is the top of the NMR probe.

3.3 The Probe

In the experiments described in this work, a low temperature NMR probe was used which was constructed by Ruiqi Tian [20]. During the course of the measurements, a number of alterations were made to the original design of the probe in order to improve its functionality and to ease the process of data acquisition.

The probe contains the NMR coil and its resonant circuitry (Fig. 3.3). It provides us with the ability to adjust precisely the position of the coil with the sample inside the magnet so they reside in the highly homogeneous region of the magnetic field, and to be able to tune the resonance circuit from outside the magnet. It also allows us to perform low temperature measurements by separating the coil from the rest of the temperature-sensitive circuitry.

The body of the probe is a 1.625" outer diameter, 0.025" thick stainless-steel tubing that is nonmagnetic and keeps the heat transfer from the top of the probe to its bottom to a minimum. A wider bottom part designed to fit in the 2.5" inner diameter tail of the Janis cryostat is used to accommodate the tuning capacitors, a heater, and a thermometer. A common arrangement

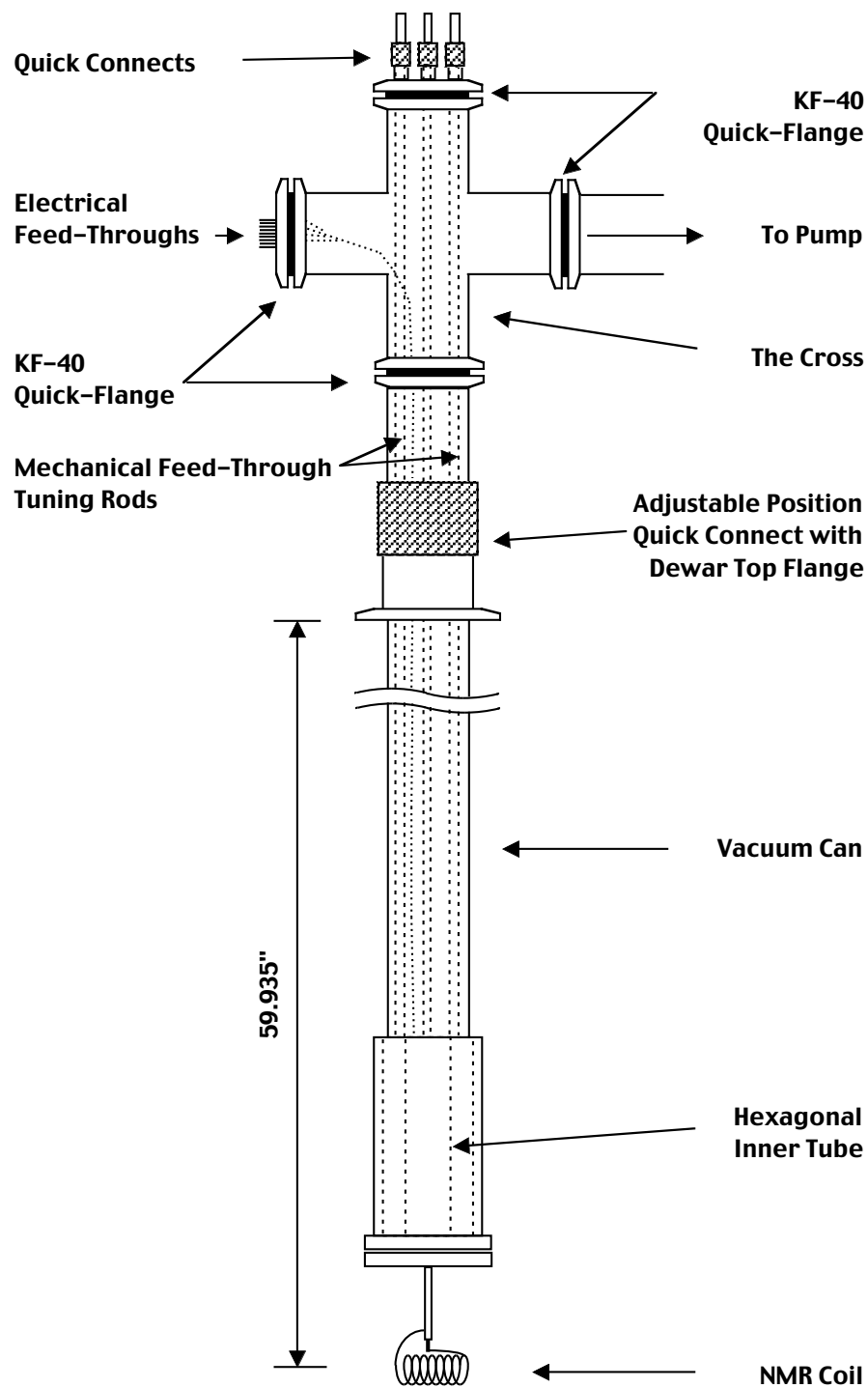


Figure 3.3: Diagram of the low temperature NMR probe.

in a NMR probe is to have the capacitors at the top of the probe, outside the magnet, but such an arrangement, even though easier to implement, allows for big resistive losses in the tank circuit and decreases the quality factor. In our probe we have the capacitors close to the coil reducing the extra resistance and so improving the quality factor of the resonance circuit. We use a 0.141" diameter $50\ \Omega$ semi-rigid rf coaxial cable to lead the signal from the top of the probe to the coil and back, but in our case this semi-rigid cable acts only as a transmission line and provides no appreciable additional losses.

The top of the vacuum can connects to a cross via a KF-40 quick-flange. One side of the cross is used to connect to a pumping station, and the other side provides the electrical feed-throughs for the heater and the thermometer which utilize a 9-pin mini-hex connector mounted on a KF-40 quick-flange and sealed with Stycast 1266 epoxy for maintaining vacuum. The top of the cross is connected to another KF-40 quick-flange with 3 quick-connect couplings soldered to it which provide vacuum-tight access to the probe for the $50\ \Omega$ semi-rigid coaxial cable and the mechanical feed-through rods for the tuning capacitors.

The probe body is adapted to a Triclover flange which serves as a top seal for the Janis cryostat. The flange is soldered to a 1.625" inner diameter quick-connect, the position of which along the length of the can is adjustable for proper vertical positioning of the NMR coil in the field of the magnet. Important dimensions to be taken into consideration here are the 26.125" distance from the center of the homogeneous region of the field to the top of the magnet and the 33.81" distance from the bottom of the mounting flange of

the Janis dewar to its top end. Thus the overall distance from the homogeneous field center to the top flange of the dewar is 59.94", or almost exactly 5 feet.

The bottom of the vacuum can is sealed with a custom-made flange using a 0.015" Pb-4%Sb wire, which was preferred over an indium wire for easier demounting. A more detailed picture of the bottom portion of the probe is provided in Fig. 3.4.

Initially, the same tuning capacitors were used for both the series and the parallel capacitances in the resonance circuit, namely, Voltronics nonmagnetic glass dielectric trimmer capacitors, model NMTM120CEI with a 2–120 pF capacitance range, a quality factor of 350, and 1000 V DC working voltage. The capacitors are cylindrically shaped and have #10-32 threaded ends via which they were mounted on a 0.125" thick hexagonal phenolic plate. The optional plastic extended shafts are used to couple the capacitors to the mechanical feed-through tuning rods using #0-80 set screws. Later, we discovered that the DC working voltage (DCWV) of the NMTM120C capacitors was too low for the series side of the tuning circuit where under resonance conditions the coil and the capacitor operate at a voltage equal to that provided by the power amplifier voltage multiplied by the quality factor of the circuit. Thus, the series capacitor needed to be replaced by one with a higher DCWV which wouldn't clip the voltage delivered to the coil. The Voltronics NMNT23-6EI was selected as a replacement due to its high DCWV of 3000 V, and because its dimensions allowed for it to be incorporated in the probe with little change—its threaded end size #1/4-32 allowed us to mount the capacitor to the phenolic plate after slightly opening the hole left from the

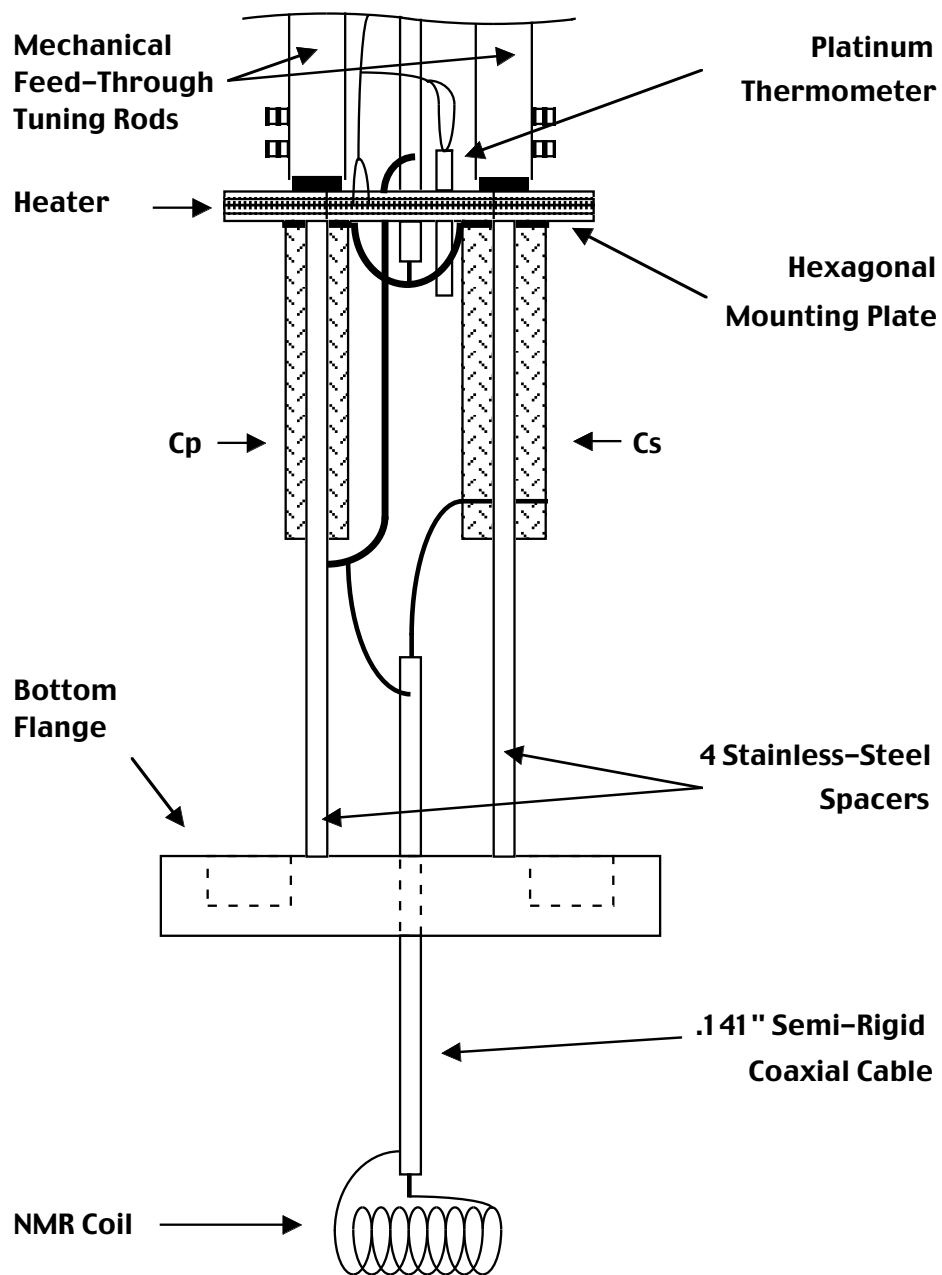


Figure 3.4: Details of the bottom of the probe.

previous capacitor. Other advantages of the NMNT23-6EI are its plastic dielectric which makes the capacitor less brittle, and its higher quality factor of 2200. A disadvantage of the new capacitor is its smaller capacitance range of 3–23 pF which makes the tuning task even harder.

An inner hexagonal stainless-steel tube is mounted inside the bottom part of the vacuum can. The hexagonal phenolic plate can slide in and out of this tube freely when work is done on the probe, but provides a fixed position for all the parts at the bottom when the probe is closed, thus, absorbing the mechanical stress associated with the rotation of the mechanical feed-through rods and resulting in less fluctuations during tuning. Four stainless-steel supporting rods are mounted between the phenolic plate and the bottom flange via their #2-56 threaded ends. The four spacers transfer the weight of the tuning rods, semi-rigid coaxial cable, and the capacitors to the bottom flange of the probe alleviating the stress from the fragile electronic circuitry.

A hole was drilled in the center of the bottom flange to pass the semi-rigid coaxial cable which makes the connection between the capacitors and the NMR coil. Originally, the cable was soft-soldered to the flange. However, the original piece of semi-rigid cable was replaced due to decreased quality of the insulator after it was operated for a period of time at a higher voltage than recommended in its specifications. Stycast 2850FT black epoxy was used to seal the flange for the new cable to prevent the worsening of the insulator quality when heated during soldering.

The original design of the bottom of the probe included a number of short pieces of semi-rigid coaxial cable connected via SMA connectors which

provided us with easier dismounting capabilities. During the course of the measurements though, they were all removed to achieve higher stability of the circuitry. The SMA connector beneath the probe which provided the connection to the coil was removed due to numerous failures to withstand the high voltage at this point of the circuit. This made the change of coils impossible if they were embedded fully in Stycast 1266 epoxy as in the past. Because of this, the new coils are covered only with a thin layer of epoxy which keeps their arrangement fixed and thus prevents impedance variations. In addition, it was found that the mechanical ringing of the coil during the rf pulses is not strong enough to affect the data acquisition process even when the coil is not fully embedded in epoxy.

The tuning capacitors cannot operate at low temperatures; they freeze and cease turning, cracks can develop in the glass insulator during fast temperature changes. Therefore, heating the inside of the probe to near room temperature is required during the low temperature measurements. The first design of the probe had a heater wrapped directly around each of the two capacitors. However, the intolerance of the Voltronics capacitors to high temperatures and the inconvenience of providing a new heater with each capacitor replacement led to moving the heater assembly away from the capacitors and placing it in a specially made groove around the phenolic plate. The heater is made of manganin wire with $12\ \Omega/\text{ft}$ linear resistance and has an approximate resistance of $37\ \Omega$. The electrical feed-through wires are 4 couples of #36 insulated copper wires which provide minimum heat transfer from the top of the probe to the bottom. A Lakeshore PT-103 platinum thermometer is mounted in a hole in the hexagonal phenolic plate and is used for monitoring

the temperature inside the probe.

3.4 The NMR Spectrometer

The 160 MHz intermediate frequency NMR spectrometer was constructed by Jonathan Cobb, based on a description in [17], and its original configuration is thoroughly discussed in his Ph. D. thesis [21].

The purpose of using a fixed intermediate frequency throughout the spectrometer is to have the majority of its circuitry operating always under the same conditions independently of the particular experiment or of frequency drifts within the same experiment. Thus, we ensure the consistency of the signal amplification inside the spectrometer, and therefore the consistency of our results.

This section provides a brief general description of the operation of the spectrometer and talks in detail about the changes made to it, and about different signal level considerations.

3.4.1 Spectrometer Operation

The spectrometer circuitry begins (Fig. 3.5) with a pulse programmer consisting of a main clock and four channels which generate programmed TTL pulse sequences. The pulse programmer was constructed by Vivek Ghante, Ruiqi Tian, and Jeff McGuirk. Its circuitry is described in [22] and will not be discussed here. The TTL signals from the programmer are converted inside the switch driver to -8 V/ground levels before being used by the rf switches inside the spectrometer. The spectrometer transmits during the TTL highs

and receives during the TTL lows. In addition, the main clock generates the 10 MHz sinusoidal signal used for the production of the 160 MHz intermediate frequency, and the four channels provide on their front panels $1.2 \mu\text{s}$ long TTL pulses for external triggering of the Nicolet digital oscilloscope.

The 10 MHz signal generated by the main clock after passing through a 10 MHz filter is sent to the doubler box where it is doubled four times to produce the 160 MHz intermediate frequency signal. This signal is split to four parts. Two of them are sent to the front panel of the spectrometer for diagnostics, the third part is passed through a variable phase shifter and then sent to the demodulator, and the final fourth part goes to the 4-way phase splitter. The 4-way phase splitter provides a selectable (via rotary switches on the front panel) $0^\circ, 90^\circ, 180^\circ$, or 270° phase shifted output with respect to its input. The output of the 4-way phase splitter enters the single-side-band (SSB) mixer where it is mixed with a $160 - f$ MHz signal to produce the f MHz resonant frequency of our experiment. The $160 - f$ MHz signal is generated by an HP, model 8656B 0.1–990 MHz signal generator. It is also sent to the receiver. Finally, the rf pulses from the SSB mixer are passed to the transmitter/attenuator for final signal level adjustment before to be sent to the power amplifier. This completes the signal generating and transmitting portion of the spectrometer.

The receiving part of the spectrometer consists of a receiver and a demodulator. The receiver takes the signal from the preamplifier and mixes it with the $160 - f$ MHz from the HP signal generator to produce a 160 MHz intermediate frequency signal. This signal is further amplified and passed to

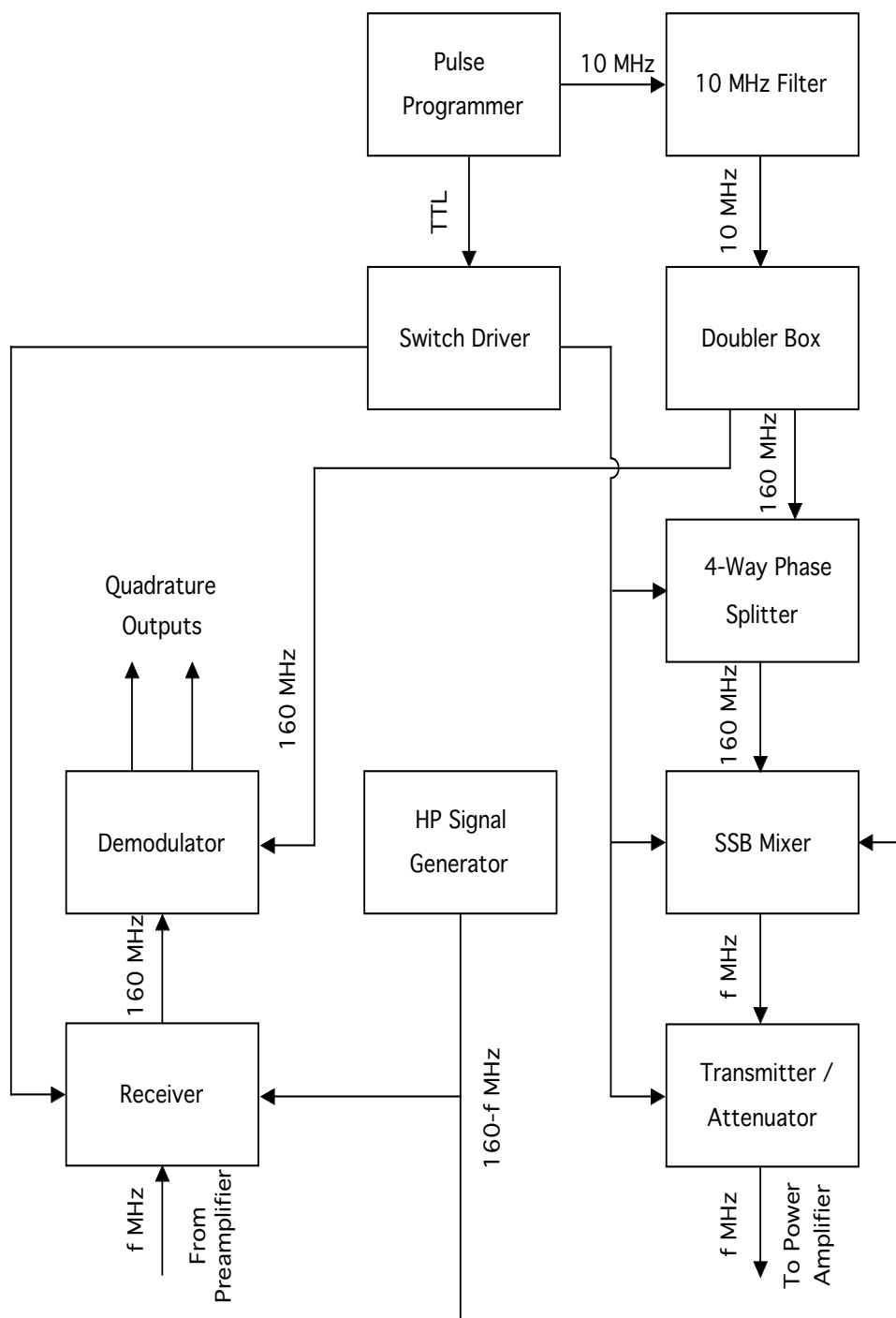


Figure 3.5: The 160 MHz intermediate frequency NMR spectrometer.

the demodulator. The demodulator mixes the 160 MHz signal from the receiver with the 160 MHz signal from the doubler box to obtain an audio frequency (around the resonance frequency) signal and thus produces the quadrature outputs collected by the Nicolet.

The parts of the pulse programmer—the main clock and the four channels—are contained in 5 separate boxes. The rest of the spectrometer circuitry is mounted into 3 chassis. The first chassis houses the doubler and the SSB mixer, the second chassis houses the switch driver board, the 4-way phase splitter and the transmitter, and the third chassis houses the receiver and the demodulator. The power for the spectrometer is provided by 2 Hyperion, model HY-ZI 32-5 power supplies—one for positive and one for negative voltages. The actual voltage levels supplied to the different electronic components are controlled by 3-terminal voltage regulators mounted inside the spectrometer chassis. LM317T regulators are used for the provision of the +15 V and +24 V positive voltages and a LM337T regulator is used for the provision of the -15 V negative voltage.

3.4.2 Signal Level Considerations and Modifications Made to the Original Spectrometer Configuration

Since its construction, a number of modifications to the spectrometer circuitry have been made during repairs of failed electronic components. Some of the poorly functioning amplifiers have been bypassed or replaced with new amplifiers of the same model, or better performing ones. At some places amplifiers were added to compensate for the lower signal levels, resulting from the continuous use of the electronics in the spectrometer. Some alternative paths in

the circuitry which were not actively used were also bypassed for the sake of simplifying the signal tracing process when making repairs. Below follows a description of the corrections to the spectrometer circuitry with comparisons to the description provided in [21], and a discussion of the characteristic signal levels at various points of interest.

Throughout this work we often will report the power levels in units of dBm. The conversion to the rms voltage is given by

$$\text{dBm} = 10 \log_{10} \left(\frac{V_{rms}^2}{50 \Omega \text{ mW}} \right). \quad (3.15)$$

Doubler

The 10 MHz sinusoidal signal at the output of the main clock has a level of 11 dBm. It is then sent through an attenuator currently set to 10 dB attenuation to the 10 MHz filter. The attenuator is located at the back of the spectrometer and is needed for adjustment of the level of the signal sent to the demodulator after being passed through the doubler box (Fig. 3.6).

The purpose of the doubler box is to generate the 160 MHz intermediate frequency signal from the 10 MHz signal produced by the main clock. The diagram of the doubler box presented here depicts the 4 doubling stages, each consisting of an Avnet (formerly known as Avantek) GPD-403 amplifier having 9 dB of gain, and a Mini-Circuits GK-2 frequency doubler having a 13 dB conversion loss. A Trilithic C3CH160/2-3-CC 160 MHz filter is used after the doublers to obtain a high quality intermediate frequency signal. Fig. 3.6 shows also the two GPD-403 amplifiers added after the filter which are not

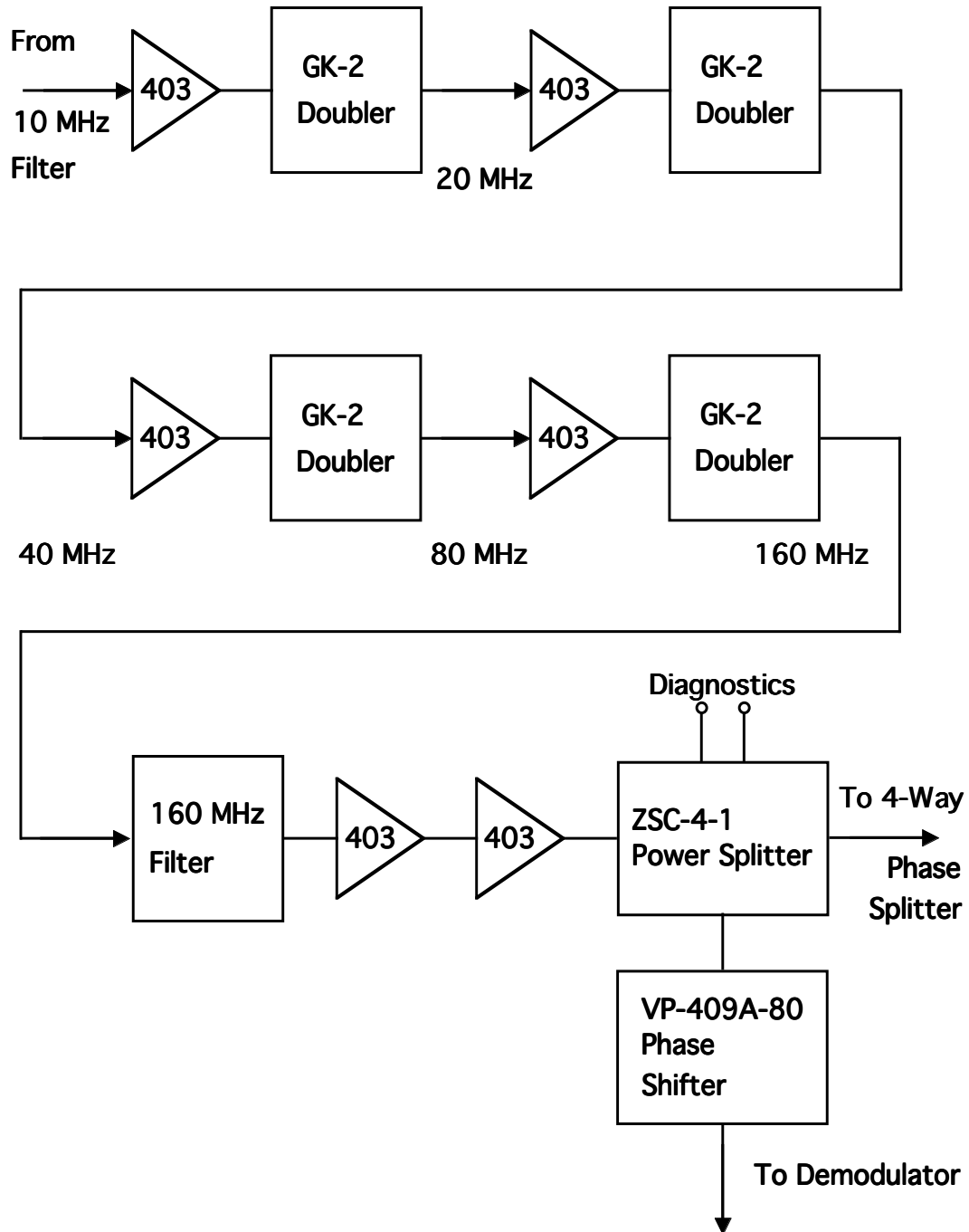


Figure 3.6: Schematic diagram of the frequency doubler.

shown on the equivalent schematic Fig. A.2 in [21] and are used for further amplification before splitting the signal to four portions by the Mini-Circuits ZSC-4-1 power splitter and sending two of them for diagnostics on the front panel of the spectrometer, the third one to the 4-way splitter, and the fourth one through a Lorch Microwave VP-409A-80 phase shifter to the demodulator.

4-Way Phase Splitter

After the doubler box the 160 MHz intermediate frequency passes through the 4-way phase splitter where the desired signal phase shift for each channel pulse is produced (only one channel at a time is active). A diagram of the 4-way phase splitter is provided in Fig. A.3 in [21].

SSB Mixer

After the phase shifter the signal is passed to the SSB mixer depicted in Fig. 3.7. The function of the single-side-band mixer is to mix the intermediate frequency signal with the $160 - f$ MHz signal from the HP in order to produce the operating rf frequency for the current experiment. In the SSB mixer the signal from the 4-way phase splitter first is split to two equal power level parts shifted by 90° with respect to each other by a Mini-Circuits ZCSCQ-2-180 power splitter. Another branch of the SSB mixer is the $160 - f$ MHz signal coming from the HP signal generator which passes through a Mini-Circuits ZFSWHA-1-20 rf switch and is then also split to two 90° out of phase parts by a broadband Anzac JH-10-4 power splitter. The four signals from the two branches are then mixed by two Mini-Circuits ZAD-1SH mixers and combined by a Mini-Circuits ZSC-2-1 power combiner in such a way that

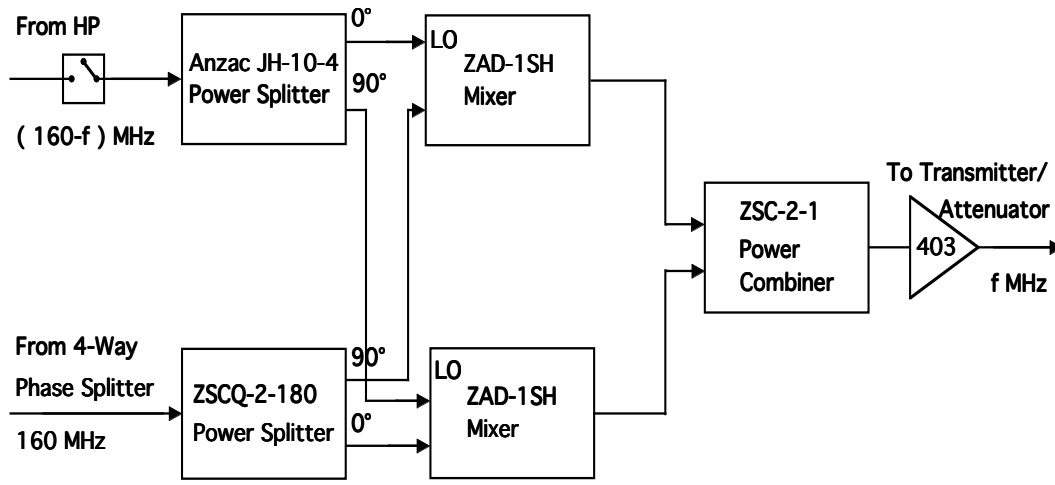


Figure 3.7: Schematic diagram of the single-side-band mixer.

only the frequency difference of the two branches is left, thus, producing the resonance frequency f . The Mini-Circuits ZSC-2-1 power splitter shown in Fig. A.4 in [21] is currently bypassed for additional signal gain to ensure that the Avnet UTL-1002 signal limiter used later in the transmitter (see Fig. 3.8) would saturate. Thus, the signal from the power combiner is sent directly to a GPD-403 amplifier and then to the transmitter/attenuator.

It is important that the ZAD-1SH mixers used in the single-side-band mixer have signals on their local oscillator inputs at a level between 13 and 17 dBm to ensure their proper functioning. This is why the HP signal generator output is kept at 8 dBm, then a GPD-405 amplifier with a gain of 13 dB is used to bring the power level to 21 dBm, and, finally, a Mini-Circuits ZCS-2-1 power splitter splits the signal to 2 equal parts each at a level of 18 dBm that go to the SSB mixer and to the receiver. Approximately 1 dB of loss is incurred in the rf switches, bringing the $160 - f$ signal level to the desired 17 dBm.

Transmitter

The transmitter/attenuator original design (Fig. A.5 in [21]) included two paths—a fixed, and a variable signal level path—separated and recombined by simple BNC tees. The latter path was achieved by incorporating an attenuator with a selectable level (4–42 dB) of attenuation. The variable path could be used, for instance, in an experiment when variation of H_1 is required. Only one path at a time was active, being selected by two Mini-Circuits ZFSHWHA-1-20 switches—one in each path. These switches were controlled by toggle switches on the front panel wired through the switch driver. Finally, a toggle switch after the recombination of the 2 paths was used to control the main on/off rf switch for transmitting pulses to the power amplifier and into the probe.

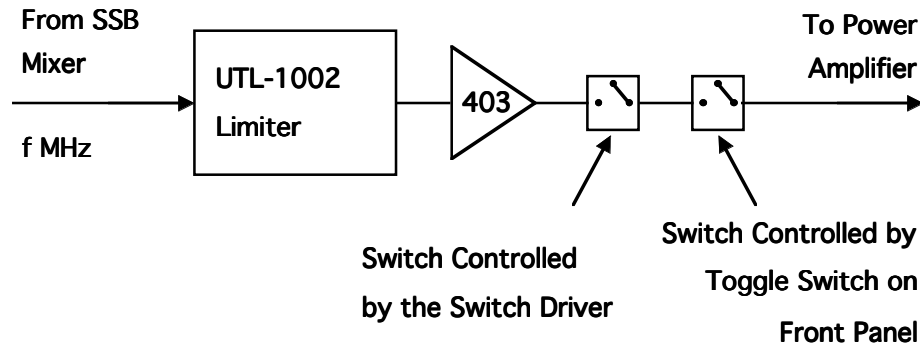


Figure 3.8: Schematic diagram of the transmitter.

It was decided for improvement of the signal strength to temporarily disconnect the variable path in the transmitter by removing the aforementioned BNC adaptors. The current single path configuration of the transmitter is depicted in Fig. 3.8. It starts with an Avnet UTL-1002 signal limiter whose output saturates at 0 dBm if a 0 dBm or higher signal level is passed to

its input. Thus, the limiter enables us to pump a signal with a constant level to the NMR probe, provided, that the SSB mixer's output is at least 0 dBm. After the UTL limiter the f MHz signal passes through a GPD-403 amplifier, through the 2 switches, and finally, leaves the spectrometer and is sent to the power amplifier.

However, the signal leaving the spectrometer now has a level of 10 dBm which is too high for our current set-up. The ENI power amplifier provides 50 dB of gain if a signal of level 0-10 dBm (signals higher than 10 dBm are not safe for the power amplifier) is sent to its input but saturates at 53 dBm (200 W). The semi-rigid coaxial cable included in the resonance tuning circuit cannot withstand such high power, though, and a breakdown occurs. The current power level sent to the probe is four times less than the maximum power and is achieved using a 13 dB attenuation of the transmitter output via an external attenuator. This situation clearly suggests the need of incorporating the variable path back into the transmitter circuitry.

Blanking Box

A blanking box located at the back of the spectrometer is used to turn off the power amplifier during receiving because of the high level noise it generates when operating. The blanking box utilizes a 74121 monostable multivibrator [23] with an RC constant of 12 ms. The blanking box uses a 5 V power supply and generates a pulse with duration equal to its RC constant when a falling edge is registered on its input. The input of the blanking box is controlled by a TTL signal from the last channel used in a given pulse sequence. The power amplifier then is turned off for 12 ms after receiving a TTL high from

the blanking box.

Receiver

The purpose of the receiver is to amplify significantly the weak NMR signal coming from the preamplifier while mixing it with the $160 - f$ MHz from the HP to obtain the 160 MHz intermediate frequency. The two ZFSWHA-1-20 switches controlled by the switch driver turn off the receiver during transmission. A Mini-Circuits ZAD-1SH mixer and a Trilithic C3CH160/2-3-CC 160 MHz filter are used for obtaining the intermediate frequency signal. In its original design (Fig. A.8 in [21]), the receiver also included an attenuator situated after the amplification stage which was to be used to prevent the amplifiers in the next module, i.e. the demodulator, from breaking into oscillations when a strong signal is received from the sample.

The high-gain (25 dB) Avnet GPD-202 amplifiers have been found to be very unstable. Both of the 202 amplifiers, used originally at the beginning and at the end of the receiver circuitry, ceased to operate properly. The one at the beginning of the receiver was replaced by an Avnet GPD-402 amplifier with a gain of 13 dB (Fig. 3.9). The GPD-202 at the end of the receiver is currently bypassed. The attenuator before the last 202 is also bypassed since no additional attenuation is currently needed by the experiments. On the contrary, the signal level at the end of the receiver has significantly decreased due to the loss of the high-gain amplifiers. In the future, the incorporation of more amplifiers should be considered to ease the data acquisition process.

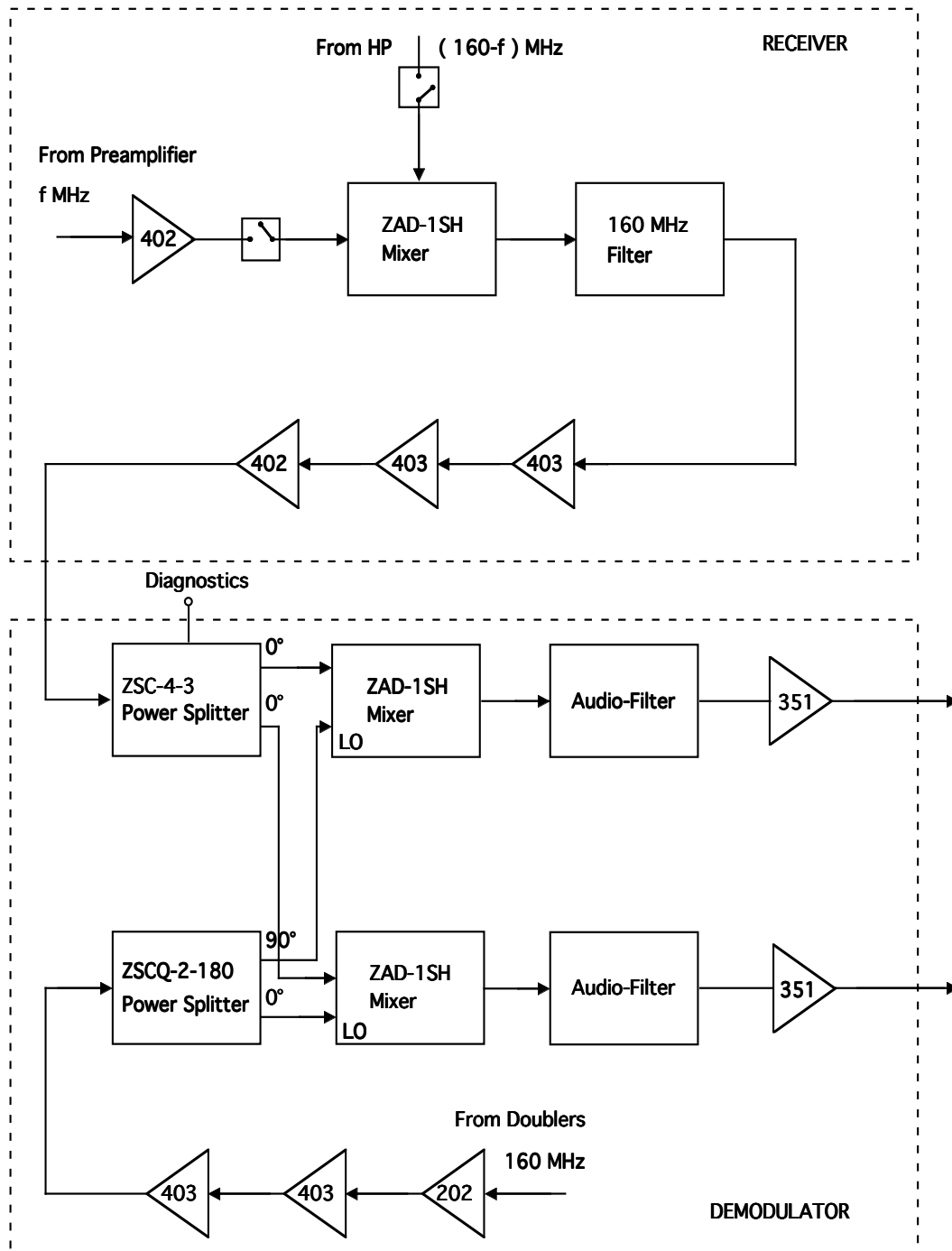


Figure 3.9: Schematic diagram of the receiver and the demodulator.

Demodulator

The purpose of the demodulator is to extract the NMR signal from the modulated carrier frequency of 160 MHz and to split the resulting audio frequency signal into its quadrature components which can then be sent to the Nicolet.

The phase-shifted intermediate-frequency signal from the doubler box is amplified by a set of a GPD-202 and two GPD-403 amplifiers so that its level is appropriate for the local oscillator (LO) inputs of the mixers positioned later in the circuit (Fig. 3.9). In the original design only one GPD-403 amplifier was used but later the second one was added to compensate for the decrease in gain of the GPD-202. The signal from the doubler box is split to two equal power, 90° out-of-phase parts by a Mini-Circuits ZSCQ-2-180 power splitter. These two parts then are applied to the local oscillator inputs of the above-mentioned Mini-Circuits ZAD-1SH mixers. The second input signal to the demodulator, the signal from the receiver, is directly sent to a Mini-Circuits ZSC-4-3 power splitter which splits it to three equal power level in-phase parts. One of them is sent to the front panel for diagnostics, and the other two are applied to the RF inputs of the ZAD-1SH mixers. The outputs of the mixers are connected to 2 Burr-Brown UAF42P audio filters which pass only the difference in frequencies coming from the mixers, thus producing the quadrature outputs carrying only the frequencies in a narrow band around the resonance frequency. The bandwidth of the passed audio signals is selected by rotary switches on the front panel of the spectrometer and it ranges from 1 kHz to the open bandwidth of 2 MHz. LF351 op-amps were originally used for buffering the final outputs but currently are used as well for additional power

amplification of 20 dB.

The strength of the noise N in the outputs of the audio filters is directly proportional to the square root of the bandwidth Δf :

$$N \propto \sqrt{\Delta f}. \quad (3.16)$$

Therefore, it is preferred to use a narrow bandwidth when possible. However, when the nucleus we are currently investigating in a particular compound has a broad line we opt to select a broader bandwidth of the filters in order to collect the signal from a broader portion of the NMR line, provided that H_1 is big enough to tip most of the spins from the line in the first place. Another feature to be considered is the ring-down time t_{RD} of the transients present in the receiver after each pulse sequence. It is inversely proportional to the selected bandwidth:

$$t_{RD} \propto \frac{1}{\sqrt{\Delta f}}, \quad (3.17)$$

for instance, a 10 kHz bandwidth results in a 100 μs ring-down time. Therefore, if we conduct an experiment with short relaxation times, of the order of tens of microseconds, it is imperative to select a wider bandwidth.

Switch Driver Card

Some modifications to the switch driver card were made in order to include a variable delay of the moment when the receiver switches close, i.e. the receiver turns on. These changes were made in an attempt to reduce the ringing observed after the end of the rf pulses if this ringing was partially caused by interference of the transmitter and receiver electronics.

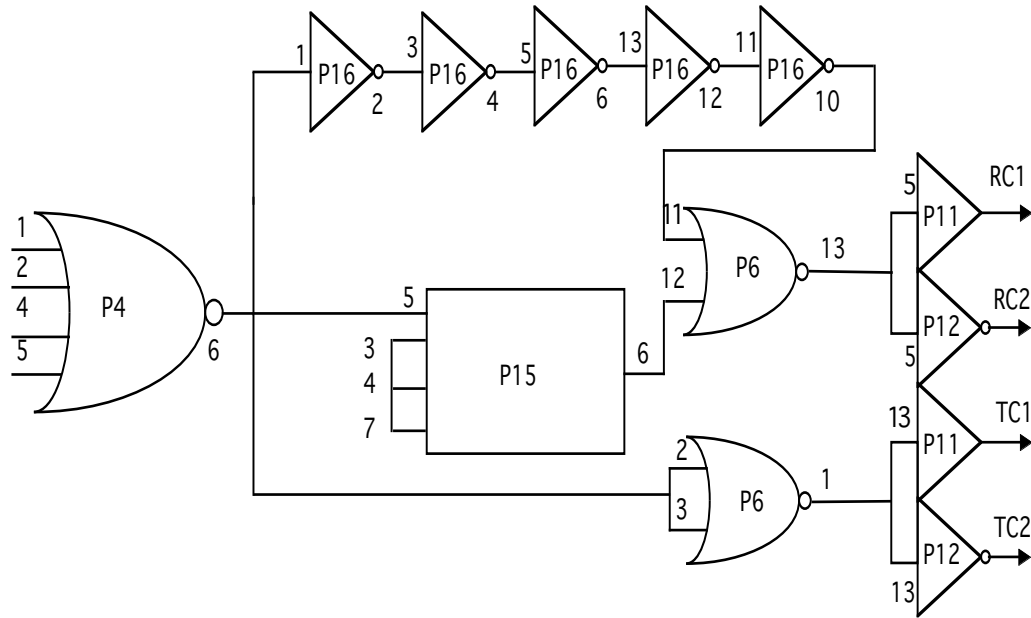


Figure 3.10: Modifications to the switch driver card made to obtain a selectable delay of the receiver turn-on time.

A thorough description of the operation of the switch driver is provided in [21]. Two chips were added to the switch driver card to implement the desired time delay. The new chips are a 74121 monostable multivibrator (P15) [23], and a 7404 hex inverter (P16) (see Fig. 3.10). The corrections only affect the path from the output of P4 to the receiver switches control signals RC1 and RC2. To obtain the variable delay a 1000 pF capacitor is connected between pins 10 and 11 of the multivibrator P15 and a $R_{var} + 1 \text{ k}\Omega$ resistance is connected between its pins 11 and 14, where R_{var} is a 0–50 k Ω variable resistor mounted on the front panel of the spectrometer. In addition, P16 is used 5 consecutive times introducing in such a way a slight delay in the path between the output of P4 and the pin 11 input of P6. This delay was introduced to prevent from glitches appearing in the output of P6 caused if both of its input

pins 11 and 12 are low for a short moment between the simultaneous transition to low of pin 11 and transition to high of pin 12.

3.4.3 Deuterium and ^{23}Na NMR as a Test of the Proper Functioning of the Spectrometer

After the major repairs made to the spectrometer circuitry, testing needed to be performed in order to determine the correctness of the operation of all electronic components. Each component was individually tested at 10 MHz. However, the most proper test for an NMR spectrometer is performing a real NMR experiment.

Deuterium (D) was chosen as a first test for its big signal, narrow resonance, and convenient relaxation times expected to be on a millisecond scale—not too short for avoiding the ringing problem mentioned above and discussed in details in the next section, but also not too long for avoiding a prolonged data acquisition.

The sample we used was a D_2O sample sealed in a glass ampule. A special coil for the deuterium experiment was made. The experiment was performed at a static field of 8.203 T, using a 10 kHz bandwidth of the audio filters in the demodulator. The resonance was discovered at the expected (no shifts, $\gamma_D/2\pi = 6.536$ MHz/T) frequency of 53.619 MHz. The duration of the $\pi/2$ pulse was determined to be $35\ \mu\text{s}$ which provided us with information about the strength of the induced alternating magnetic field in the NMR coil. According to Eq. (2.25) we estimated $H_1 \approx 11$ G. This experiment was conducted before the replacement of the series capacitor in the tuning circuit discussed in section 3.3 and therefore the power pumped into the coil was less

than the expected one.

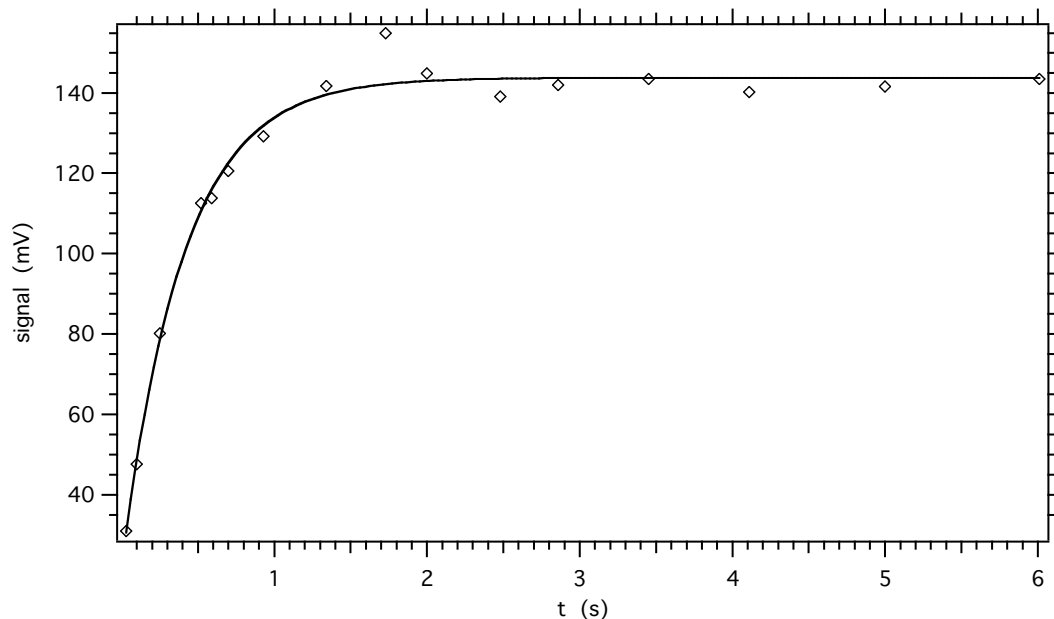


Figure 3.11: Room temperature T_1 measurement of deuterium as a test of the proper functioning of the spectrometer. Solid line is an exponential fit to the data.

Furthermore, room temperature measurements of T_2 and T_1 were conducted using respectively the standard $\pi/2 - \tau - \pi$ and the saturation recovery sequences described in Chapter 2. The results of the T_1 measurement are presented in Fig. 3.11. The data is in good agreement with an exponential recovery law of the magnetization. The point at $t = 1.73$ s was taken with a change in the phase which explains its offset from the exponential fit shown with the solid line. The T_2 measurement (Fig. 3.12) showed a little surprising results at short times. The tail of the decay fits very well to an exponential law (not shown on the figure) while the points taken at short times are better fitted with a gaussian line (solid line in the figure). The first point in the T_2 measurement, however, shows even a downturn, the origin of which is not

clear.

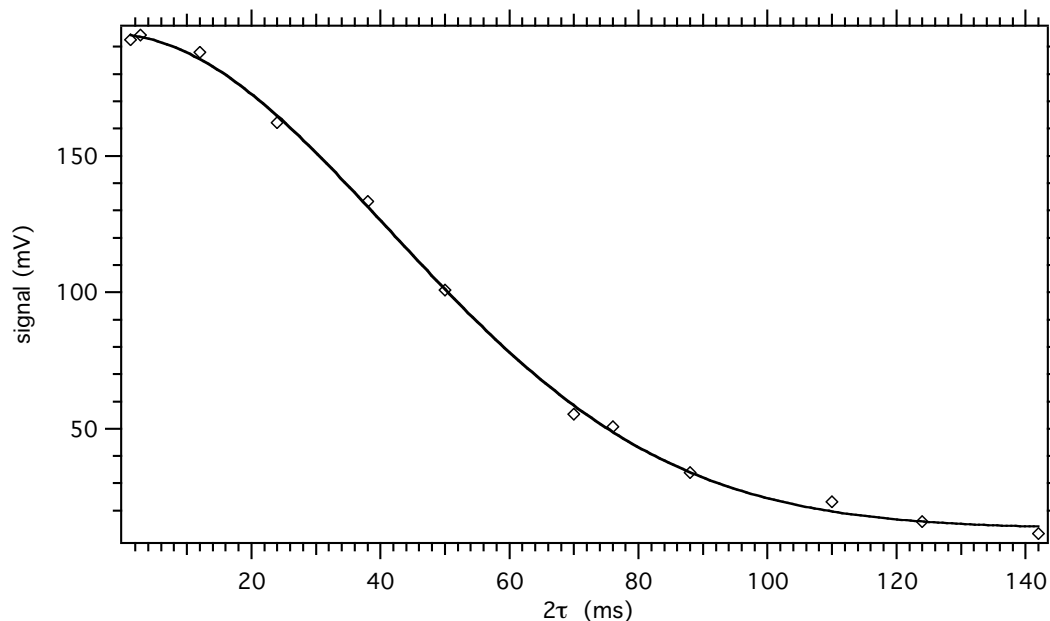


Figure 3.12: Room temperature T_2 measurement of deuterium as a test of the proper functioning of the spectrometer. Solid line is a gaussian fit to the data.

Still, there was a concern that the spectrometer electronic components might be operating differently at different frequencies. Since we were interested in performing an NMR experiment at frequencies in the vicinity of 92–93 MHz, where we would expect to find the ^{63}Cu resonance in $\text{YBa}_2\text{Cu}_3\text{O}_7$ for our static field of 8.203 T, we decided to test the spectrometer operation by searching for the ^{23}Na resonance in a water solution of common salt (NaCl) since ^{23}Na has a $\gamma/2\pi = 11.262$ MHz/T which is very close to the ^{63}Cu $\gamma/2\pi$ of 11.285 MHz/T. Similar to the deuterium experiment, it was again expected to have a narrow line with no significant shifts and a relatively strong signal. The sample was sealed in a 1/4" OD polyethylene tubing and the experiment was performed using the coil for the copper NMR. The resonance was found at an expected

frequency of 92.383 MHz. The duration of the $\pi/2$ pulse was determined to be $20\ \mu\text{s}$ which suggests we had similar to the deuterium $H_1 \approx 11\ \text{G}$. No further ^{23}Na measurements were made.

With the deuterium and ^{23}Na NMR experiments we tested the operation of the spectrometer circuitry and concluded that all components function properly and the spectrometer was ready to be used in our NMR investigations.

3.4.4 Reducing the Spectrometer Ringing

The ringing induced in the receiver after each transmit sequence could be due to internal transients in the electronics of the spectrometer, mechanical ringing of the coil after the high power pulses, or it could originate in a poorly operating electronics elsewhere in the circuitry.

In the previous section we already discussed the measures taken to reduce the ringing internal to the spectrometer. We also talked about how we try to reduce the ringing in the coil. This section is devoted to the discussion of the transient due to another part of the experimental set-up circuitry which turned out to be the most significant one in our experiment.

An example of the ringing we are concerned with is shown in Fig. 3.13. The ringing in the receiver lasts for more than $100\ \mu\text{s}$ and its strength is comparable to the huge deuterium test NMR signal. Clearly, it would fully cover any NMR signal of real experimental interest when the observation of an FID or an echo with a short τ is required.

For instance, the expected copper spin-relaxation time in $\text{YBa}_2\text{Cu}_3\text{O}_7$

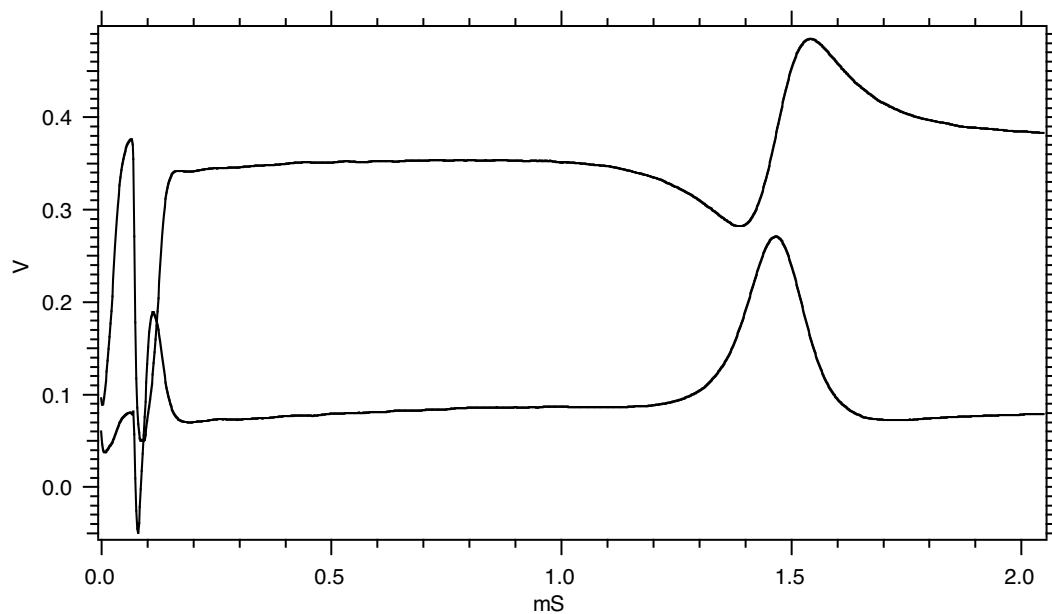


Figure 3.13: Signal-averaged quadrature outputs showing an NMR echo (deuterium) with the spectrometer ringing present in the beginning of both channels.

of less than $100 \mu\text{s}$ and the tiny strength of the signal would make it impossible to perform an NMR experiment on the afore-mentioned system. Therefore, it was imperative to solve the spectrometer ringing “mystery” before proceeding with the measurements in $\text{YBa}_2\text{Cu}_3\text{O}_7$.

The reason for the ringing turned out to be a transient at the power amplifier output which appeared after a blanking TTL signal was sent to the power amplifier logic input in order to turn it off during receiving.

The solid line in Fig. 3.14 (a) shows the ringing at the output of the power amplifier observed after the rising edge of a $70 \mu\text{s}$ long pulse was used to trigger the Nicolet. We see that the first spike is about 9 V high—a signal strong enough to pass through the crossed-diode boxes in the tank circuit and

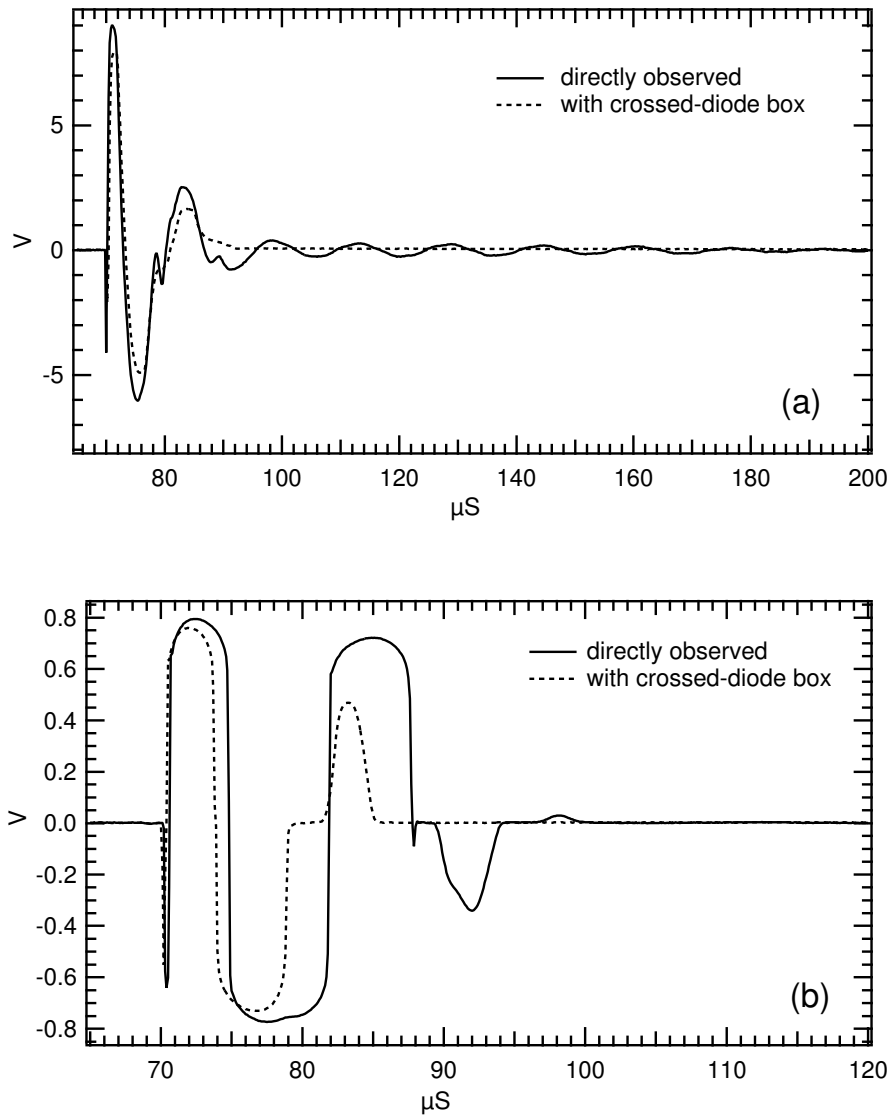


Figure 3.14: Ringing at the output of the power amplifier (a), and at the preamplifier input (b) observed directly and when attenuated with a crossed-diode box.

to be observed at the input of the preamplifier Fig. 3.14 (b).

Several different approaches for reducing the power amplifier ringing were attempted. The first trial for an attenuation of the transient was made by adding a box consisting of three crossed-diode stages each followed by $2\text{ k}\Omega$ resistors shorted to ground. The box was placed at the output of the power amplifier but did not give the expected result (the dashed lines in Fig. 3.14).

The next method we tried was a simple RC high-pass filter. Its cutoff frequency (the frequency at which the power of the transmitted signal drops in half) was selected to be 5 MHz which would provide us with the opportunity to use the same filter in all of our NMR experiments. The high-pass filter did a much better job at reducing the ringing. The result is presented in Fig. 3.15 (a). From the plot it can be seen that the filter attenuated the transient signal more than 10 times. However, tests showed that it also attenuated the power of the rf pulses by 3-4 dB (reduced it in half), an unwanted feature which led to a search of a better solution.

Finally, a tee was connected at the output of the power amplifier with one path going to the probe and the other connected to ground through a quarter-wavelength cable. The idea was borrowed from the use of the $\lambda/4$ cables in the tank circuit—the quarter-wavelength cable shorts all the frequencies except the resonant frequency for which the end of the $\lambda/4$ cable at the tee looks like an infinite impedance. Thus, the parasitic ringing is significantly reduced while the full power of the rf pulses is transferred into the probe.

The plot in Fig. 3.15 (a) shows that the quarter-wavelength cable does an even better job of ringing attenuation than the RC filter while preserving

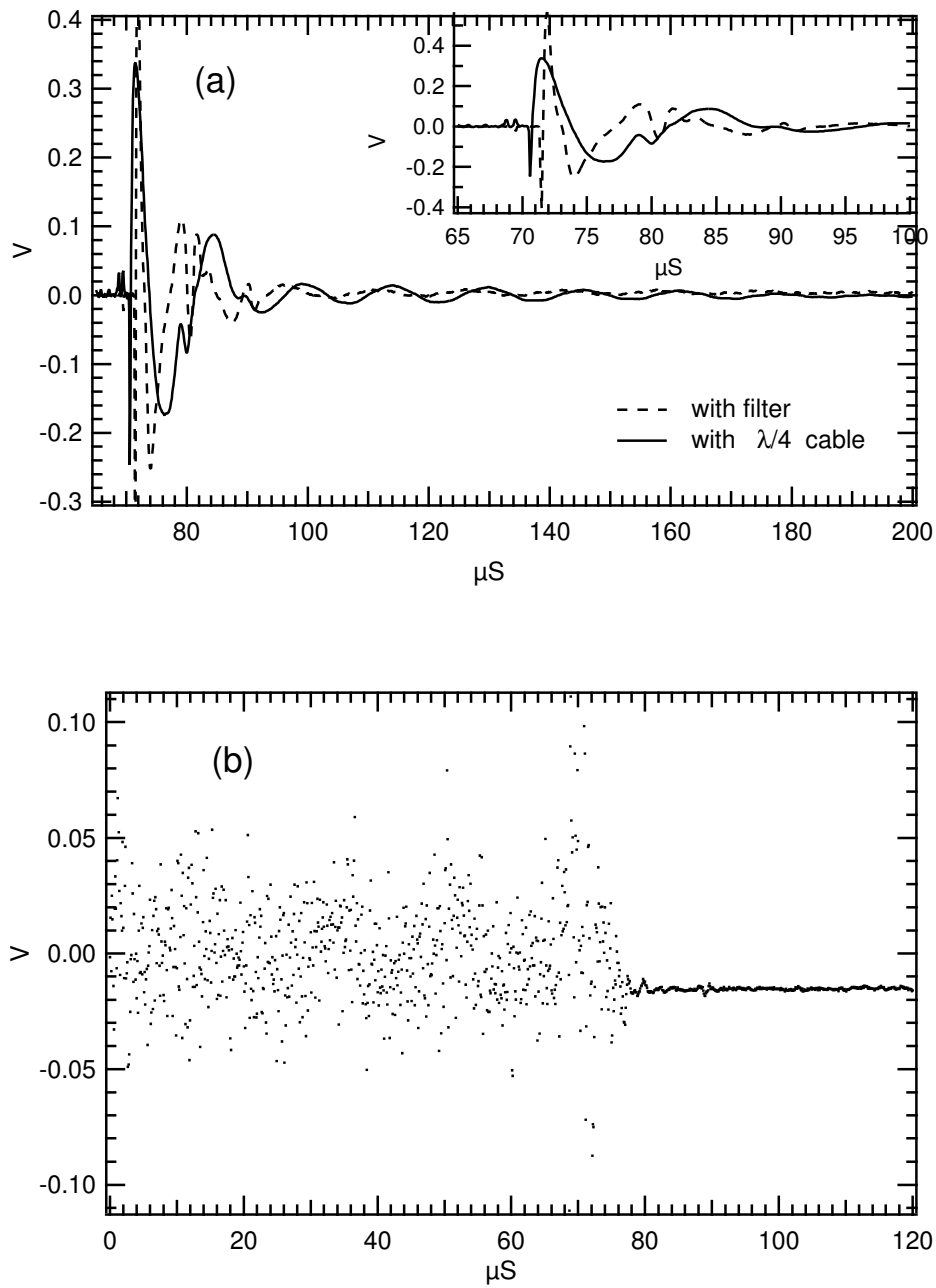


Figure 3.15: (a) Reduction of the ringing at the power amplifier output when using a high-pass RC filter or a $\lambda/4$ cable; (b) Output of the preamplifier when using a $\lambda/4$ cable as a method of ringing attenuation and triggering the Nicolet at the rising edge of a $70 \mu\text{s}$ pulse.

the strength of the rf pulses. Fig. 3.15 (b) is a plot of the signal observed on the output of the preamplifier when a $70\ \mu\text{s}$ pulse is sent to the probe. Evidently, the time that the ringing in the preamplifier lasts is about 10 times shorter than the ringing without attenuating the power amplifier transient. The new $8\text{--}10\ \mu\text{s}$ duration of the ringing gives us the opportunity to perform the copper NMR experiment in $\text{YBa}_2\text{Cu}_3\text{O}_7$ when using the full 2 MHz bandwidth of the audio filters which wouldn't add a significant ring-down time to the receiver ringing.

Chapter 4

Prelude to ^{63}Cu NMR in $\text{YBa}_2\text{Cu}_3\text{O}_7$

4.1 Overview and Motivation for Conducting the Experiment

The discovery in 1987 [24] of a high temperature superconductor composed of Y, Ba, Cu, and O with critical temperature $T_c \approx 90$ K above liquid nitrogen temperature has been followed by an enormous amount of work concentrated in crystallographic characterization of the $\text{YBa}_2\text{Cu}_3\text{O}_{7-\delta}$ (YBCO-123) phase and the discovered later by [25] $\text{YBa}_2\text{Cu}_4\text{O}_8$ (YBCO-124) phase with a critical temperature around 80 K. The results of this research are summarized in [26, 27], where thorough discussions of the crystal and micro-structure of these compounds are presented. We will restrict ourselves to mentioning that the 123 compound has either tetragonal ($a = b < c$) or orthorhombic (pseudotetragonal with a slightly longer than b) structure depending on the anneal conditions, e.g. the compounds with $\delta \approx 0$ possess the orthorhombic structure. There are two distinctive copper Cu1 and Cu2 sites present in 1:2 ratio in both structures of the 123 compound. The Cu2 sites are similarly situated in CuO_2 planes both in the tetragonal and the orthorhombic structures. The main difference between the two structures is in the existence of distinctive CuO chains in the orthorhombic structure, which is the structure of interest

for us since we are concentrating on studying the $\text{YBa}_2\text{Cu}_3\text{O}_7$ compound, i.e. the case of $\delta \approx 0$. The $\text{YBa}_2\text{Cu}_4\text{O}_8$ compound has also an orthorhombic structure with additional copper and oxygen atoms in it. The lattice parameters a and b in the 124 phase are similar to the ones of the unit cell in the 123 phase, but c is significantly longer in the 124 compound.

Along with the efforts to characterize the new system crystallographically, YBCO has drawn the attention of a large number of researchers who performed a variety of experiments in an attempt to set a consistent picture of the properties of the new material both in the normal and the superconducting states.

Since nuclear magnetic resonance was a very valuable tool in studying the classical superconductors, it was not a surprise that this technique was used by many scientists in their investigation of the properties of the novel high temperature superconductors, among which YBCO-123 has been by far the most extensively studied one with NMR performed on three of the four nuclei—Y, Cu, and O. Reviews of the results from these studies are presented in [28, 29].

In the normal state it was interesting to find the nature of the charge and the spin degrees of freedom. The major goal of the superconducting state studies was to understand the mechanism of the high temperature superconductivity itself.

In a metal, often the spin-lattice relaxation is governed by interactions with conduction electrons. In this case it can be calculated [2] that the spin-

lattice relaxation time is given by the formula

$$\frac{1}{T_1} = \frac{64}{9} \pi^3 \hbar^3 \gamma_e^2 \gamma^2 \langle |u_{\mathbf{k}}(0)|^2 \rangle_{E_F}^2 \rho^2(E_F) kT \quad (4.1)$$

where γ_e is the electronic gyromagnetic ratio, $u_{\mathbf{k}}(0)$ is the spatial part of the eigenfunction of the Hamiltonian describing the hyperfine nuclear-electron interaction evaluated at the nucleus and $\rho(E_F)$ is the density of states at the Fermi energy.

This formula can be expressed using the Knight shift K —a feature arising from the interaction of the nuclei with the conduction electrons and being defined as the ratio of the change in the magnetic field required to stay on resonance (with respect to the field in the absence of conduction electrons), to the magnetic field itself:

$$K = \frac{\Delta H}{H} \quad (4.2)$$

where

$$\omega = \gamma H = \gamma(H_0 + \Delta H). \quad (4.3)$$

Substituting the expression for the Knight shift [2]

$$\frac{\Delta H}{H} = \frac{4\pi}{3} \hbar^2 \gamma_e^2 \langle |u_{\mathbf{k}}(0)| \rangle_{E_F}^2 \rho(E_F) \quad (4.4)$$

into Eq. (4.1) we obtain the so called “Korringa relation”

$$\frac{1}{T_1} = \frac{4\pi}{\hbar} \left(\frac{\gamma}{\gamma_e} \right)^2 \left(\frac{\Delta H}{H} \right)^2 kT. \quad (4.5)$$

The Korringa law predicts a linear dependence of the relaxation rate with temperature for relaxations dominated by interactions with the conduction electrons.

Indeed, NMR measurements of ^{89}Y [30] and NQR (nuclear quadrupole resonance) measurements of the Cu1 sites of ^{63}Cu [31] in $\text{YBa}_2\text{Cu}_3\text{O}_{7-\delta}$ with δ close to zero showed in the normal state (up to about 300 K) a very close to linear dependence of the relaxation rate with temperature. However, the relaxation rate at the Cu2 sites [31] is relatively independent of temperature, and even exhibits a slight decrease at temperatures above 250 K. This behavior might be strongly related to the features causing the superconductivity since it is believed that the superconductivity occurs in the CuO_2 planes.

In the conventional superconductors with isotropic energy gap the relaxation rate increases forming a peak just below the critical temperature. This peak, known as the “coherence peak”, is due [32] to an enhancement of the density of states around the Fermi energy as a result of the opening of the gap. For temperatures well below the critical temperature the relaxation rate drops exponentially according to the standard BCS theory for s-orbital pairing

$$\frac{1}{T_1} \propto e^{-\Delta/T}, \quad (4.6)$$

where Δ is the energy gap.

In YBCO-123 however, the coherence peak was not observed in the measurements below T_c of ^{89}Y [30] and the Cu2 sites of ^{63}Cu [31]. Instead, a sharp falloff of the relaxation rate was found below T_c which could not be fit with the exponential decay in the classic BCS theory. In the extensive ^{63}Cu and ^{65}Cu NQR studies in [33, 34, 35] the absence of the coherence peak was confirmed one more time for both Cu1 and Cu2. This absence could be due to an anisotropic energy gap resulting from d-wave pairing. It was also shown

that the relaxation rate falloff below T_c is nonexponential for both Cu1 and Cu2 but it is much less steeper for the Cu1 sites than the Cu2 sites pointing again to the conclusion that the superconductivity primarily occurs in the CuO_2 planes. A power law dependence of the relaxation rate with temperature was found more suitable. In particular, for Cu2 the following fits were proposed: just below T_c $1/T_1 \propto T^6$, $1/T_1 \propto T^{4.5}$ for T in the region 40–80 K, and T^3 between 20 K and 40 K.

The high temperature superconductors are type II superconductors meaning that small regions with normal state cores, called “vortices” or “flux lines”, coexist with the superconducting state for applied fields between the upper and lower critical field, in which region the static magnetic field used in NMR usually falls. It is very interesting to explore the matter of how these flux lines are positioned inside a bulk superconductor and how they are moving due to thermal fluctuations. The thermal dynamics of the vortices has been studied by observing the ^{89}Y NMR linewidth narrowing in YBCO-123 [36] and in YBCO-124 [37], by T_2 measurements of ^{89}Y in YBCO-123 [38, 39], and by T_1 measurements of ^{89}Y in YBCO-124 [40]. All these measurement techniques provides us with information for the different motional regimes of the flux lines—the form of the vortices and the frequencies associated with their motion. For instance, T_1 measurements are sensitive to fluctuation in the xy -components of the local magnetic (caused by fluctuations of the vortices) with frequencies in the megahertz range. T_2 measurements are sensitive to fluctuation in the z component of the local magnetic field at ultraslow frequencies below 1 kHz.

Therefore, our intention was to perform $T_{1\rho}$ measurements in $\text{YBa}_2\text{Cu}_3\text{O}_7$ and $\text{YBa}_2\text{Cu}_4\text{O}_8$ in an attempt to explore the kilohertz frequency region between the regions studied via T_1 and T_2 measurements. Another advantage of studying $T_{1\rho}$ is that it provides information for fluctuations of both the xy and the z components of the local field which, in turn, give us information of how the vortices move—do they move as rigid “straws”, do they bend, or are they just 2D pancakes?

We chose to look for the copper resonance since its high gyromagnetic ratio (compared to yttrium, for instance) gives us a better relative intensity of the signal and S/N ratio. Also, the Cu NMR is attractive since high temperature superconductivity is almost always found in compounds containing CuO_2 planes. Since, the two copper isotopes ^{63}Cu and ^{65}Cu have natural abundances of 69% and 31% respectively, we selected the ^{63}Cu isotope for providing more signal. Thus, we proceeded with the preparation of the samples and with trials for performing the $T_{1\rho}$ measurement.

4.2 Sample Preparation and Attempted NMR Measurements

A $\text{YBa}_2\text{Cu}_3\text{O}_7$ polycrystalline compound was prepared via solid state reaction technique. 99.9999% pure starting ingredients of Y_2O_3 , BaCO_3 , and CuO were dried and mixed in the proper stoichiometric ratios using a mortar and a pestle. The obtained powder was fired in air at 900°C for 10 days being reground each day. After this, the powder was annealed in flowing oxygen atmosphere at 900°C for 5 min followed by a slow cool down to 400°C where the powder absorbed more oxygen for about 48 h and finally was slowly cooled

down to room temperature.

The additional anneal in oxygen atmosphere is necessary to remove the oxygen deficiency in the sample. When fired in air, the sample usually does not absorb enough oxygen to result in the compound $\text{YBa}_2\text{Cu}_3\text{O}_{7-\delta}$ with $\delta \approx 0$. The oxygen stoichiometry has been shown to have a great effect on the sample properties (first found by [41]). For instance, the compound with $\delta = 1$ is an antiferromagnet, $0.3 \leq \delta \leq 0.4$ is a superconductor with a transition temperature of 60 K, and $\delta \approx 0$ is the sample of interest—the superconductor with a transition temperature of 92 K.

X-ray characterization was done on the powder prepared in the way described above. The x-ray results showed a successful preparation of the desired sample with no additional or missing peaks, although the results were not 100% conclusive due to increased noise level in the x-ray apparatus.

An attempt to produce an $\text{YBa}_2\text{Cu}_4\text{O}_8$ was made using the described above solid state reaction technique. The final anneal for this sample is done in a high pressure oxygen environment. X-ray results showed that the first trial was unsuccessful and a second trial was not possible to make due to equipment problems.

When performing NMR on powder samples, one usually obtains a very broad resonance line. This is because the axes of the crystallites in the powder are randomly oriented with respect to the applied magnetic field and thus the resonance frequency is spread over a wide range. The line broadening results in decrease of the NMR signal since we are able to tip at the same moment only a small number (proportional to the strength of the rf field) of all the

spins in the sample. The decrease in the signal strength is often so significant that it can even become impossible to detect the resonance. Fortunately, a technique for orienting the crystallites has been developed [42] to help with this problem.

Hence, we proceeded with aligning our YBCO sample. The sample was mixed with epoxy Stycast 1266 in a 1:2 volume ratio, dense enough to allow for obtaining a strong signal, and at the same time not stacking the crystallites so close to each other that they affect each other's orientation. After this the mixture was placed in a specially-constructed for cylindrical (1/4" diameter, 3/4" length of the sample space) teflon mold which, in turn, was placed in the homogeneous field region of the NMR magnet for 24 h. The crystallites in the powder orient with their c axis along the field [43] and once the epoxy cures this orientation becomes permanent. Thus, the aligned sample provides a similar signal to the signal obtained from a single crystal sample, although since the alignment is never perfect the signal from a single crystal sample will still have a narrower line. Also, the dispersed powder sample permits a greater penetration of the rf field than a single crystal would.

Furthermore, a search for the ^{63}Cu resonance was performed in the 92–93 MHz, and more closely the 92.6–92.8 MHz frequency region, where according to the literature [35, 44, 45, 46] the resonance was expected to be found for our magnetic field of 8.20 T. In this search we used a silver coil (to avoid mixing the NMR signal from the sample with a possible signal from a standard copper coil), which was later also used in the ^{23}Na NMR testing of the spectrometer (see Chap. 3). We were using the full 2 MHz bandwidth of

the audio filters to be able to collect as much signal from the expected to be broad NMR line. We first looked for a free induction decay using a single $\pi/2$ pulse picked somewhat randomly to be $12 \mu\text{s}$ (until the actual resonance is found there is no method of determining the proper pulse length).

Since no signal was found in this first attempt it was decided to perform different characterizations on the epoxy embedded powder as a trial to check the quality of the crystallites' alignment. First, we performed a SQUID (Superconducting Quantum Interference Device) measurement of the magnetization of a piece of the sample with magnetic field both parallel and perpendicular to the c axis of the crystallites. The measurement was done using the “zero-field-cooled/field-cooled” sequence and the results are shown in Fig. 4.1. The temperature scale on both graphs is offset due to malfunctioning (fixed later) of one of the two thermometers used by the SQUID. Apart from the temperature offset however, the magnetic moment was not found to significantly differ from one orientation to the other. This might be pointing to the fact that alignment of the crystallites was not obtained for some reason. In addition, the total value of the magnetic moment seemed to be a little less than the expected one by an estimation. This, together with the not-so-sharp transition, might be a sign of existing mixture of several phases in the sample—some of which may be nonsuperconducting.

In addition to the SQUID measurement, an x-ray measurement was done on a plane parallel to the c axis of the embedded in epoxy sample. The expectation was to find only those peaks which were enhanced due to the alignment and not to find the suppressed ones. Figure 4.2 shows the result

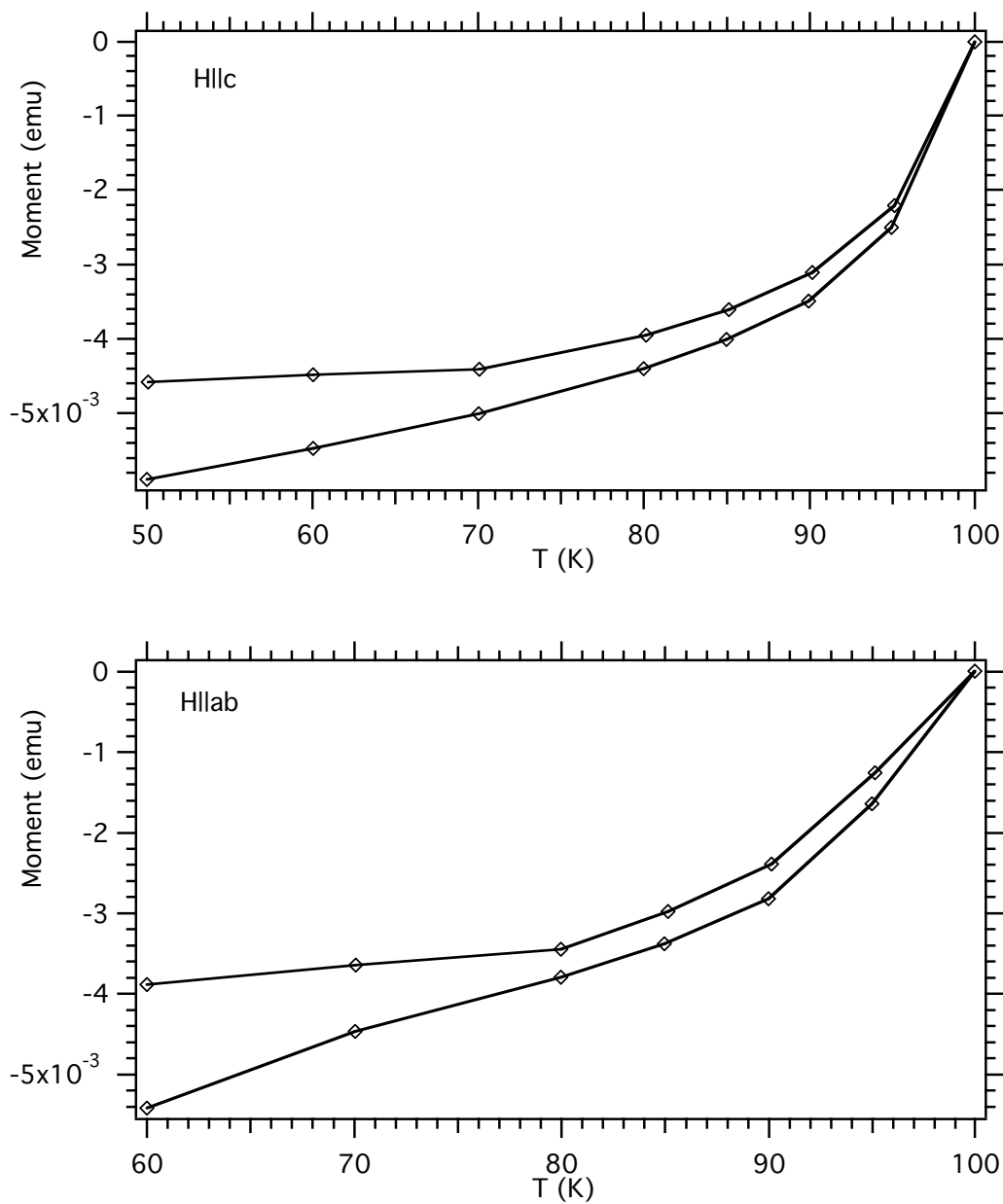


Figure 4.1: Magnetic moment measurement of the $\text{YBa}_2\text{Cu}_3\text{O}_7$ powder cured in epoxy with the field respectively parallel and perpendicular to the crystallites' c axis.

of the x-ray measurement of the powder embedded in epoxy compared to a typical unoriented powder sample. We see that there is no significant difference

between the two patterns which suggests that our sample was not oriented.

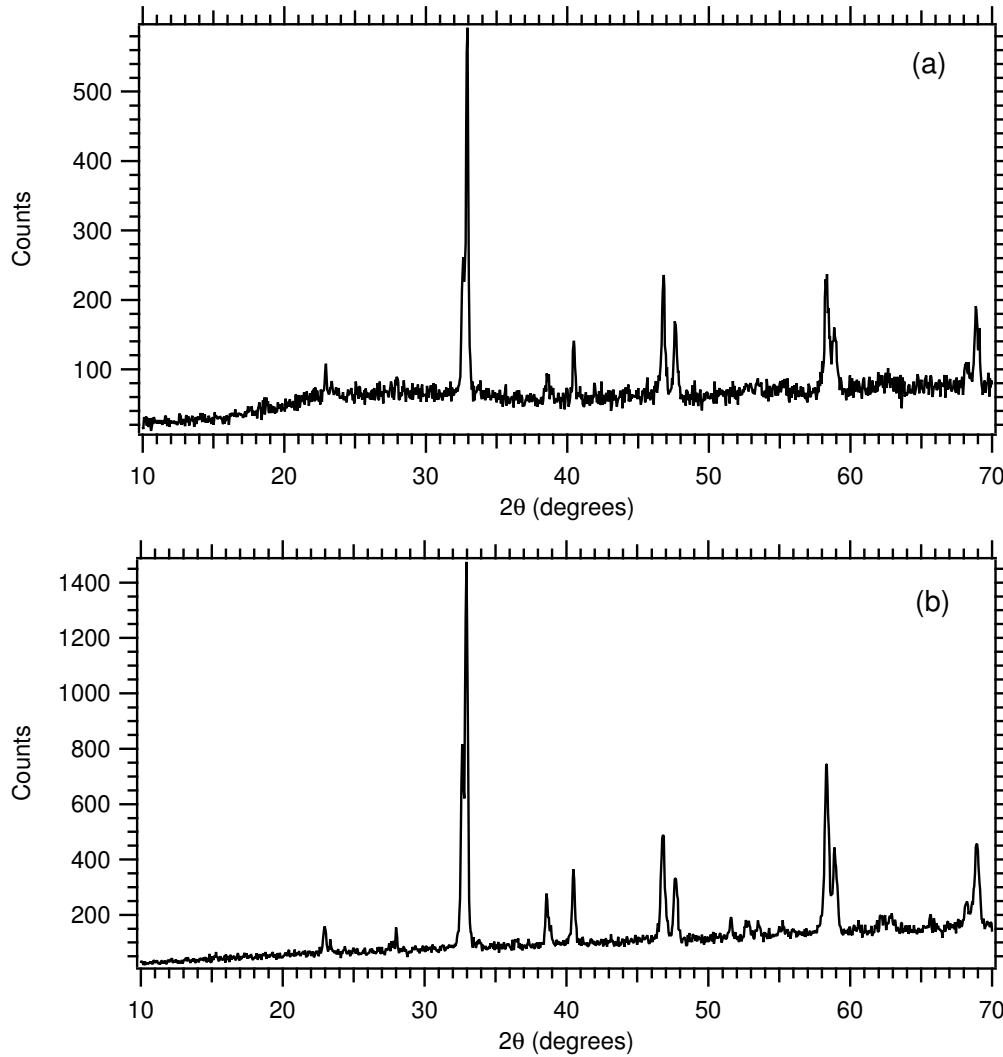


Figure 4.2: X-ray diffraction pattern of the YBCO sample embedded in epoxy (a) has the same peaks as a powder sample pattern (b). This points to the fact that orientation of the c axis of the crystallites was not achieved.

One reason for the unsuccessful orientation of the powder could be the existence of a small amount of magnetic impurities in it. For this reason more batches of sample were prepared in an attempt to produce a highly

homogeneous sample with as little impurities as possible. Another possible reason could be the size of the grains in the powder. If the grains are too big, they actually might be composed of several crystallites instead of a single one. Their c axes then would be randomly pointing in different directions making the alignment in the magnetic field impossible. To avoid such problems the powder in the next batch was passed through 45 μm size sieves before an attempt for alignment in the magnet was made.

Another attempt for finding the ^{63}Cu resonance was done after the changes made to the probe that allowed the use of the full power rf pulses (see Chap. 3). This time however, a search for an echo was chosen because of the expectation of a very short T_2 relaxation which would cause the signal in the FID to decay faster than the ringing after the pulses. Also, the length of the pulses used in the $\pi/2 - \tau - \pi$ sequence was chosen much closer to the ideal one since these pulses were well determined in the ^{23}Na NMR tests (Chap. 3) and a big difference was not expected because of the close gyromagnetic ratios of ^{63}Cu and ^{23}Na . Even with these improvements we were unsuccessful in finding the resonance.

More trials for aligning different batches of powder in the field were made by waiting different periods of time for the epoxy to harden a little before mixing the powder in. However, the x-ray measurements made on these samples one more time showed a probable random orientation of the grains.

In conclusion, we made numerous attempts to find the ^{63}Cu NMR resonance of aligned $\text{YBa}_2\text{Cu}_3\text{O}_7$ samples. The most probable reason for the lack

of success is the improper alignment of the samples. A suggestion for future work is to determine the exact oxygen concentration of the prepared samples, thus ensuring the purity of the superconducting phase and to pass the samples through smaller size sieves (5–10 μm) to ensure that several crystallites don't stack in one powder grain. Once it is determined that the alignment of the sample is successful another search for the ^{63}Cu NMR resonance should be made after determining the proper duration of the pulses at the current power configuration by using the ^{23}Na resonance as a test. In addition, when the high pressure oven is operating again, the trial for producing the YBCO-124 phase should be continued since the vortex fluctuation effects in this phase are stronger than in the 123 phase which may make the NMR experiments easier to perform.

Chapter 5

^{89}Y NMR in the $\text{Ca}_{2+x}\text{Y}_{2-x}\text{Cu}_5\text{O}_{10}$ Spin-Chain Compound

5.1 The $\text{Ca}_{2+x}\text{Y}_{2-x}\text{Cu}_5\text{O}_{10}$ System—Structure and Sample Preparation

Low-dimensional copper-oxide systems have received a lot of attention in relation to the discovery of high temperature superconductivity in cuprate compounds. The quasi-1D copper-oxide spin systems are expected to exhibit very interesting magnetic properties due to their low dimensionality and quantum fluctuations. In these compounds it is possible to observe 3D long-ranged order only when exchange interactions between the chains are present. Often, the quasi-1D compounds which can be doped possess a very complicated structure. Such an example is the $(\text{Sr}, \text{Ca})_{14}\text{Cu}_{24}\text{O}_{41}$ material which contains both CuO_2 chains and two-leg ladders [47, 48]. On the other hand, the spin-chain compounds with relatively simple structure often cannot be doped— CuGeO_3 , SrCuO_2 , Sr_2CuO_3 . Therefore, the $\text{Ca}_{2+x}\text{Y}_{2-x}\text{Cu}_5\text{O}_{10}$ material which can be hole doped and possesses a relatively simple structure is a very attractive system for studying the effects of introducing charge carriers into the copper-oxide chains.

The structure of the $\text{Ca}_{2+x}\text{Y}_{2-x}\text{Cu}_5\text{O}_{10}$ compound is thoroughly dis-

cussed in [49, 50]. It consists of edge-shared CuO_4 squares which form infinite CuO_2 chains. For $x=2$ the Ca ions occupy distorted octahedral sites between the chains, thus forming layers of the CuO_2 chains separated by layers of Ca chains. For smaller dopings ($0 \leq x < 2$) the Y atoms partially occupy the octahedral sites substituting for some of the Ca ions. There is no intervening oxygen neither between the different layers, nor between the CuO_2 chains within the same layer. The structure exhibits an incommensurate relation between the Ca(Y) chain repeat distance and the Cu chain repeat distance. The unit cell contains five CuO_4 squares along the chains parallel to the a axis, while four Ca(Y) atoms are repeated in the same distance. The b axis is selected perpendicular to the chain layers, while the c axis is perpendicular to the CuO_2 chains, but parallel to the layers formed by them.

When holes are introduced into the system the valence of the Cu ions changes from +2 to +2.4. The electrical conductivity of the material increases but still remains of insulating character through the whole doping range [51]. It is believed that the hole spins are delocalized over the four oxygens in the CuO_4 squares and couple with the copper spins to form Zhang-Rice singlets [52]. The holes are believed to frustrate the magnetic order in the chains. Recently, it was suggested by susceptibility and heat capacity measurements [53] that, while the undoped system exhibits a 3D long-ranged antiferromagnetic ordering, the system doped with holes transitions to 1D chain behavior and, finally, to cluster behavior at doping concentrations of $x \approx 2$.

Since nuclear magnetic resonance measurements of the spin relaxation times can provide us with information about the spin dynamics in a magnetic

material, we decided to perform ^{89}Y NMR measurements on the $\text{Ca}_{2+x}\text{Y}_{2-x}\text{Cu}_5\text{O}_{10}$ compound in an attempt to further investigate the properties of this relatively new system. For this purpose samples with different doping concentrations were prepared. We constrained our current study only to samples with $x = 0$ and $x = 0.5$, since the samples with higher dopings require preparation in high pressure oxygen atmosphere, which wasn't available to us at the moment.

The $x = 0$ sample was prepared via the solid state reaction technique described in Chap. 4 using the following starting materials: Y_2O_3 , CaCO_3 , and CuO . The mixture was fired in air at 1000°C for several days being re-ground every day. In order to fit more sample into the sample container, after being x-ray characterized the powder was pressed into $3/8''$ diameter pellets. The pressing was done by pouring the powder into a stainless-steel mold and applying 5000 psi pressure. The pellets obtained in such a way were fired for an additional 24 h in 1000°C and sealed in a glass ampule. The $x = 0.5$ sample was prepared by Elin Winkler in a similar fashion, except that all firings were done in O_2 atmosphere to ensure the proper oxygen absorption in the hole doped sample.

5.2 Results and Suggestions for Future Work

By studying the temperature evolution of the NMR relaxation times in a material one can extract information about the correlation times of the different nuclear and electronic spin subsystems interacting with the nucleus on which NMR is being performed. Thus, the ^{89}Y NMR measurements in the

$\text{Ca}_{2+x}\text{Y}_{2-x}\text{Cu}_5\text{O}_{10}$ material can reveal information about the timescale of spin flipping, and thus magnetic ordering, in the copper-oxide chains.

Here we report the ^{89}Y NMR lineshape and relaxation time measurements for two different doping concentrations ($x = 0$ and $x = 0.5$) at temperatures in the 250 K– 295 K region.

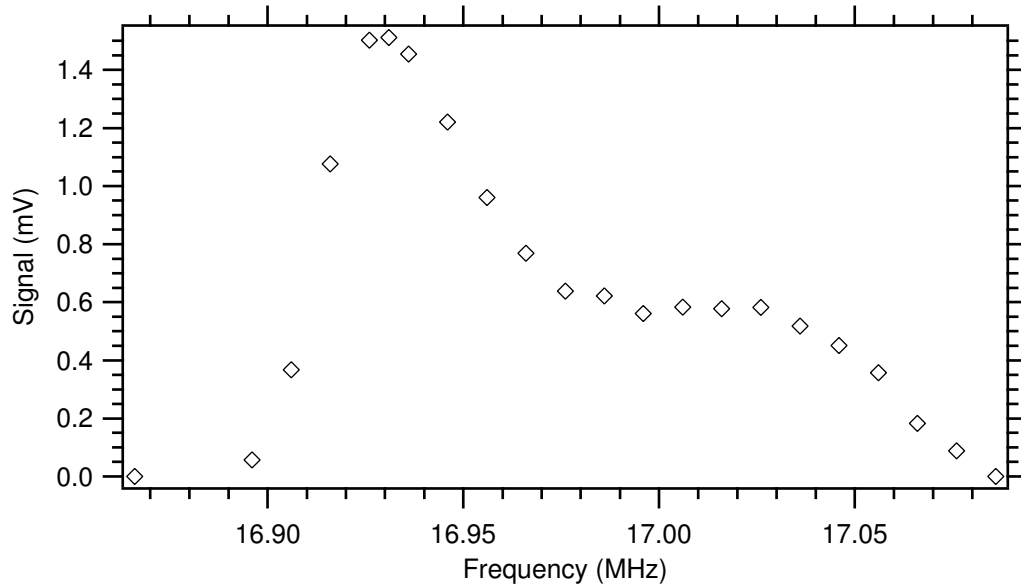


Figure 5.1: Shape of the ^{89}Y NMR line of the $\text{Ca}_{2.5}\text{Y}_{1.5}\text{Cu}_5\text{O}_{10}$ compound at 289 K.

We begin with the determination of the lineshape (Fig. 5.1) of the NMR signal for the hole doped compound ($x = 0.5$) at room temperature (289 K). From the graph we see that the line is quite broad with detectable signal over a frequency range of almost 200 kHz. In addition, the line is quite asymmetric. A possible explanation for the spreading in the resonance frequencies could be the random orientation of the crystal axes in the different grains of the powder. In general, the chemical shifts in a single crystal sample depend on its orientation with respect to the static magnetic field, having a different

resonance frequency along each axis. Since in a powder all angles of crystal axes orientation in the grains are randomly present we obtain a variety of resonance frequencies continuously spread over a relatively wide range. Such spectra are known as “powder patterns”. We refer the reader to the literature elsewhere for more information on this subject. Thorough calculations of the signal intensity as a function of frequency for particular set of resonance frequencies along the crystallographic axes of a sample are presented in [2].

Next, we discuss our spin-spin and spin-lattice relaxation times results. Fig. 5.2 shows the T_2 measurements at 275 K and 295 K temperatures in the compound with no hole doping ($x = 0$). Both graphs in the figure display the NMR echo strength as a function of 2τ . The lines represent exponential fits to the data. It can be seen that the signal decays faster in the lower temperature case resulting in a shorter relaxation time. T_2 is determined from the graphs and its value is presented in Table 5.1 together with all the relaxation times determined for the different temperature and doping cases.

The T_2 measurement for the hole doped compound ($x = 0.5$) is shown on the upper graph in Fig. 5.3. The lower graph in Fig. 5.3 shows that the natural logarithm of the measured signal as a function of 2τ can be fitted pretty well to a straight line as a visual proof of the exponential behavior of the spin-spin relaxation.

The spin-lattice relaxation time measurements at three different temperatures for the $x = 0$ material are presented in Fig. 5.4. The lines represent exponential fits to the data. Equipment instabilities resulted in higher deviations of the collected data from the fits at some temperatures compared to

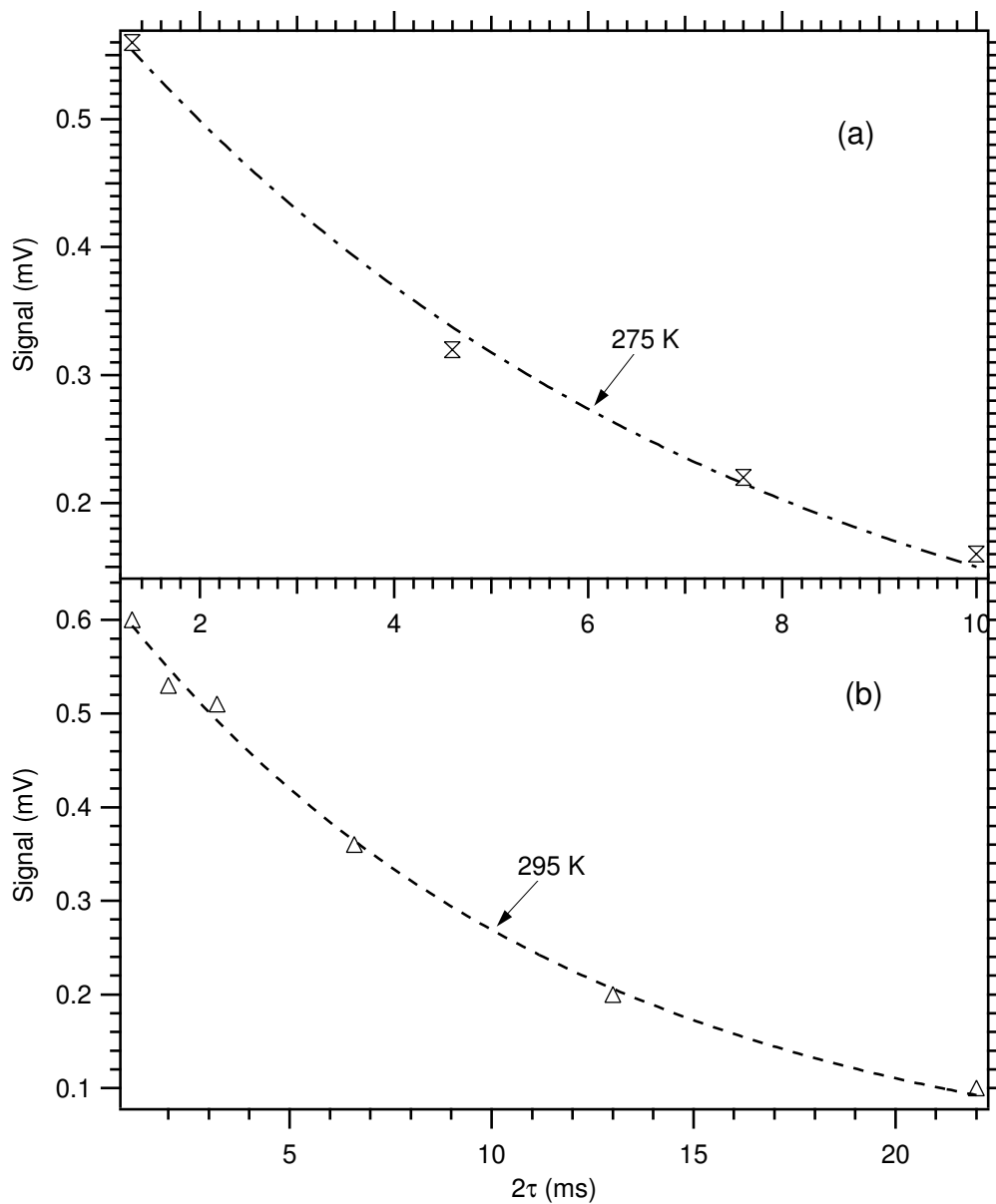


Figure 5.2: ^{89}Y T_2 measurements at 275 K (a) and room temperature (b) of the $\text{Ca}_2\text{Y}_2\text{Cu}_5\text{O}_{10}$ compound.

others. As the temperature was lowered various problems with tuning and temperature control appeared and finally prevented the data acquisition at lower temperatures, where the 3D ordering is actually expected to be observed. In

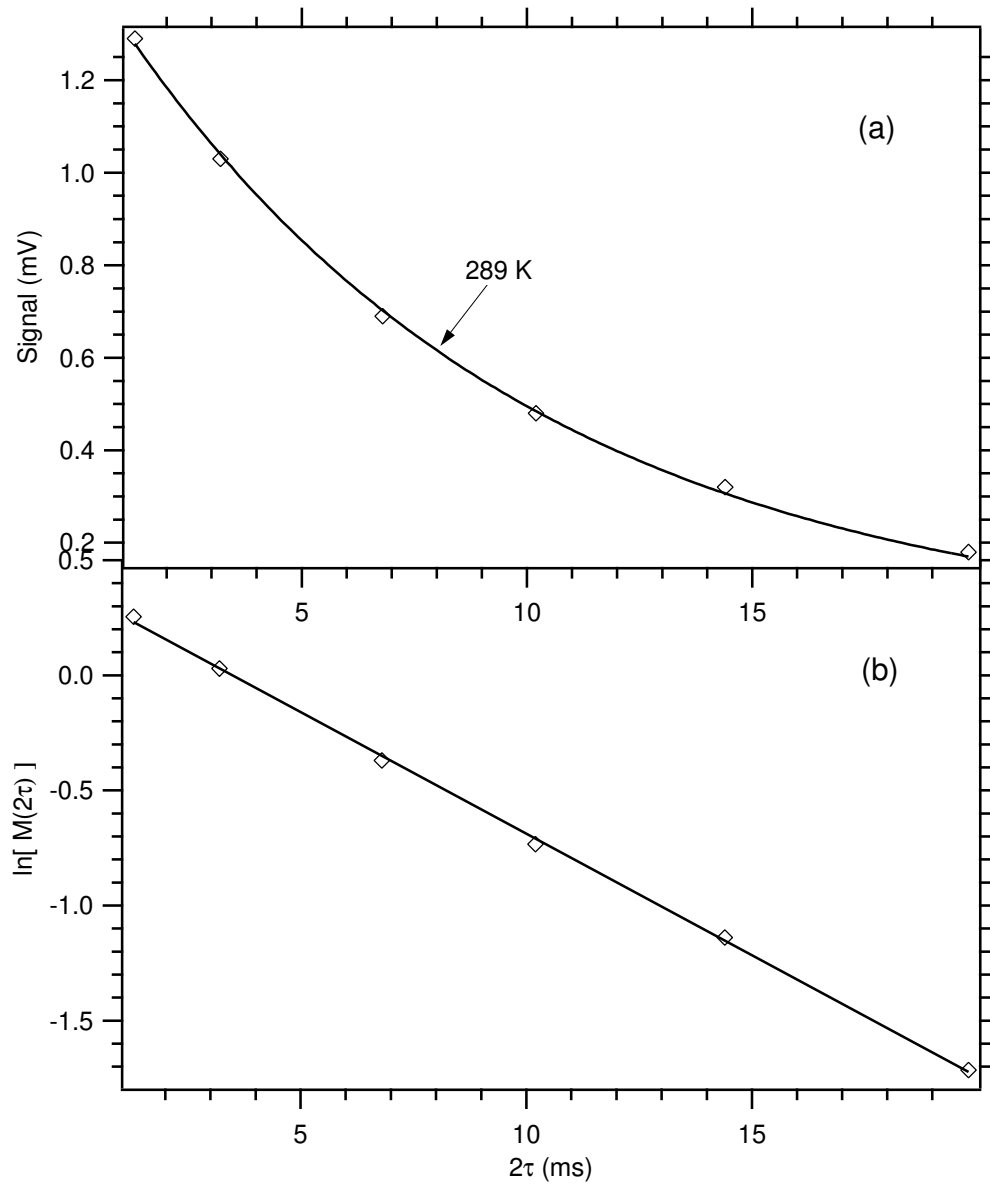


Figure 5.3: (a) ^{89}Y T_2 measurement of the $\text{Ca}_{2.5}\text{Y}_{1.5}\text{Cu}_5\text{O}_{10}$ compound at 289 K. (b) Straight-line fit of the logarithm of the signal as a function of 2τ .

fact, the 250 K T_1 measurement was conducted under strongly fluctuating conditions and should be considered somewhat unreliable.

Next, we present the T_1 measurement at 289 K of the hole doped com-

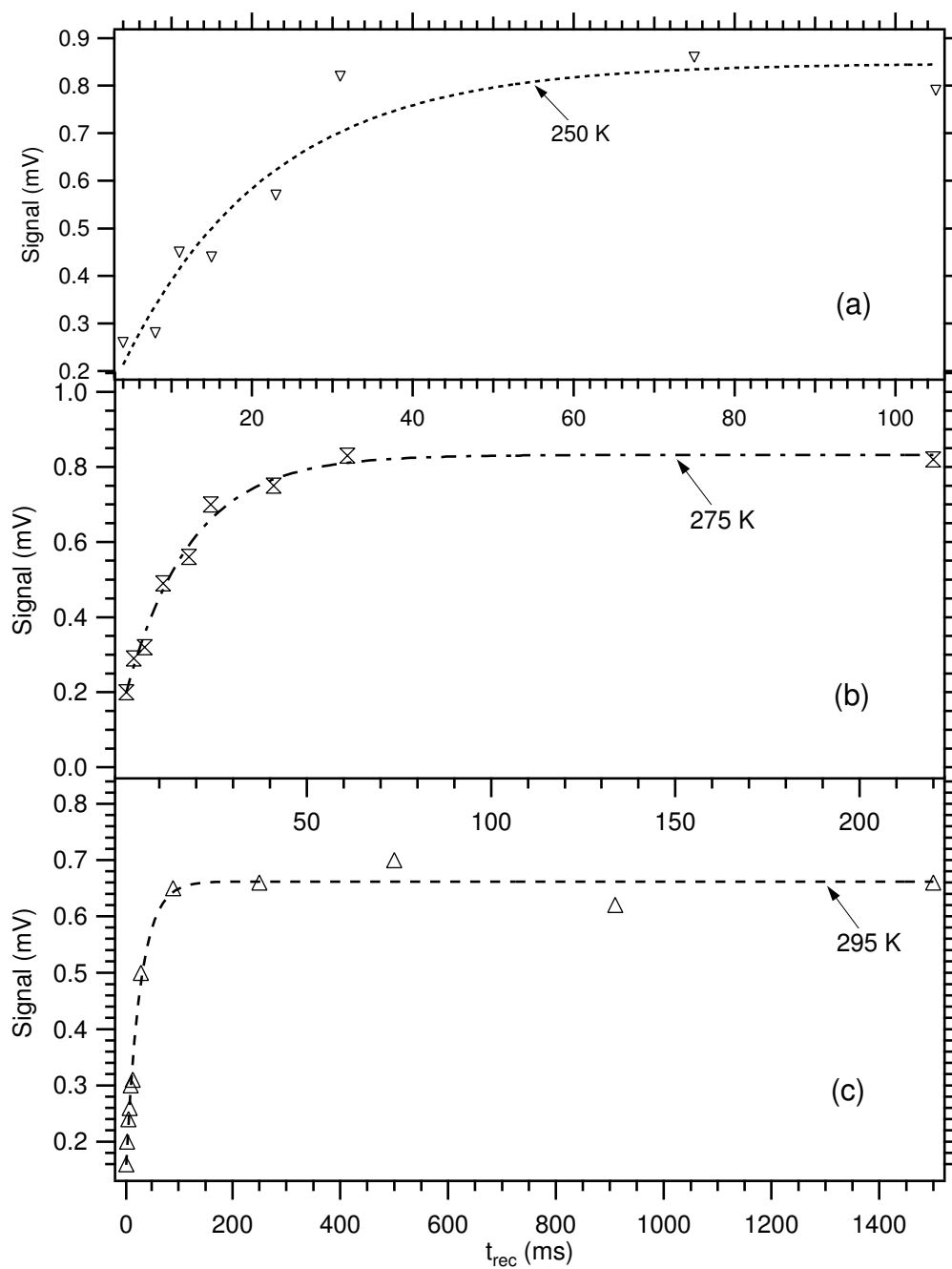


Figure 5.4: ^{89}Y T_1 measurements at 250 K (a), 275 K (b), and room temperature (c) of the $\text{Ca}_2\text{Y}_2\text{Cu}_5\text{O}_{10}$ compound.

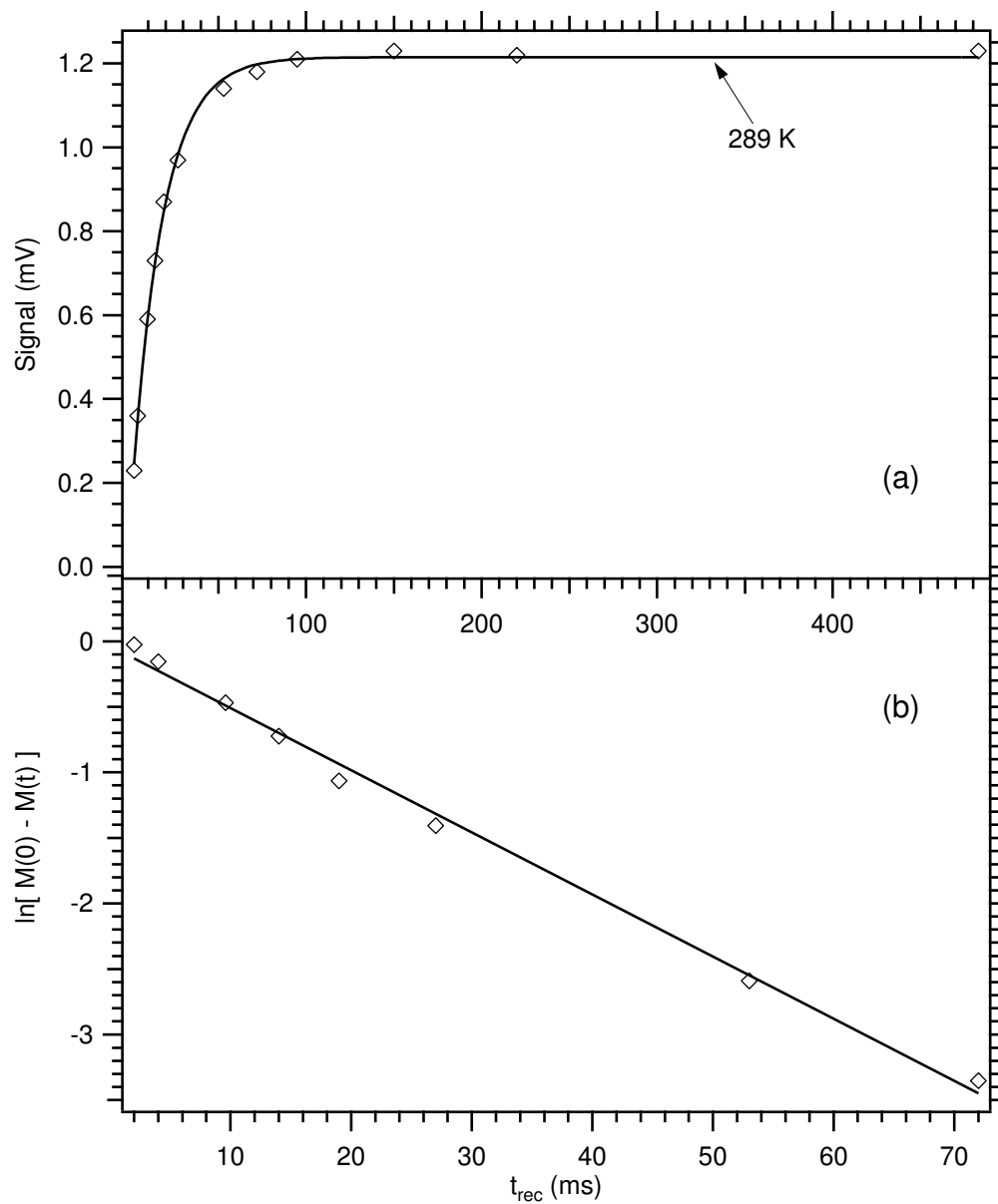


Figure 5.5: (a) ^{89}Y T_1 measurement of the $\text{Ca}_{2.5}\text{Y}_{1.5}\text{Cu}_5\text{O}_{10}$ compound at 289 K. (b) Straight-line fit of the logarithm of the difference between the equilibrium value and the current value of the signal as a function of recovery time.

pound ($x = 0.5$)(see Fig. 5.5). On the lower graph we plot the natural logarithm of the signal as a function of waiting time subtracted from the value of the signal at thermal equilibrium and we again observe a good fit to a straight line.

The spin-spin and the spin-lattice relaxation times are determined for all the conducted measurements. The results are summarized in Table 5.1 and are plotted on Fig. 5.6. We see that both types of relaxation times for the undoped compound decrease with temperature with the exception of T_1 at 250 K the obtained value of which, however, may not be completely trusted.

x	Temperature (K)	T_1 (ms)	T_2 (ms)
0	295	26.3 ± 3.1	11.2 ± 0.5
	275	17.6 ± 2.1	6.66 ± 0.38
	250	18.3 ± 5.7	
0.5	289	17.4 ± 0.6	9.17 ± 0.17

Table 5.1: ^{89}Y NMR T_1 and T_2 values for the $\text{Ca}_{2+x}\text{Y}_{2-x}\text{Cu}_5\text{O}_{10}$ compound.

To see why the decrease of the relaxation times with temperature is happening we proceed with describing the relaxation processes as a function of the correlation times of the different spin subsystems in the material. Since no free charge carriers are believed to be present in our compound we ascribe both the spin-spin and the spin-lattice relaxations to be due to magnetic dipolar moment interactions. Candidates to contribute to the Y spin relaxations are mainly the Y-Cu(nuclear) and the Y-Cu(electron) interactions since O and Ca have zero-spin isotopes with natural abundance above 99% and the Y-Y(nuclear) contribution is believed to be negligible.

The dipolar relaxation rates for unlike interacting spins are given by

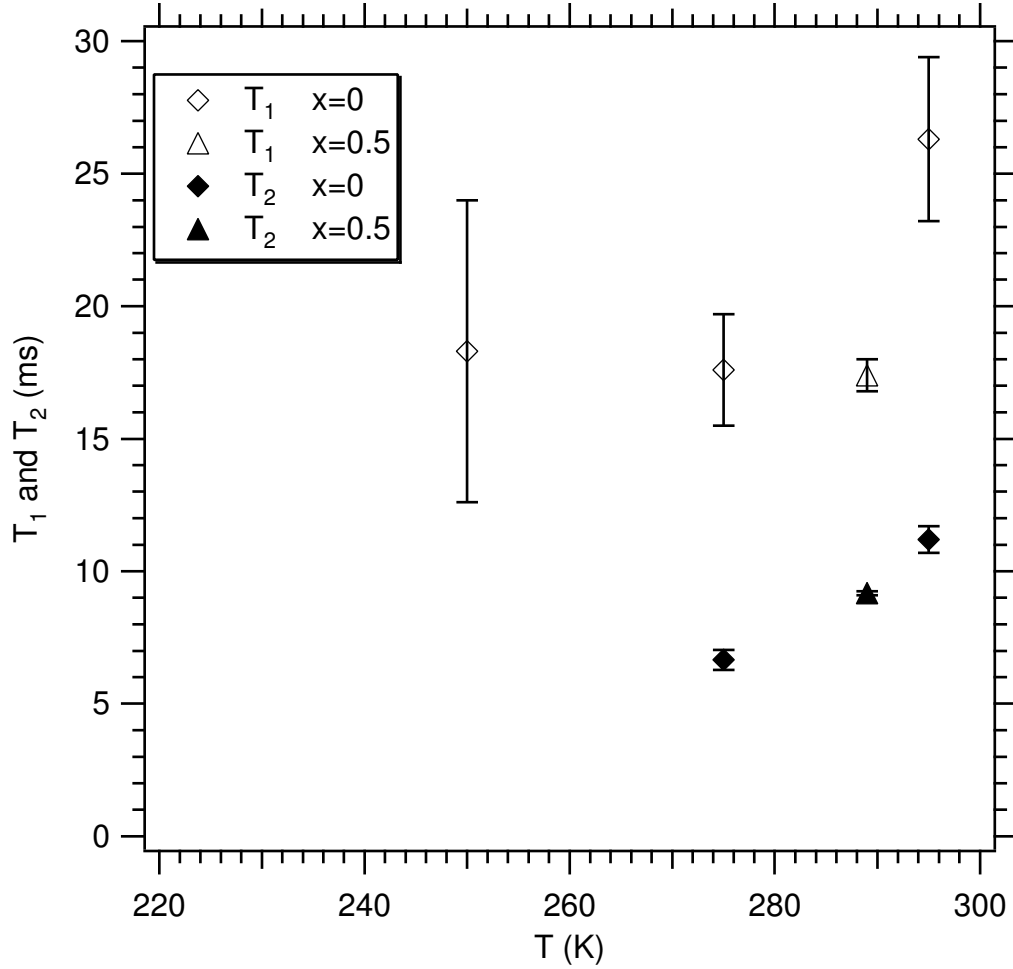


Figure 5.6: Summarized results of the ^{89}Y T_1 and T_2 measurements of the $\text{Ca}_{2+x}\text{Y}_{2-x}\text{Cu}_5\text{O}_{10}$ system at different temperatures for doping concentrations of $x = 0$ and $x = 0.5$.

the following expressions [17]:

$$\frac{1}{T_1} = M_{IS}^{2(I)} \left[\frac{1}{2}F(\omega_I - \omega_S) + \frac{3}{2}F(\omega_I) + 3F(\omega_I + \omega_S) \right] \quad (5.1)$$

$$\frac{1}{T_2} = M_{IS}^{2(I)} \left[F(0) + \frac{1}{4}F(\omega_I - \omega_S) + \frac{3}{4}F(\omega_I) + \frac{3}{2}F(\omega_S) + 3F(\omega_I + \omega_S) \right] \quad (5.2)$$

where $F(\omega) = \tau_c/(1 + \omega^2\tau_c^2)$ and $M_{IS}^{2(I)}$ is the dipolar second moment which

for a powder average is given by the formula

$$M_{IS}^2{}^{(I)} = \frac{4}{15} \gamma_I^2 \gamma_S^2 \hbar^2 S(S+1) \sum_i \frac{1}{r_i^6}. \quad (5.3)$$

In the above relations γ_I and ω_I are respectively the gyromagnetic ratio and the resonance frequency of the measured nucleus (related to each other via formula (2.7)), while γ_S and ω_S are the gyromagnetic ratio and the resonance frequency of the spin system interacting with the nucleus under consideration. Also, τ_c is the correlation time of the “S” spins, S is their spin number, and $\sum_i r_i^{-6}$ is the sum over all lattice sites of the distance between the interacting magnetic moments.

It can be seen that the sum on the right side of Eq. (5.1) has a maximum (corresponding to a minimum of T_1) as a function of τ_c while the sum on the right side of Eq. (5.2) continuously grows with τ_c (corresponding to a decreasing T_2 as a function of correlation time). The correlation time in general decreases from a finite low-temperature value with increasing temperature and therefore we should expect T_1 to have a minimum as a function of temperature, while T_2 should be constant at low temperatures and then increase with temperature. The fact that our measurements show increases in both T_1 and T_2 indicates that we are in the short correlation time regime.

Next, we proceed with evaluation of the correlation times of the Cu(nuclear) and the Cu(electron) spin subsystems. Because the electronic Cu magnetic moments are three orders of magnitude greater than the nuclear Cu magnetic moments we would expect them to have the major contribution to the Y relaxation rates. First, we solved numerically Eq. (5.1) using the 295 K value of T_1 for both the Y-Cu(nuclear) and the Y-Cu(electron) interaction

cases. For the Y-Cu(nuclear) case we used parameters averaged over the two copper isotopes (^{63}Cu , ^{65}Cu):

$$M_{\text{YCu}(n)}^2{}^{(\text{Y})} = 0.69 M_{\text{Y}^{63}\text{Cu}}^2{}^{(\text{Y})} + 0.31 M_{\text{Y}^{65}\text{Cu}}^2{}^{(\text{Y})} \quad (5.4)$$

$$\omega_{\text{Cu}(n)} = 0.69 \omega_{^{63}\text{Cu}} + 0.31 \omega_{^{65}\text{Cu}}. \quad (5.5)$$

The gyromagnetic ratios of ^{89}Y , ^{63}Cu , and ^{65}Cu were taken from a table, while their resonance frequencies were calculated for the current strength of our magnetic field $H_0 \approx 8.073$ T. The electronic gyromagnetic ratio and resonance frequency were calculated using Eq. (2.2). The sum over the lattice sites was calculated for 100 lattice constants using the following lattice parameters for the undoped compound [49]: $a = 14.09 \times 10^{-8}$ cm, $b = 6.18 \times 10^{-8}$ cm, and $c = 10.595 \times 10^{-8}$ cm. We obtained $\sum_i r_i^{-6} = 6.72 \times 10^{45}$ cm $^{-6}$.

Eq. (5.1) turned out not to have a solution for the correlation time of the Y-Cu(nuclear) interaction when solved using the experimentally measured value of T_1 which proved our initial suggestion that the Cu nuclei don't contribute to the Y spin-lattice relaxation. In fact, the calculation of the relaxation time T_1 due to the Y-Cu(nuclear) interaction gives a minimum value of 200 s, much larger than the observed T_1 . The solution of Eq. (5.1) for the Y-Cu(electron) interaction provided us with an estimate of the copper electronic correlation time at 295 K $\tau_c \approx 3.2 \times 10^{-11}$ s. By substituting this value in Eq. (5.2) we obtained an estimate of the electronic contribution to the spin-spin relaxation rate $1/T_2$. The calculated in such a way value of $T_2 \approx 23$ ms is very close to the measured spin-lattice relaxation time value of 26.3 ms, which confirms the correctness of our results since all the relaxation times are essentially equal in the high temperature limit, provided that they all are due

to the same kind of interactions. However, the measured value for T_2 of 11.2 ms suggests that an additional interaction, namely the Y-Cu(nuclear) interaction, does contribute significantly to the spin-spin relaxation in the studied compound. By plugging the difference in the measured and the calculated rate $1/T_2$ in Eq. (5.2) we obtained an estimate for the correlation time of the copper nuclear spin system at 295 K $\tau_c \approx 70 \mu\text{s}$. This correlation time should be of the order of the copper NMR spin-spin relaxation time in this material.

Similarly, we obtained the following correlation times for the undoped compound at a temperature $T = 275$ K: for the Cu(electron) spin subsystem $\tau_c \approx 4.8 \times 10^{-11}$ s, for the Cu(nuclear) spin subsystem $\tau_c \approx 120 \mu\text{s}$.

Finally, since the lattice parameters of the $\text{Ca}_{2+x}\text{Y}_{2-x}\text{Cu}_5\text{O}_{10}$ compound vary within one percent with doping concentration and since by decreasing the Y doping we actually dilute the system resulting in a smaller sum $\sum_i r_i^{-6}$, one would expect to obtain smaller relaxation rates (at the same temperature) than for the undoped compound. This effect should be even stronger since we expect that the disorder in the copper-electron spin system increases with doping resulting in a shorter relaxation rates. However, the measured value of T_1 for the $x = 0.5$ compound is actually smaller than the one we would expect to have at the same temperature for $x = 0.5$ (see Fig. 5.6). In addition, the difference in T_1 and T_2 is smaller for $x = 0.5$. All these features need to be considered more closely in a future attempt for more accurate modelling of the interaction picture in the copper-oxide chains.

In conclusion, we performed ^{89}Y NMR measurements of the lineshape and the relaxation times T_1 and T_2 in the $\text{Ca}_{2+x}\text{Y}_{2-x}\text{Cu}_5\text{O}_{10}$ spin-chain com-

pound for two different doping concentrations and for temperatures between 250 K and room temperature. The lineshape showed a standard powder pattern broadening. Both relaxation times were determined to have an exponential behavior and decreased with lowering the temperature which led us to conclude that we were operating in the short correlation time regime. The measured values of T_1 and T_2 were used to calculate the correlation times of the nuclear and the electronic copper spin subsystems, which were considered to be the major contributors to the Y spin-relaxation processes. The estimated correlation times showed that the spins in the copper chains of the undoped compound already slow down at temperatures significantly higher than the antiferromagnetic transition temperature of 29 K [53].

In the future, the study of this very interesting compound should be continued. Measurements at lower temperatures should reveal the temperature dependence of the spin correlations in the copper-oxide chains, thus providing information about the magnetic-ordering transitions. Samples from the full range of dopings should be prepared after the high pressure oven is repaired and they should be thoroughly studied to obtain a more complete picture of the spin behavior in the chains as a function of hole doping.

Appendix A

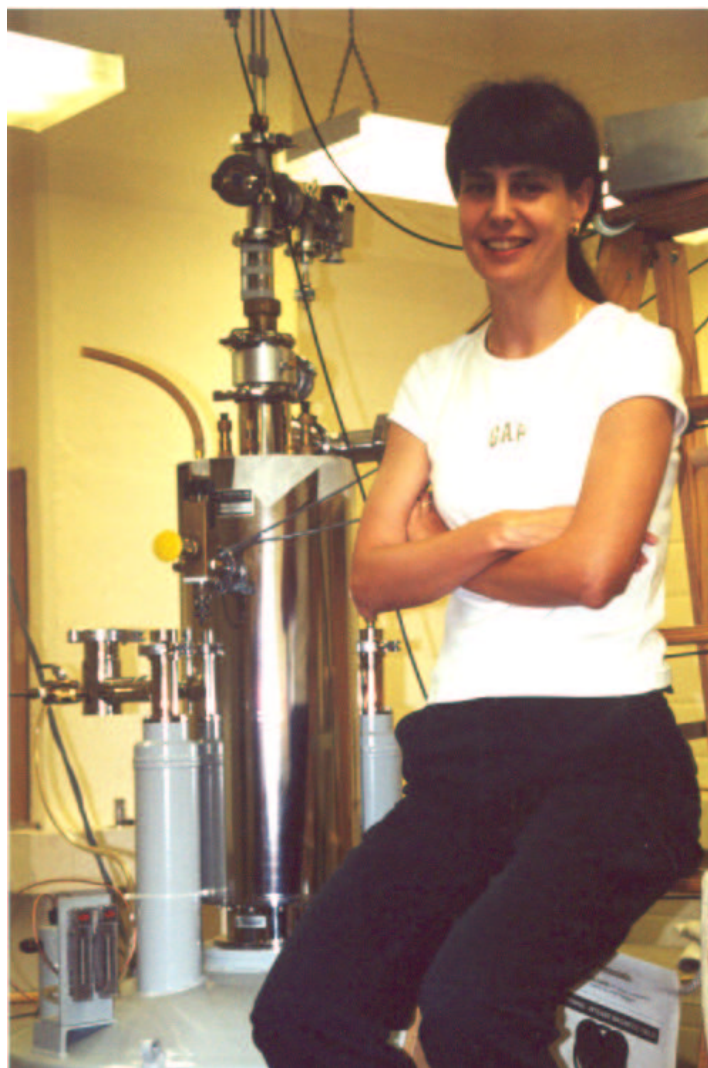


Figure A.1: The author, the NMR probe, and the superconducting magnet.

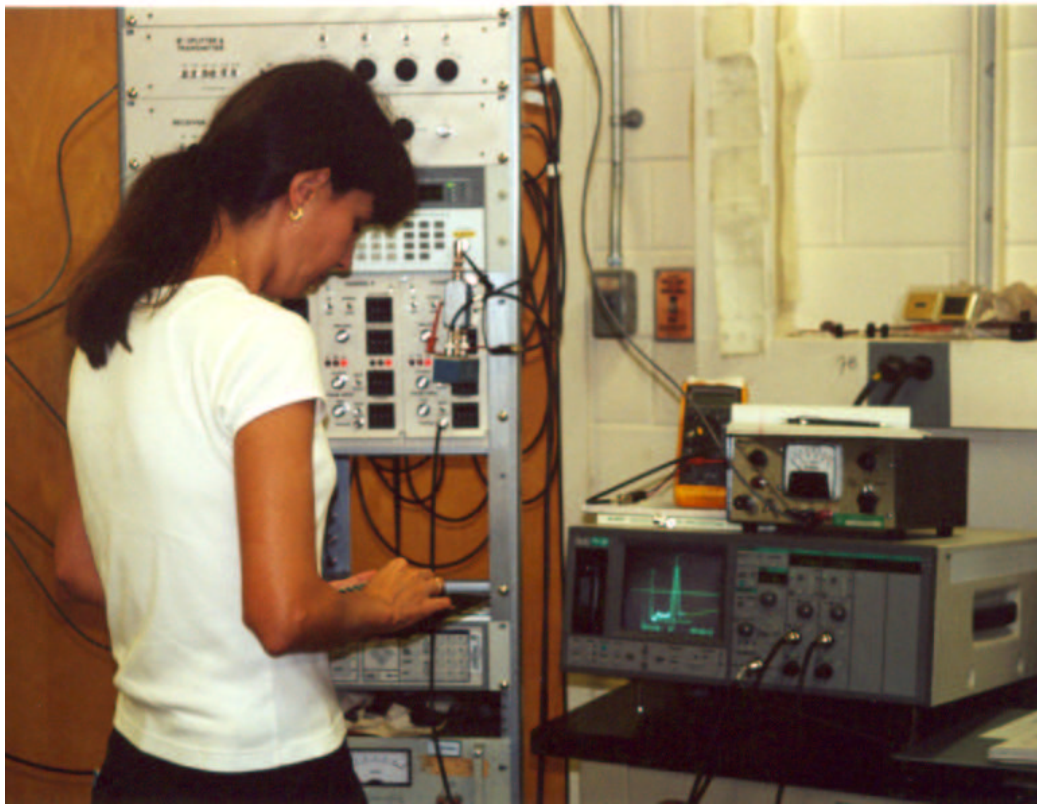


Figure A.2: Collecting data from the $\text{Ca}_{2+x}\text{Y}_{2-x}\text{Cu}_5\text{O}_{10}$ material.

Bibliography

- [1] J. G. Bednorz and K. A. Müller, *Z. Phys. B* **64**, 189 (1986).
- [2] C. P. Slichter, *Principles of Magnetic Resonance* (Third Edition, Springer-Verlag, Berlin, 1996).
- [3] E. Fukushima, *Experimental Pulse NMR. A Nuts and Bolts Approach* (Addison-Wesley, Reading, 1994).
- [4] D. Canet, *Nuclear Magnetic Resonance. Concepts and Methods* (John Wiley & Sons, New York, 1996).
- [5] J. J. Sakurai, *Modern Quantum Mechanics* (Addison-Wesley, Reading, 1994).
- [6] N. W. Ashcroft and N. D. Mermin, *Solid State Physics* (Saunders College Publishing, Harcourt Brace College Publishers, Orlando, 1976).
- [7] A. Abragam, *The Principles of Nuclear Magnetism* (Oxford University Press, London, 1961).
- [8] E. L. Hahn, *Phys. Rev.* **80**, 580 (1950).
- [9] E. D. Becker, J. A. Ferretti, and T. C. Farrar, *J. Am. Chem. Soc.* **91**, 7784 (1969).

- [10] H. Y. Carr and E. M. Purcell, *Phys. Rev.* **94**, 630 (1954).
- [11] S. Meiboom and D. Gill, *Rev. Sci. Instrum.* **29**, 688 (1958).
- [12] D. C. Ailion, “NMR and Ultraslow Motions” in *Advances in Magnetic Resonance*, Vol. 5, edited by J. S. Waugh (Academic Press, New York, 1971).
- [13] W. G. Clarck and J. A. McNeil, *Rev. Sci. Instrum.* **44**, 844 (1973).
- [14] T. C. Farrar and E. D. Becker, *Pulse and Fourier Transform NMR* (Academic Press, New York, 1971).
- [15] T. J. Gramila, “Nuclear Magnetic Resonance” in *Experimental Techniques in Condensed Matter Physics at Low Temperatures*, edited by R. C. Richardson and E. N. Smith (Addison-Wesley, Reading, 1998).
- [16] J. D. Jackson, *Classical Electrodynamics* (Second Edition, John Wiley & Sons, New York, 1975).
- [17] J. T. Markert, Ph. D. Thesis, Cornell University (1987).
- [18] R. L. Liboff, *Transmission Lines, Waveguides, and Smith Charts* (Macmillan Publishing Company, New York, 1985).
- [19] R. A. Chipman, *Shaum’s Outline Series. Theory and Problems of Transmission Lines* (McGraw-Hill, Inc., New York, 1968).
- [20] R. Tian, Masters Thesis, University of Texas at Austin (1997).
- [21] J. L. Cobb, Ph. D. Thesis, University of Texas at Austin (1995).

- [22] J. L. Conway and R. M. Cotts, *Rev. Sci. Instrum.* **48**, 656 (1977).
- [23] D. Lancaster, *TTL Cookbook* (Howard W. Sams & Co., Inc., Indianapolis, 1974).
- [24] M. K. Wu, J. R. Ashburn, C. J. Torng, P. H. Hor, R. L. Meng, L. Gao, Z. J. Huang, Y. Q. Wang, and C. W. Chu, *Phys. Rev. Lett.* **58**, 908 (1987).
- [25] P. Marsh, R. M. Fleming, M. L. Mandich, A. M. DeSantolo, J. Kwo, M. Hong, and L. J. Martinez-Miranda, *Nature* **334**, 141 (1988).
- [26] R. M. Hazen, “Crystal Structures of High-Temperature Superconductors” in *Physical Properties of High Temperature Superconductors*, Vol. II, edited by D. M. Ginsberg (World Scientific Publishing, New Jersey, 1990).
- [27] C. H. Chen, “The Microstructure of High-Temperature Oxide Superconductors” in *Physical Properties of High Temperature Superconductors*, Vol. II, edited by D. M. Ginsberg (World Scientific Publishing, New Jersey, 1990).
- [28] A. Rigamonti, F. Borsa, and P. Carretta, *Rep. Prog. Phys.* **61**, 1367 (1998).
- [29] C. H. Pennington, and C. P. Slichter, “Nuclear Resonance Studies of $\text{YBa}_2\text{Cu}_3\text{O}_{7-\delta}$ ” in *Physical Properties of High Temperature Superconductors*, Vol. II, edited by D. M. Ginsberg (World Scientific Publishing, New Jersey, 1990).

- [30] J. T. Markert, T. W. Noh, S. E. Russek, and R. M. Cotts, *Solid State Comm.* **63**, 847 (1987).
- [31] W. W. Warren, Jr., R. E. Walstedt, G. F. Brennert, G. P. Espinosa, and J. P. Remeika, *Phys. Rev. Lett.* **59**, 1860 (1987).
- [32] L. C. Hebel, C. P. Slichter, *Phys. Rev.* **113**, 1504 (1959).
- [33] T. Imai, T. Shimizu, T. Tsuda, H. Yasuoka, T. Takabatake, Y. Nakazawa, and M. Ishikawa, *J. Phys. Soc. Japan* **57**, 1771 (1988).
- [34] T. Imai, T. Shimizu, H. Yasuoka, Y. Ueda, and K. Kosuge, *J. Phys. Soc. Japan* **57**, 2280 (1988).
- [35] T. Imai, T. Shimizu, H. Yasuoka, Y. Ueda, and K. Kosuge, *Int. J. Mod. Phys. B* **3**, 93 (1989).
- [36] P. Carretta and M. Corti, *Phys. Rev. Lett.* **68**, 1236 (1992).
- [37] P. Carretta, *Phys. Rev. B* **45**, 5760 (1992).
- [38] B. J. Suh, D. R. Torgeson, and F. Borsa, *Phys. Rev. Lett.* **71**, 3001 (1993).
- [39] Y.-Q. Song, *Phys. Rev. Lett.* **75**, 2008 (1995).
- [40] M. Corti, B. J. Suh, F. Tabak, A. Rigamonti, F. Borsa, M. Xu, and B. Dabrowsky, *Phys. Rev. B* **54**, 9469 (1996).
- [41] R. J. Cava, B. Batlogg, C. H. Chen, E. A. Rietman, S. M. Zahurak, and D. J. Werder, *Phys. Rev. B* **36**, 7118 (1987).

- [42] D. E. Farrell, J. R. Clem, and D. K. Finnemore, *Phys. Rev. B* **36**, 4025 (1987).
- [43] J. T. Markert, Y. Dalichaouch, and M. B. Maple, “Rare Earth and Other Substitutions in High Temperature Oxide Superconductors” in *Physical Properties of High Temperature Superconductors*, Vol. I, edited by D. M. Ginsberg (World Scientific Publishing, New Jersey, 1989).
- [44] C. H. Pennington, D. J. Durand, D. B. Zax, C. P. Slichter, J. P. Rice, and D. M. Ginsberg, *Phys. Rev. B* **37**, 7944 (1988).
- [45] R. E. Walstedt, W. W. Warren, Jr., R. F. Bell, and G. P. Espinosa, *Phys. Rev. B* **40**, 2572 (1989).
- [46] S. E. Barrett, D. J. Durand, C. H. Pennington, C. P. Slichter, T. A. Friedmann, J. P. Rice, and D. M. Ginsberg, *Phys. Rev. B* **41**, 6283 (1990).
- [47] E. M. McCarron III, M. A. Subramanian, J. C. Calabrese, and R. L. Harlow, *Mater. Res. Bull.* **23**, 1355 (1988).
- [48] T. Siegrist, L. F. Schneeneyer, S. A. Sunshine, J. V. Waszczak, and R. S. Roth, *Mater. Res. Bull.* **23**, 1429 (1988).
- [49] A. Hayashi, B. Batlogg, and R. J. Cava, *Phys. Rev. B* **58**, 2678 (1998).
- [50] P. K. Davies, *J. Solid State Chem.* **95**, 365 (1991).
- [51] H. F. Fong, B. Keimer, J. W. Lynn, A. Hayashi, and R. J. Cava, *Phys. Rev. B* **59**, 6873 (1999).
- [52] F. C. Zhang and T. M. Rice, *Phys. Rev. B* **37**, 3759 (1988).

- [53] M. D. Chabot and J. T. Markert, *Phys. Rev. Lett.* **86**, 163 (2001).

Vita

Gergana Drandova was born in Sofia, Bulgaria, on January 31, 1972, the daughter of Ivanka and Ilia Drandovi. From a young age she liked solving problems and learning how things functioned. She especially enjoyed the math, geography, and biology classes in her school “Assen Zlatarov”, Sofia, but she also liked drawing, wanted to learn to play different instruments, and was participating in the children’s basketball school of professional sports club “Locomotive”, Sofia. She found physics interesting from the beginning of her physics classes at school, so she decided not to join the athletics high school of “Locomotive”, but instead, in 1986 she applied and was accepted to the physics class of the National Nature and Mathematics High School “Lubomir Chakalov”, Sofia. There she studied extra hours of physics and participated in the student physics olympiads on a national level. In high school she also met some of her best friends in life.

The author considered studying Russian literature for a while, but instead, upon her graduation from high school in 1990 she entered the physics program at Sofia University “St. Kliment Ohridski”. After her second year at the university, she chose the specialization “Elementary Particles and Nuclear Physics” in which she fulfilled the required course work. She also worked under the supervision of Dr. Dimitar Marvakov and wrote her Diploma thesis on

“Irreducible Green Functions in the Theory of Anisotropic Ferromagnets with Biquadratic Exchange Interaction”.

In her first year at Sofia University, while playing bridge in the cafeteria of the physics department, she met Sergey Cheshkov who turned out to have graduated from the same high school as the author and was also just starting his undergraduate studies after completing a two-year mandatory military service. She married Sergey Cheshkov in June, 1998.

After graduating from Sofia University in 1996, the author entered the Graduate School of the University of Texas at Austin. She really enjoyed condensed matter physics, but instead of continuing the theoretical work she did in Bulgaria, she decided to explore the experimental physics world and joined the superconductivity and magnetism lab of Prof. John Markert. There she learned a great deal of physics and actually got to see what’s inside things and how people build them in the first place.

Permanent address: 926E, Dean Keeton St., # 204,
Austin, TX 78705

This dissertation was typeset with \LaTeX^\ddagger by the author.

[‡] \LaTeX is a document preparation system developed by Leslie Lamport as a special version of Donald Knuth’s \TeX Program.